

MICROMACHINED OPTICAL AND ACOUSTIC WAVEGUIDE SYSTEMS FOR
ADVANCE SENSING AND IMAGING APPLICATIONS

A Dissertation

by

CHENG-CHUNG CHANG

Submitted to the Office of Graduate and Professional Studies of
Texas A&M University
in partial fulfillment of the requirements for the degree of

DOCTOR OF PHILOSOPHY

Chair of Committee,	Jun Zou
Committee Members,	Arum Han
	Jun Kameoka
	Kristine Maitland
Head of Department,	Chanan Singh

August 2014

Major Subject: Electrical Engineering

Copyright 2014 Cheng-Chung Chang

ABSTRACT

Evolving from the IC fabrication processes, micromachining technologies allow mass production of 2D or 3D microstructures, which are otherwise difficult to achieve with traditional machining techniques. In this research, novel micromachining processes have been developed to enable new micro optical and acoustic waveguide systems for advanced optical sensing and acoustic imaging applications. The investigated applications include non-invasive cancer detection inside human body, in-field soil characterization, and time-delayed and multiplexed ultrasound and photoacoustic tomography.

Micromachining technology enables miniaturized optical waveguide system for efficient light transmission. The small size and light-guiding capabilities are particularly useful for optical sensing at places deep inside the human body or underground. Two micromachined optical waveguide systems were fabricated and tested. The first one was used to conduct oblique incidence diffuse reflectance spectroscopy (OIDRS) for the determination of tumor margins on human pancreas specimens. The second one was used to conduct visible-near-infrared diffuse reflectance spectroscopy (VNIR-DRS) for extracting the compositional information of soil samples.

Micromachining technology also makes it possible to utilize single-crystalline silicon as a structural material for acoustic wave propagation. It enables the development of high-performance integrated acoustic circuits and allows direct acoustic signal processing and control. The acoustic properties and propagation inside silicon

waveguides were characterized, and the acoustic signal processing using micromachined acoustic waveguide system was investigated. Based on the results, two acoustic waveguide systems were designed and constructed. The first system utilized micromachined acoustic delay lines to passively delay acoustic signal thereby reducing the required transceivers and processing electronics; while the second system employed micromachined acoustic multiplexer to actively control the transmission of acoustic signals. Both techniques are expected to provide new solutions to reduce the complexity and cost of the acoustic receiver systems in ultrasound and photoacoustic imaging.

for my parents

Shih-Lin and Ling-Mei

and in hearty memory of my family friend Mr. Meng

ACKNOWLEDGEMENTS

Foremost, I would like to express my profound gratitude to my committee chair, Dr. Jun Zou, who provides scientific guidance in my research and exchanges valuable life experience.

I am also thankful to my committee members, Dr. Arum Han, Dr. Jun Kameoka, Dr. Kristen Maitland for their constructive comments and supports throughout the course of this research.

My appreciation also goes to my friend and colleague, Dr. Alejandro Garcia-Uribe, for sharing research experiences and his broad knowledge in optics and imaging. His expertise helps me to create useful designs and to conduct meaningful experiments in this work.

I also want to extend my gratitude to the technical staff of Aggie Fab. I would like to thank Mr. Robert Atkins, Mr. Jim Gardner, Mr. Dennie Spears, and Mr. Larry Rehn for maintaining a good working environment and functional equipments.

Thanks also go to my friends and colleagues in solid state group. Dr. Murat Yapici, Dr. Jung Moo Hung, and Dr. Karthik Balareddy shared their invaluable experience in device fabrication. Mr. Yi-Chen Lo and Mr. Yifeng Zhou provide supports and training for the clean room equipments.

Last but most importantly, I would like to thank my parents for their continuously support and encouragement. Without their support, this work would not be possible.

NOMENCLATURE

MEMS	Microelectromechanical systems
DRS	Diffuse reflectance spectroscopy
OIDRS	Oblique incidence diffuse reflectance
VNIR	Visible-near-infrared
MIR	Mid-infrared
PA	Photoacoustic
PAT	Photoacoustic tomography
PAM	Photoacoustic microscopy
PDMS	Polydimethylsiloxane
SNR	Signal to noise ratio

TABLE OF CONTENTS

	Page
ABSTRACT	ii
DEDICATION	iv
ACKNOWLEDGEMENTS	v
NOMENCLATURE	vi
TABLE OF CONTENTS	vii
LIST OF FIGURES	x
LIST OF TABLES	xv
1. INTRODUCTION.....	1
1.1 Motivation.....	1
1.2 Summary of work	2
2. MICROMACHINED OPTICAL WAVEGUIDE SYSTEM FOR OBLIQUE INCIDENCE DIFFUSE REFLECTANCE SPECTROSCOPY (OIDRS).....	6
2.1 Theory of oblique incidence diffuse reflectance spectroscopy	6
2.2 Design of the micromachined optical probe	9
2.3 Fabrication of the micromachined optical probe	12
2.4 Application: Pancreatic tumor margin detection	16
2.4.1 Introduction to pancreatic cancer	16
2.4.2 Current clinical diagnosis.....	18
2.4.3 Non-invasive optical diagnosis	19
2.4.4 Testing setup and cancer detection results	20
2.5 Conclusion	23
3. MICROMACHINED OPTICAL WAVEGUIDE SYSTEM FOR VISIBLE-NEAR- INFRARED DIFFUSE REFLECTANCE SPECTROSCOPY (VNIR-DRS)	25
3.1 Theory of visible-near-infrared diffuse reflectance spectroscopy	25
3.2 Design of the micromachined optical soil probe	28
3.3 Fabrication of the micromachined optical soil probe	33
3.4 Application: Soil characterization	35
3.4.1 Introduction to soil analysis	35
3.4.2 Testing setup for soil characterization	37

	Page
3.4.3 Experimental results and discussion	39
3.5 Conclusions.....	42
4. MICROMACHINED SILICON ACOUSTIC DELAY LINES FOR ULTRASONIC AND PHOTOACOUSTIC IMAGING APPLICATIONS	44
4.1 Introduction.....	44
4.1.1 Ultrasound transducer array receiving system	44
4.1.2 Ultrasound delay line receiving system	45
4.2 Optical fiber delay line system and its limitations.....	46
4.3 Design of silicon acoustic delay line	52
4.4 Materials and methods.....	54
4.4.1 Delay line structure fabrication	54
4.4.2 Characterization setup	55
4.5 Experiment and results.....	57
4.5.1 Acoustic properties: Attenuation and velocity	57
4.5.2 Propagation in U –turn structures with different curvature.....	60
4.5.3 Propagation in Y –junction structures with different angles	62
4.5.4 Comparison of signal shape from different structures	65
4.6 Multi-channel serial and parallel delay lines	66
4.7 Silicon parallel acoustic delay line probe	69
4.8 Conclusion	72
5. MICROMACHINED ACOUSTIC MULTIPLEXER FOR ULTRASONIC AND PHOTOACOUSTIC IMAGING APPLICATIONS	73
5.1 Introduction.....	73
5.1.1 Electronics multiplexing in ultrasound receiving system	73
5.1.2 Acoustic multiplexing in ultrasound receiving system	74
5.2 Design of the acoustic multiplexer	77
5.3 Fabrication of the micromachined acoustic multiplexer.....	80
5.4 Characterization of the micromachined acoustic multiplexer	83
5.5 Application: Photoacoustic imaging with acoustic multiplexer	85
5.5.1 Photoacoustic effect	85
5.5.2 Photoacoustic imaging techniques	87
5.5.3 Experiment setup.....	88
5.5.4 Imaging result.....	90
5.6 Conclusions.....	91
6. CONCLUSIONS	93
REFERENCES	95

	Page
APPENDIX CRYOGENIC REACTIVE ION ETCHING	103

LIST OF FIGURES

	Page
Figure 2.1 Illustration of light absorption and scattering in an inhomogeneous medium. The light scattered out from the tissue surface becomes diffuse reflectance.	6
Figure 2.2 Schematic of the diffusion theory model for oblique incidence.	8
Figure 2.3 Schematic of micro OIDRS probes for in-vivo optical characterization of human tissues: (a) front-viewing configuration and (b) side-viewing configuration. The incidence fiber has a oblique angel in both cases, while the collection fiber/waveguides are perpendicular to the tissue surface.	10
Figure 2.4 Schematic design of the new “side-viewing” OIDRS probe: (a) Collection device and (b) Source device.	11
Figure 2.5 Optical transmission of the Epotec 301 epoxy.	12
Figure 2.6 Schematic of the sample fabrication process.	13
Figure 2.7 Fabricated SU-8 structures. 1 st and 2 nd substrates were used for collection channels, while 3 rd and 4 th substrate were used to accommodate source fiber.	14
Figure 2.8 Schematics of the sample assembly process.	15
Figure 2.9 Complete OIDRS probe. (a) Optical probe with fiber connections. (b) Close-up of probe tip.	16
Figure 2.10 Experimental setup for OIDRS measurement.	21
Figure 2.11 A human pancreas specimen with malignant tumors. The measurements are along the pancreatic duct.	21
Figure 2.12 Diffuse reflectance spectra of human pancreas tissue from ex-vivo OIDRS measurement: (a) Normal tissue; and (b) Cancer tissue. Each color line represents spectrum from one of the five collection channels.	22
Figure 2.13 Average scattering coefficient along the pancreatic duct.	23
Figure 3.1 Spectral absorption signatures from various materials.	26

Figure 3.2	Illustration of the light interaction with soil.	26
Figure 3.3	Different configurations of VNIR-DRS probe for soil characterization: (a) Front viewing; (b) Side viewing.	29
Figure 3.4	Schematic design of the side-viewing VNIR-DRS probe for soil measurement: (a) Source chip; (b) Collector chip; and (c) Front-view of probe assembly with source structures sandwiched between collection structures.	32
Figure 3.5	Microfabricated aluminum-coated SU-8 structures for making the side-viewing VNIR-DRS probe: (a) Source guiding structure; and (b) Collection waveguide structures.	33
Figure 3.6	Assembly of the side-viewing VNIR-DRS probe: (a) Source chip; (b) Collection chip; and (c) Assembled probe.	35
Figure 3.7	Schematic of the VNIR-DRS measurement setup.	38
Figure 3.8	(a) A representative soil sample for VNIR-DRS measurements; (b) Measured diffuse reflectance spectra; and (c) Calculated absorption spectra of the soil sample shown in figure 3.8(a).	39
Figure 4.1	Ultrasound transducer array system: (a) Transducer array setup; (b) Signals received by each transducer. The arrival time is determined by the travel distance and acoustic velocity in the medium.	44
Figure 4.2	Delay line receiving system: (a) Delay lines with single receiving transducer; (b) Ultrasound signals before entering the delay lines; (c) Ultrasound signals with proper delay time; and (d) Ultrasound signals received by the single transducer.	45
Figure 4.3	Ultrasound through-transmission setup.	47
Figure 4.4	Acoustic velocity in optical fiber. (a) Ultrasound signals arrive at different time with respect to the fiber length. (b) The acoustic velocity is determined by the length/time ratio and is about 5108 m/s.	48
Figure 4.5	Optical fiber delay lines system with 16-channel common input and two 8-channel outputs. Inset: Close up look of the 16-channel input terminal with acrylic holder.	50

Figure 4.6	Ultrasound signals received by the 16-channel optical fiber delay line system. (a) Signals received by the 8-channel output terminal 1. (b) Signals received by the 8-channel output terminal 2.	50
Figure 4.7	Schematic of parallel delay lines.	53
Figure 4.8	Schematic of serial delay lines.....	53
Figure 4.9	Schematic of the photoacoustic excitation setup.	56
Figure 4.10	Straight silicon delay line. (a) Sample; (b) Measurement setup: Receive signal from focus points along the straight delay line. L: Traveling length (distance from the focal point to the transducer). R: Receiving transducer.	58
Figure 4.11	Straight silicon delay line measurement. (a) Plot of the arrival time versus traveling length. The average velocity in straight silicon delay line is ~8454 m/s. Inset: Representative signal shape from L: 28.2 mm; (b) Simulation results of signal peak–peak amplitude versus traveling length. Inset: Representative signal shape from L: 30 mm; and (c) Experimental results of signal peak–peak amplitude versus traveling length. Inset: Representative signal shape from L: 28.2 mm.....	58
Figure 4.12	U-turn structure measurement. (a) Sample; (b) Measurement setup: Receive signals from different focus points, A: without bending, B: with bending.....	61
Figure 4.13	U-turn structure measurement. (a) Simulation results of radius versus amplitude ratio. Inset: Representative signal shape from turning with 6 mm radius; and (b) Experimental result of radius versus amplitude ratio. Inset: Representative signal shape from turning with 6 mm radius.....	61
Figure 4.14	Y-junction structure measurement. (a) Samples; (b) Measurement setup: Receive signals from different focal points, A: without passing junction, B: passing junction through branch with an angle, C: passing junction through straight line.	63
Figure 4.15	Y-junction structure measurement. (a) Simulation results of angle versus amplitude ratio. Inset: Representative signal shapes from junction with 15 degrees; and (b) Experimental results of angle versus amplitude ratio. Inset: Representative signal shapes from junction with 15 degrees.	64
Figure 4.16	Pulse shape and spectrum of different structures.....	65

Figure 4.17 4-channel serial delay lines assembled on an acrylic holder.	67
Figure 4.18 4-channel parallel delay lines. (a) Fabricated; and (b) Assembled on an acrylic holder.	67
Figure 4.19 Two-port through-transmission setup.	67
Figure 4.20 Time-delayed signals from. (a) 4-channel serial delay lines; and (b) 4-channel parallel delay lines.	68
Figure 4.21 Etched silicon acoustic delay lines.	70
Figure 4.22 Assembled 16-channel silicon acoustic delay lines probe.	71
Figure 4.23 Ultrasound signals propagating in the 16-channel silicon acoustic delay line probe received by a single transducer.	71
Figure 5.1 Ultrasound transducer array receiving system. (a) Transducer array and electronics setup; (b) Ultrasound signals received by the transducer array. T_1, T_2, T_3, T_4 are the acoustic signal traveling time inside the phantom.	74
Figure 5.2 Acoustic multiplexer receiving system. (a) System setup; (b) Acoustic signals received by the multiplexer input; (c) Acoustic signals after multiplexing; (d) Ultrasound signals received by the single transducer. T_M is the acoustic signal traveling time inside the multiplexer.	75
Figure 5.3 Schematic design of the acoustic multiplexer. Acoustic signal can be coupled to the output end through mercury droplet. The location of the mercury droplet is controlled by external air pressure.	77
Figure 5.4 Simulation results of the "ON" state and "OFF" state acoustic channels. (a) Air-coupling "OFF" state; (b) Mercury-coupling "ON" state. Inset: Simulation setup. The air and mercury gaps are 500 μm in width.	80
Figure 5.5 Fabricated silicon acoustic multiplexer structure (one side).	81
Figure 5.6 Acoustic multiplexer assembly process.	82
Figure 5.7 Assembled acoustic multiplexer. (a) Side view; (b) Top view.	82
Figure 5.8 Ultrasound transmission experiment setup.	84
Figure 5.9 Acoustic ON/OFF characterization. (a) Reference signal from silicon delay line; (b) "ON" setup and the transmitted signal; (c) "OFF" setup and the transmitted signal.	84

Figure 5.10 Ultrasound signals from each channel received by the transducer.	85
Figure 5.11 Physical process of photoacoustic effect.	86
Figure 5.12 Photoacoustic imaging setup.	89
Figure 5.13 Zoom in view of the imaging target inside the optical phantom.	90
Figure 5.14 Photoacoustic imaging results. (a) Photoacoustic signals received from each channel; (b) Reconstructed photoacoustic image.	91
Figure A.1 Etching for 40 minutes with different line width (unit: μm).	104
Figure A.2 Etching for 40 minutes with different trench width (unit: μm).	104

LIST OF TABLES

	Page
Table 1 Fiber length and signal/echo arrival time for each channel.	49
Table 2 Delay line design parameters.	70
Table 3 On-chip driving mechanism.	92
Table 4 Process recipe for through-wafer etching.	104
Table 5 Etching profile with different O ₂ flow rate for 10 minutes.	105
Table 6 Etching profile with different etch time.	106

1. INTRODUCTION

1.1 Motivation

Optical waves can be used for in-vivo and non-invasive sensing and imaging, such as material science, biomedical science, and chemistry. To efficiently collect signals for the sensing or imaging targets, optical waveguide systems such as fiber-optic sensor probes can be used. However, the large dimension of the probe and low penetration depth of the optical waves have limited the possibility of using the probe for samples deep inside a medium or located in a tight space. To address these issues, miniaturized optical waveguide systems are needed.

Micromachining technologies provide ways to create optical waveguide systems with controllable collection angles. The micromachined optical waveguide devices are easy to construct and have small dimensions and high optical transmission efficiency. In this research, two kind of optical waveguide systems capitalizing micromachining technologies were developed. A micro “side-viewing” probe has been built to enable in-vivo oblique incidence diffuse reflectance spectroscopy (OIDRS) measurement for pancreatic cancer detection and another micro “side-viewing” probe has been built to enable in-field visible-near-infrared diffuse reflectance spectroscopy (VNIR-DRS) measurement on soils.

In addition to optics, ultrasound waves are also be used for non-destructive sensing and imaging applications. To receive and process the acoustic signals, multiple electrical components that involve transducers and data acquisition are necessary. Furthermore, to achieve fast and real-time imaging, array of ultrasound transducers are

needed. Ultrasound signals from the sample are detected by transducer array at the same time, which requires multiple-channel receiving electronics for data acquisition. This massive transducer array, together with their interfacial electronics, made the ultrasound system complex and costly. This situation has turned out to be a bottleneck for array-base ultrasound systems.

The above issue can be solved by using micromachining technology to create structural acoustic waveguide devices to replace the expensive electronic components. Micromachining technology enables multiple designs to be made simultaneously and directly from silicon, which is a good acoustic material with low transmission loss. Instead of controlling and processing electrical signals, the micromachined acoustic waveguide devices can function similarly to the electrical counterparts by directly handling the acoustic signals. In this research, two silicon-based acoustic waveguide devices, delay lines and multiplexer, were fabricated with micromachining technologies to replace the complex receiving configuration in ultrasound system. Silicon delay lines can introduce true time delays into the acoustic signals and silicon multiplexer can select signals out from multiple channels. The functionalities of both devices were demonstrated in ultrasound and photoacoustic imaging systems. These methods could potentially reduce the cost and complexity of the ultrasonic receiving system.

1.2 Summary of work

In section 2, the design, fabrication and testing of a novel miniaturized optical sensor probe with “side-viewing” capability is presented. Its small size, unique “side-viewing” capability and high optical transmission efficiency enable the agile

maneuvering and efficient data collection even in the narrow cavities inside the human body. The sensor probe consists of four micromachined substrates with optical fibers for oblique light incidence and collection of spatially resolved diffuse reflectance from the contacted tissues. The optical sensor probe has been used to conduct the oblique incidence diffuse reflectance spectroscopy (OIDRS) on a human pancreatic specimen. Based on the measurement results, the margin of the malignant tumor has been successfully determined optically, which matches well with the histological results.

In section 3, the design, fabrication and testing of a new micro optical sensor probe with side-viewing function to enable in-field visible-near infrared diffuse reflectance spectroscopy (VNIR-DRS) for soil is discussed. The optical probe consists of two microfabricated source chips and two collection chips. The source chips are used to deliver oblique light incidence onto the soil surface, while the diffuse reflectance is received from the normal direction through the collector chips. Several design and fabrication considerations have been made to optimize the optical transmission efficiency of the probe and the signal-to-noise ratio (SNR) of the collected diffuse reflectance signal. The probe has a small outer dimension and thus can be easily fit into a typical soil penetrometer for in-field VNIR-DRS measurements. Using the new optical probe, VNIR-DRS measurements have been successfully conducted on a number of soil samples, which shows the new optical probe offers better performance than the existing commercial reflectance soil probe.

In section 4, the concept of ultrasound delay line receiving system is first demonstrated with an optical fiber-based delay line system. Following that, the design,

fabrication, and testing of novel micromachined silicon-based acoustic delay line system are presented. The acoustic properties of different silicon delay line structures have been characterized. Based on the experiment results, two different acoustic delay line systems (parallel and serial) have been successfully demonstrated to create controlled time delays in multiple channels of ultrasound signals. A silicon parallel delay line probe is also developed. Upon single acoustic excitation cycle, the time-delayed ultrasound signals from multiple channels are received with a single-element ultrasound transducer in a time-serial manner. This unique capability could be used to merge signals from multiple channels, thereby enabling new real-time ultrasound receiver designs with potentially less complexity and lower cost.

In section 5, a novel micromachined silicon-based microfluidic acoustic multiplexer was presented. The acoustic multiplexer is capable of selectively transmitting ultrasound signals travelling in multiple acoustic channels one at a time. By performing selections in multiple acoustic excitation cycle, ultrasound signals from all channels can be selected sequentially and sent and/or received in a serial manner with only one single-element ultrasound transducer, followed by single channel of data acquisition electronics. The switching performance of the acoustic multiplexer is tested with ultrasound transmission experiment. An 8-channel acoustic multiplexer is constructed and its functionality for imaging is demonstrated by conducting photoacoustic (PA) imaging for an optically absorptive object inside a phantom. The use of acoustic multiplexer allows individual PA signals to be received with only one

ultrasound transducer, thus effectively reducing the complexity of the ultrasound receiver system.

2. MICROMACHINED OPTICAL WAVEGUIDE SYSTEM FOR OBLIQUE INCIDENCE DIFFUSE REFLECTANCE SPECTROSCOPY (OIDRS)*

2.1 Theory of oblique incidence diffuse reflectance spectroscopy

As shown in figure 2.1, when light is incident on the surface of an inhomogeneous medium (e.g. biological tissue), some of the incident light will be directly reflected (specular reflectance) and the remaining light will transmit into and interacts with the medium through scattering and absorption.

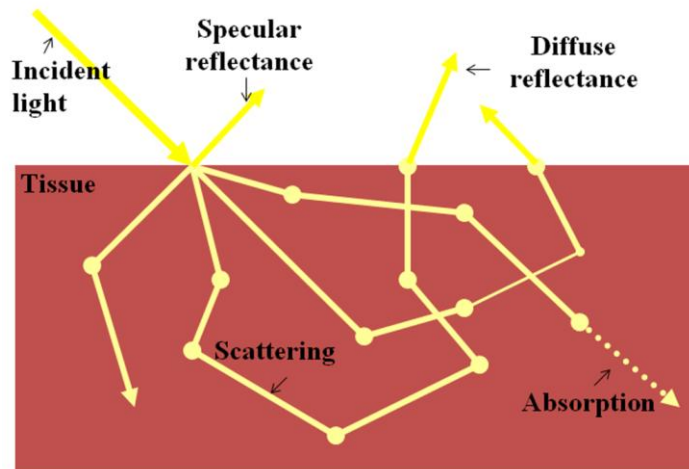


Figure 2.1 Illustration of light absorption and scattering in an inhomogeneous medium. The light scattered out from the tissue surface becomes diffuse reflectance.

*@ 2011 IEEE. Reprinted, with permission, from Alejandro Garcia-Urbe, Cheng-Chung Chang, Murat K. Yapici, Jun Zou, Bhaskar Banerjee, John Kuczynski, Evan Ong, Erin S. Marner, Benjamin H. Levy, and Lihong V. Wang, "High-transmission-efficiency and side-viewing micro OIDRS probe for fast and minimally-invasive tumor margin detection," IEEE Sensor Journal, 11(4), pp. 891-896, 2011.

After undergoing multiples times of interactions, part of the transmitted light will be scattered back to the surface and escape from the medium to form the diffuse reflectance.

The spatially resolved steady-state diffuse reflectance for a particular wavelength can be calculated by diffusion theory [1].

$$R(x) = \frac{1}{4\pi} \left[\frac{\Delta z (1 + \mu_{eff} \rho_1) \exp(-\mu_{eff} \rho_1)}{\rho_1^3} + \frac{(\Delta z + 2z_b) (1 + \mu_{eff} \rho_2) \exp(-\mu_{eff} \rho_2)}{\rho_2^3} \right] \quad (1)$$

where ρ_1 and ρ_2 are the distances between the positive and negative source points and the observation point on the medium surface (figure 2.2). Δz is the distance between the virtual boundary and the tissue depth, and z_b is the distance between the virtual boundary and the surface of the sample . The distance from the point of incidence to the positive point source d_s is equal to $3D$. For oblique incidence, the diffusion coefficient is $D = (3(0.35\mu_a + \mu_s'))^{-1}$, where μ_a is the absorption coefficient and μ_s' is the reduced scattering coefficient. The effective attenuation coefficient $\mu_{eff} = (\mu_a / D)^{1/2}$. The shift of the point sources in the x direction $\Delta x = \sin(\alpha_t) / (3(0.35\mu_a + \mu_s'))$, and α_t is the angle of light transmission into the medium. The absorption and reduced scattering coefficients can be calculated by [2]

$$\mu_a = \frac{\mu_{eff}^2 \Delta x}{3 \sin(\alpha_t)} \quad (2)$$

$$\mu_s' = \frac{\sin(\alpha_t)}{\Delta x} - 0.35\mu_a \quad (3)$$

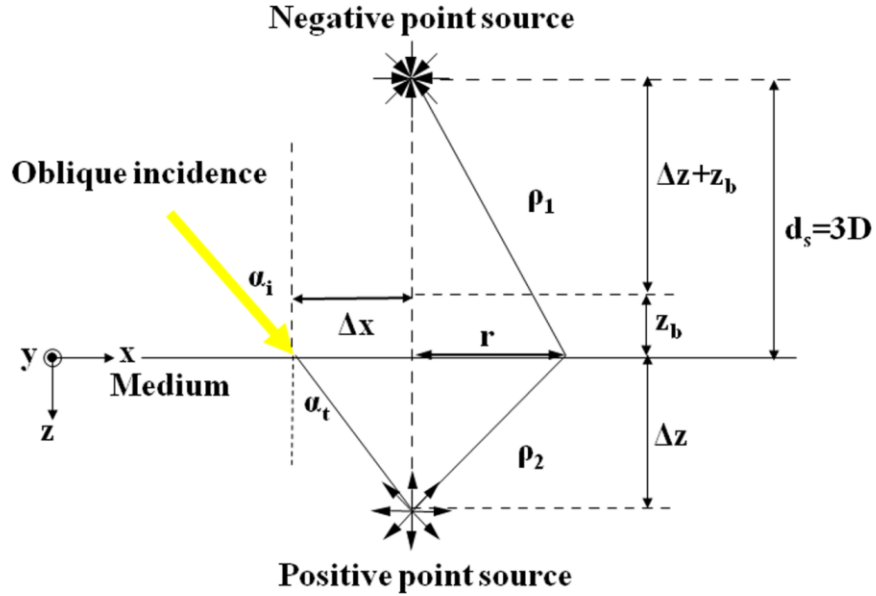


Figure 2.2 Schematic of the diffusion theory model for oblique incidence.

The assumption of the diffusion theory is that the reduced scattering coefficient is much larger than the absorption. The source and detector must also be separated in space so that the light is diffuse reflectance instead of specular reflectance. The diffuse reflectance light travels through the medium, thus optical signatures of the medium are more dominant. When the distance between the source and the detectors is comparable to the transport mean free path (~ 1 mm), diffusion theory does not apply. In this case, Monte Carlo simulation can be applied to extract optical properties from the diffuse

reflectance [3]. Dr. Lihong Wang and S. L. Jacques developed a Monte Carlo modeling software for photon transportation in biological tissue [4]. This software was used to determine the optical properties of pancreatic tissue in this section.

The optical absorption of the human tissue is mostly related to the concentration of hemoglobin and its oxygen saturation. These parameters are believed to have close relationship with the disease state of lesions [5], [6]. On the other hand, the cell nuclei of the tissue can be considered as the major contributor for the scattering properties. Research has shown the diameter of the nuclei would increase with the degree of dysplasia in different lesions [7]. Therefore, the close relationship between the optical absorption and scattering properties can be used to differentiate the state of the malignancy of human tissue, which forms the physiological foundation for applying OIRS for the cancer detection.

2.2 Design of the micromachined optical probe

In the OIRS measurements, light with particular wavelengths is delivered at a desirable oblique incidence angle on the tissue surface and the one-dimensional linear distribution of the diffuse reflectance $R(x)$ is collected. While this can be achieved by using a conventional front-viewing probe that consists of straight optical fiber bundles (figure 2.3(a)), it will not be convenient and feasible to conduct *in-vivo* OIRS measurements inside the human body. This is due to the fact that internal organs mostly consist of long and narrow tubular cavities. To address this issue, the idea of building a miniaturized side-viewing fiber optic probe suitable for measurements inside the human body (figure 2.3(b)) was investigated. However, the side-viewing capability requires all

the collection fibers to undergo a sharp 90° turn within a radius of curvature less than 2.5 mm. This inevitably would cause significant light loss and leakage and also possible mechanical fracture of the collection fibers.

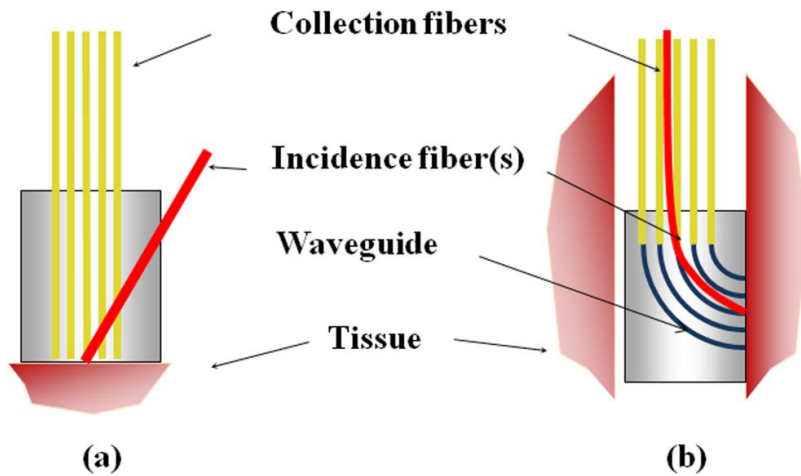


Figure 2.3 Schematic of micro ODIRS probes for in-vivo optical characterization of human tissues: (a) front-viewing configuration and (b) side-viewing configuration. The incidence fiber has an oblique angle in both cases, while the collection fiber/waveguides are perpendicular to the tissue surface.

To solve this problem, we came up with a new probe design using optical-epoxy-filled waveguides. The probe consists of two micromachined devices assembled together. The first device functions as collectors of the diffuse reflection and contains five epoxy-filled waveguides with a 90° turn for side viewing, which are coupled to $100\ \mu\text{m}$ core diameter optical fibers (figure 2.4(a)). The waveguides are filled with optically transparent epoxy (Epotek 301, Epoxy Technology, Inc., Billerica, MA, USA) to increase the coupling efficiency with the fibers and protect them from possible

contamination from the body fluids (e.g. blood). The optical epoxy has a high optical transmission of 98% in the visible wavelength range (figure 2.5), thus can effectively transmit light in the epoxy-filled waveguides. In the second device, two chips are assembled to hold and position one source fiber (200 μm in core diameter) which delivers light precisely at an oblique angle to the tissue of interest (figure 2.4(b)).

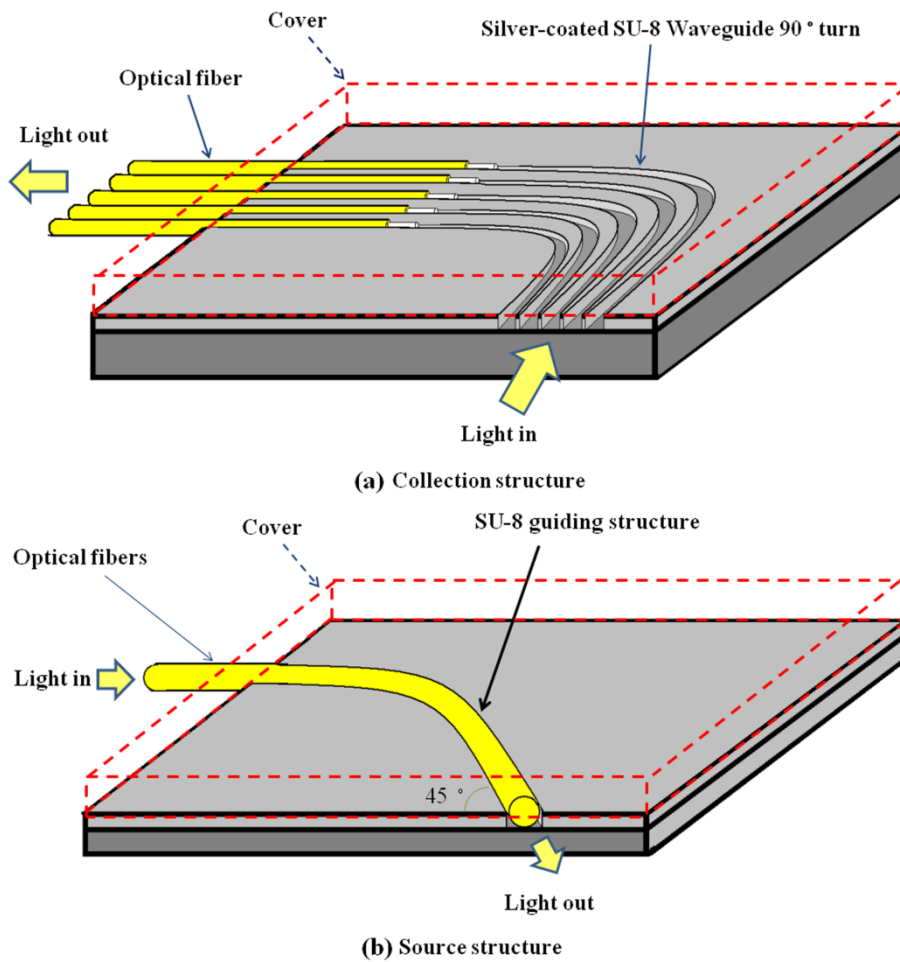


Figure 2.4 Schematic design of the new “side-viewing” OIIRS probe: (a) Collection device and (b) Source device.

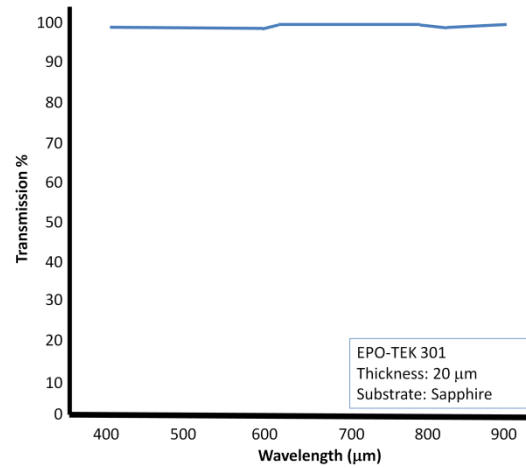


Figure 2.5 Optical transmission of the Epotec 301 epoxy.

2.3 Fabrication of the micromachined optical probe

The detail of the probe fabrication process is described below. Figure 2.6 shows the fabrication process. Four silicon substrates with patterned SU-8 channel are used. SU-8 (MicroChem, Newton, MA, USA) is chosen as the structural material because it can easily form patterned thick layers with high aspect ratio. The fabrication of SU-8 structure fabrication is based on the recipe from the material provider [8]. Silicon wafers were first cleaned and baked at 200 °C for 5 minutes. SU-8 50 and SU-8 100 photoresists were spun on cleaned silicon wafers at a calibrated speed for 30 seconds, resulting approximately 75 μm and 125μm in thickness, respectively. For the first and second substrates with 75μm in thickness, a soft bake of 65 °C for 15 minutes and then at 95 °C for 35 minutes was conducted, followed by a UV exposure of 300 mJ/cm². After the exposure, the wafers were baked at 65 °C for 1 minute and 95 °C for 12 min to allow chemical cross-link at the exposed region. The development of the SU-8 patterns was

conducted for several minutes until unexposed region was completely removed. Similarly, for the third and fourth substrates with 125 μm in thickness, a 65 °C soft bake for 25 minutes and a 95 °C soft bake for 55 minutes was performed. The UV exposure power was 400 mJ/cm^2 and the develop process took about 14 minutes. During the baking process, a slow temperature ramping was used to reduce the internal stress and prevent cracks formation within the SU-8 film.

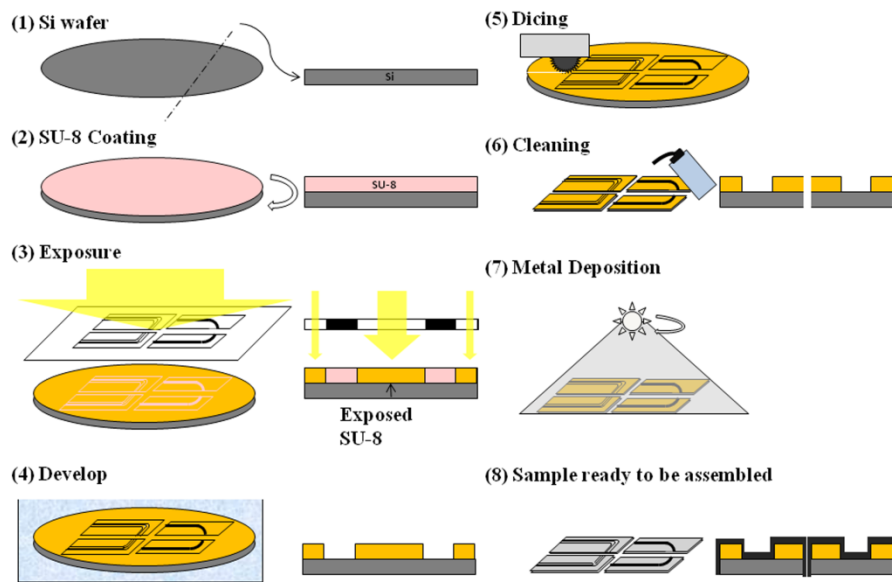


Figure 2.6 Schematic of the sample fabrication process.

The first and second substrates have five curved SU-8 channel ($\sim 75 \mu\text{m}$ deep, $\sim 150 \mu\text{m}$ wide) on each of them and their patterns are mirror-flipped. When the two substrates are stacked together, tightly closed channels with cross section $150 \mu\text{m} \times 150 \mu\text{m}$ can be formed and serve as the waveguide and positioning device for the connection

fibers. Similarly, the third and fourth substrates each have one open channel ($\sim 125 \mu\text{m}$ deep, $250 \mu\text{m}$ wide) and mirror flipped patterns (figure 2.7). When being stacked together, a close channel with $250 \mu\text{m} \times 250 \mu\text{m}$ cross section can be created as a position structure for source fiber.

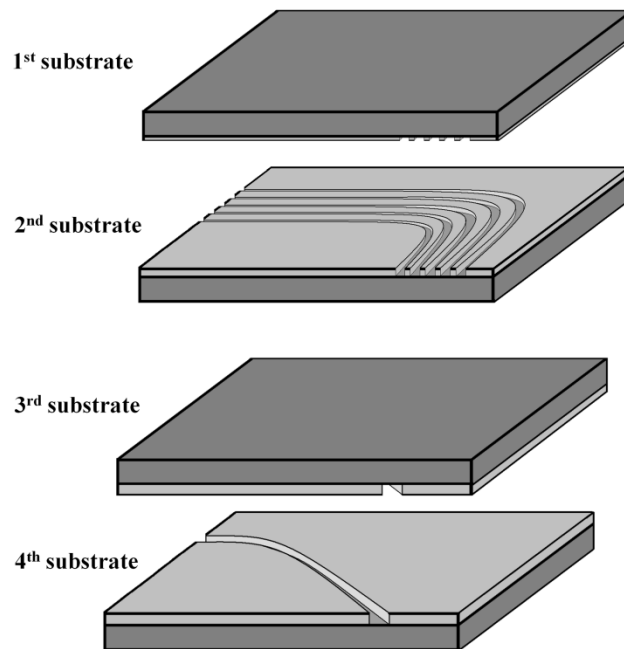


Figure 2.7 Fabricated SU-8 structures. 1st and 2nd substrates were used for collection channels, while 3rd and 4th substrates were used to accommodate source fiber.

To form the optical waveguides, all channels were coated with a thin layer of silver ($\sim 300 \text{ nm}$ thick) uniformly using electron-beam evaporation. Transparent optical epoxy is applied to fill the collection waveguides and the fibers are placed inside all the aligning SU-8 channels. The assembly of the probe was essentially stacking and aligning

the four substrates and glued together (figure 2.8). The proximal ends of the fibers are connected to the OIIRS system and the light source via SMA 905 connectors. The completely assembled probe is shown in figure 2.9. The probe has one 45° oblique incidence channel and five collection channels with an overall dimension of $8 \times 2.5 \times 2 \text{ mm}^3$. This small size provides the possibilities for endoscopic applications inside human body.

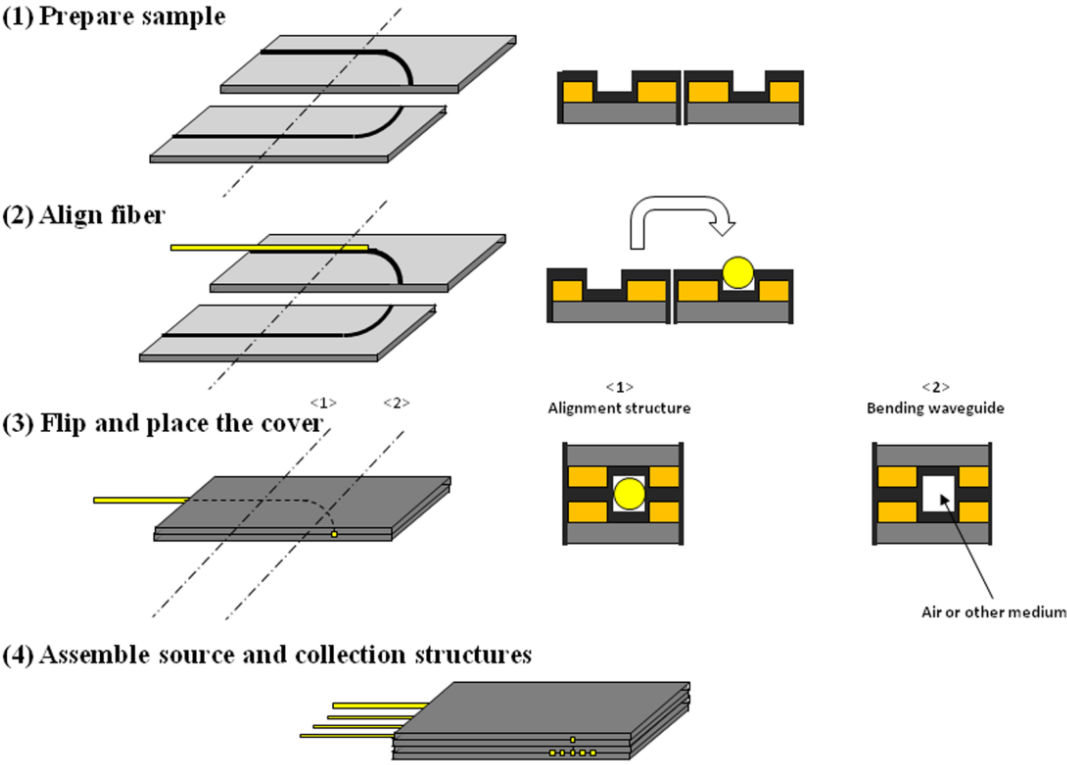


Figure 2.8 Schematics of the sample assembly process.

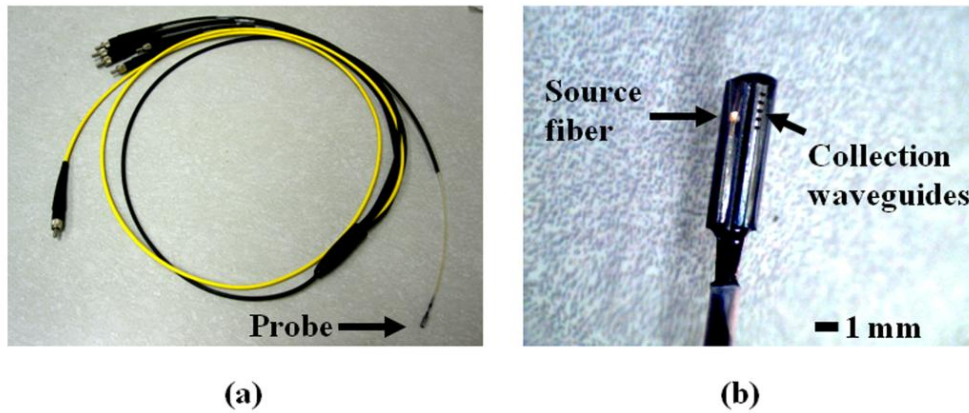


Figure 2.9 Complete OIIRS probe. (a) Optical probe with fiber connections. (b) Close-up of probe tip.

2.4 Application: Pancreatic tumor margin detection

2.4.1 Introduction to pancreatic cancer

Pancreas is an internal organ which is long and narrow. It locates behind the stomach and connects the duodenum and part of the digestive tract. The main function of pancreas is to secret digestive enzyme from exocrine cells to facilitate digestion and to produce insulin from endocrine cells to regulate blood sugar level. Pancreatic cancer is mostly occurred at the exocrine cells. The survival rate of the pancreatic cancer is relatively low compared with many other types of cancers. The American Cancer Society estimated that there were about 46,420 new cases of pancreas cancers with about 39,590 deaths in the U.S. in 2014 [9]. The chance of developing pancreatic cancer in a lifetime is about 1.47%, while this rate is slowly increasing over the past 10 years. The low survival rate is due to the fact that early detection of pancreatic cancer is difficult. Because the pancreas is deep inside the body, behind the stomach and large intestine,

early tumors cannot be seen by routine physical examinations. In addition, the initial symptoms are not obvious, and so far there are no tests or physical exams can effectively detect the pancreatic cancer in its early stage.

Some symptoms can be used as signs of exocrine pancreatic cancer. Jaundice is the yellowing of eyes and skin. The yellowish color is originated from the accumulation of Bilirubin in the body. Bilirubin is made by the liver and excreted into bile. When the pancreatic cancer compresses and blocks the bile duct, Bilirubin starts to build up and jaundice occurs. Also, pain in the abdomen or back may be caused by the enlargement of the pancreas. Unintended weight loss and digestive problems may associate with pancreatic cancer.

The main types of treatment for pancreatic cancer are surgery, ablative techniques, radiation therapy, and chemotherapy. The surgery method requires doctors to remove the pancreatic cancer completely. However, the pancreatic tumor margin is hard to be distinguished from benign tissue; therefore, the surgery becomes one of the most difficult operations. Ablative techniques are invasive methods that directly destroy the pancreatic cancer inside patient's body with the aid of probes. Depending on the destroying methods, there are radiofrequency ablation, microwave thermotherapy, and cryosurgery. Radiation therapy utilizes high-energy x-rays to kill the pancreatic cancer cell. It is non-invasive and suitable for wide-spread pancreatic tumor, but patients may sometimes suffer from the side effects such as skin burn, nausea, diarrhea, and weight loss. Chemotherapy uses anti-cancer drugs to kill the pancreatic cancer cell. This method is suitable for any stages of the pancreatic cancer and lowers the chance of reoccurrence

of the pancreatic cancer. However, the drugs also damage normal cells, resulting side effects such as nausea, diarrhea, hair loss, and loss of appetite. Since all these treatments have their limitations such as the side effects and intensive medical surgery and expenses, the early diagnosis of pancreatic cancer is necessary and economical for potential patients.

2.4.2 *Current clinical diagnosis*

Currently clinical methods for early diagnosing of pancreas cancers start from physical examination and lab tests. During the physical examination, doctors may check any symptoms that are caused by pancreatic cancer or feel a mass in the abdomen. In the lab test, doctors may check if the bile flow is blocked. Following by the tests and examinations, doctors may order patients to go through imaging test, such as computer tomography, magnetic resonance imaging, and ultrasound imaging. If the imaging results indicate high possibility of being pancreatic cancer, surgical processes including laparoscopy and biopsy are required. Tissues from the suspicious regions are removed from the patient and histologically analyzed. Based on the results, another suspicious cite for tissue removal is planned and performed. Multiple rounds of cut-and-analyze procedure are required to complete the tumor removal, which would end up with an extremely time-consuming surgical procedure. Furthermore, for the follow-up treatments, these methods lack the ability to quickly and precisely determine a safe margin for removing the malignant pancreatic tissues. To address this issue, new techniques that can enable simple, fast, accurate and reliable tumor margin detection are necessary. Optical detection becomes a possible solution for its fast detection time, ease of use for

surgeon with minimal invasive procedure, and reliable optical spectrum readout from the suspicious sites.

2.4.3 *Non-invasive optical diagnosis*

Recent studies have shown that the change in the optical absorption and scattering properties of human tissues are closely related to their states of the malignancy [10], [11]. Several different optical methodologies have been investigated for determining the malignancy of tumors [12], [13]. Optical and spectroscopic methods such as near-infrared spectroscopy, Raman spectroscopy, and fluorescent spectroscopy, have been applied in tissue diagnosis for skin, gastrointestinal tract, cervix, and breast. Among them, oblique incidence diffuse reflectance spectroscopy (OIDRS) is a unique approach, which utilizes a special fiber optic sensor probe to measure the diffuse reflectance of the tissue in contact [14]. The diffuse reflectance spectra can be further used to extract optical absorption and scattering properties of the tissue [15]. From previous studies, a remarkably high accuracy of 95% in differentiating (pre)cancerous human skin lesions from benign ones with automated OIDRS data processing and classification [14] is achieved. However, to extend the application of OIDRS from skin to pancreas cancer which is inside the body, miniaturized fiber optic probes suitable for inner-body measurements are needed. For these reasons, the 2-mm micromachined OIDRS probe with side-viewing capability is particularly suitable for this application. This miniaturized, high optical transmission efficiency, and “side-viewing” configuration makes it compatible with medical endoscopes for effective and efficient in-vivo measurements even in the narrow cavities inside human body.

2.4.4 Testing setup and cancer detection results

The OIDRS measurement setup is shown in figure 2.10. It consists of a white light source (halogen lamp), a fiber optic probe, an imaging spectrograph coupled with a CCD camera, and a personal computer. The source fiber of the optical probe is connected to the light source, while the collection fibers are connected to the spectrograph. During the OIDRS measurement, the probe is gently placed on the surface of the tissue. The incident light is delivered at an oblique angle through the source fiber, and the spatial distribution of the diffuse reflectance ($R(x)$) is acquired by the collection waveguides and transmitted through the collection fibers to the spectrograph. The CCD camera captures the diffuse reflectance spectra (from 455 to 765 nm) from all the collection channels within about one second, which are then stored in the personal computer for future analysis. Before the OIDRS measurement, the whole experimental setup was calibrated using a standard liquid phantom with trypan blue dye as the absorbers and polystyrene microspheres as the scattering elements [16]. After calibration, the OIDRS probe was used to conduct *ex-vivo* measurements on a freshly excised human pancreas specimen with malignant tumors (figure 2.11). It should be noted that due to the extensive bleeding caused by the surgical excision, the entire pancreatic specimen appears in the same bloody color, which makes it almost impossible to visually differentiate the normal and malignant regions.

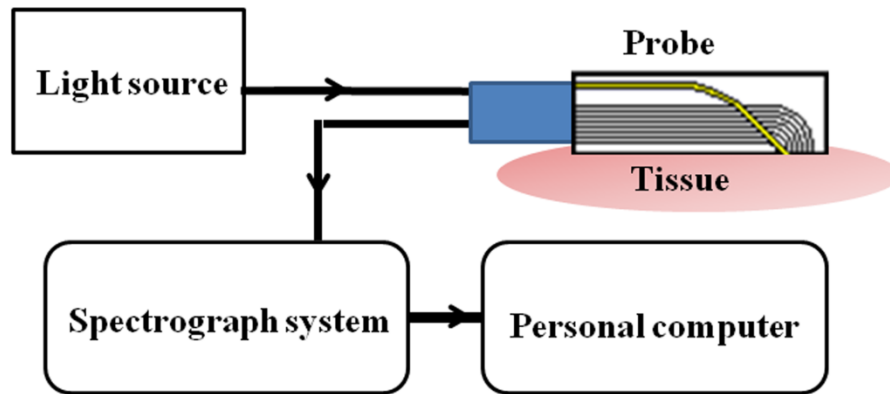


Figure 2.10 Experimental setup for OIDRS measurement.

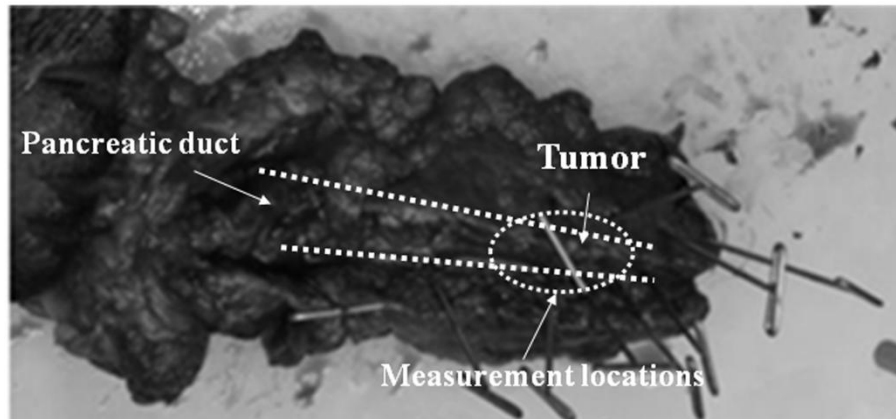


Figure 2.11 A human pancreas specimen with malignant tumors. The measurements are along the pancreatic duct.

Figure 2.12(a) and 2.12(b) show the representative diffuse reflectance spectra (five channels) measured from both the normal and the malignant regions in the pancreas specimen, which clearly show the difference in their optical signatures. To better understand the physiological origin of these differences, the absorption and scattering parameters were extracted from the measured diffuse reflectance spectra.

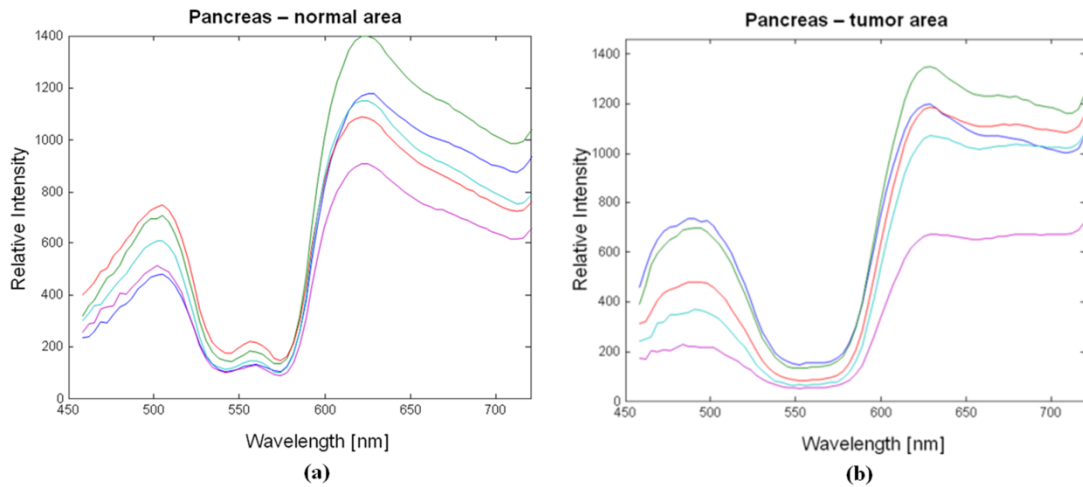


Figure 2.12 Diffuse reflectance spectra of human pancreas tissue from ex-vivo OIDRS measurement: (a) Normal tissue; and (b) Cancer tissue. Each color line represents spectrum from one of the five collection channels.

In human tissues, hemoglobin is the major absorber within the visible spectrum. As shown in figure 2.11, due to the extensive bleeding caused by the surgical excision, the concentration of the hemoglobin and thus the absorption parameters of both the normal and malignant regions in the pancreatic specimen must have changed significantly from their original values. However, the scattering parameter, which is mainly due the cell density and the size of the cell nuclei, will not be affected by the bleeding. Previous studies have shown that malignant tissues usually manifest higher optical scattering due to increased cell density and enlarged cell nuclei. Therefore, the relative value of the scattering parameter could serve as a good indicator to differentiate the malignant tissues from the normal ones. To test the feasibility of using OIDRS for malignant tumor margin detection, we made a series of measurements along the opened pancreatic duct (where the pancreatic cancers usually start to develop). Figure 2.13

shows the extracted scattering parameters for different locations along the pancreatic duct, which clearly indicate the existence and location of the tumor region. This result matches well with the histological reading of the pancreas specimen.

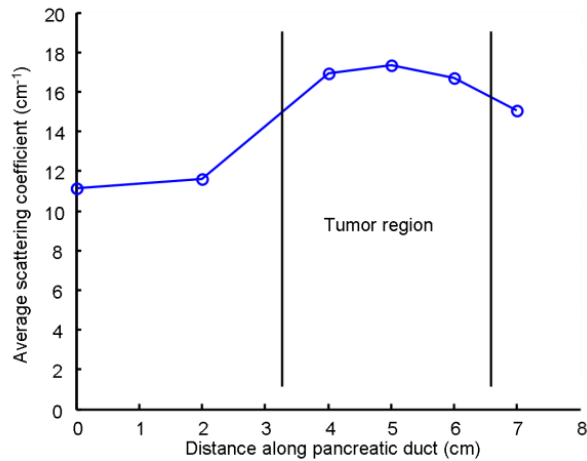


Figure 2.13 Average scattering coefficient along the pancreatic duct.

2.5 Conclusion

A new miniaturized OIDRS optical sensor probe with side-viewing capability has been successfully developed utilizing micromachining technology. Our preliminary results show that the probe, combined with OIDRS can provide both functional and structural information of tissue malignancy and thus can be a useful tool for rapidly determining a safe margin for the surgical treatment of cancers. The new OIDRS probe has been used to conduct diffuse-reflectance measurement on a human pancreas specimen. Based on the measurement and classification, the margin between the malignant tissues and the benign ones has been successfully identified, which matches

well with the histological results. The micromachining technology plays a critical role in enabling probe miniaturization and performance enhancement for the clinical application of OIRS.

3. MICROMACHINED OPTICAL WAVEGUIDE SYSTEM FOR VISIBLE-NEAR- INFRARED DIFFUSE REFLECTANCE SPECTROSCOPY (VNIR-DRS)*

3.1 Theory of visible-near-infrared diffuse reflectance spectroscopy

When light is incident on a medium surface (such as soil), part of the incident light is directly reflected or scattered back, while the remaining part transmits into the medium. After going through a number of absorption and scattering events, some of the transmitted photons could escape from the surface, which form the so-called diffuse reflectance (figure 3.1). Recently, diffuse reflectance spectroscopy (DRS) has attracted much interest from the soil science community. DRS has a number of advantages such as rapid, timely, cheap, non-destructive and hence more efficient in collecting soil information when large number of soil samples require analysis. In addition, a single spectrum allows simultaneously characterize various sample's constitutes and physical, chemical, and biological properties. For example, the diffuse reflectance of soils is largely affected by mineral and clay content. Different minerals and clays have their own characteristic optical absorbance as a function of wavelength, which are due to their specific electron transition and atomic vibration (figure 3.2). Because of the close relationship between the diffuse reflectance spectrum and the optical absorption and scattering of various soil contents, critical information about the soil composition and properties can be obtained with DRS [17]–[19].

*@ 2011 IEEE. Reprinted, with permission, from Cheng-Chung Chang, Alejandro Garcia-Urbe, Jun Zou, and Christine L. S. Morgan, "Micro side-viewing optical probe for VNIR-DRS soil measurement," IEEE Sensor Journal, 11(10), pp. 2527-2532, 2011.

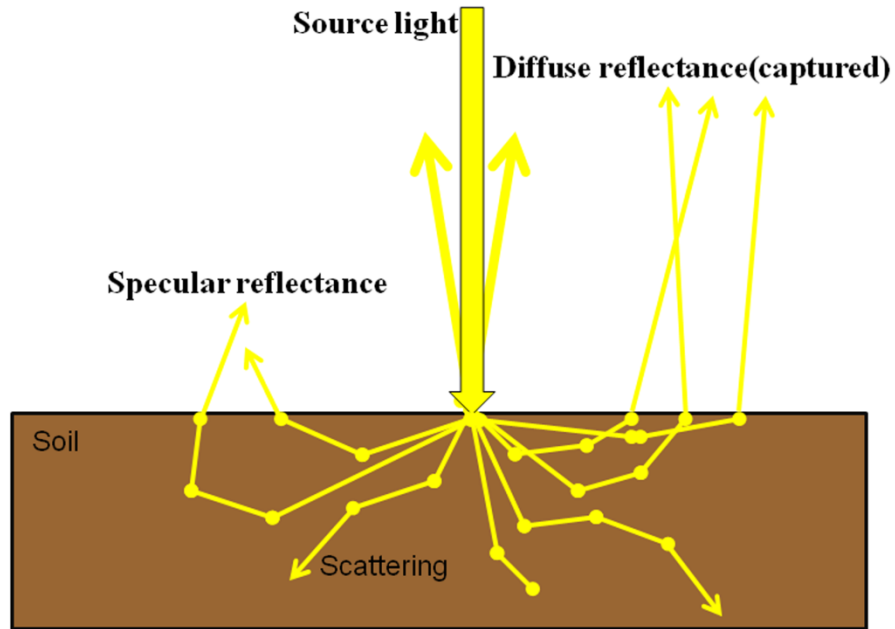


Figure 3.1 Illustration of the light interaction with soil.

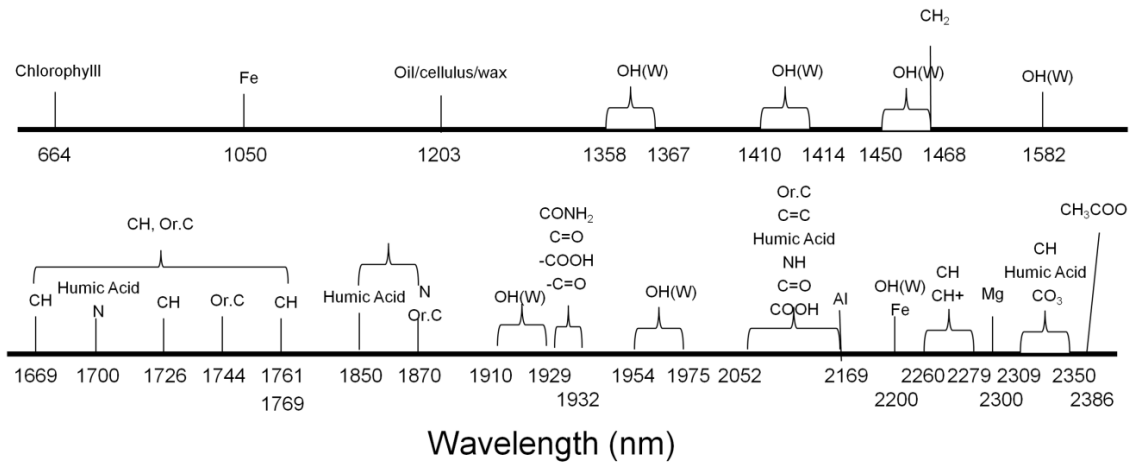


Figure 3.2 Spectral absorption signatures from various materials.

The constitution of medium can be determined by the DRS spectrum. This is based on the assumption that the spectrum is a linear combination of the spectral signature of individual composition weighted by their abundance [20]. Based on that, a multivariate linear model can be used to express the spectrum and quantitatively predict the amount of spectral components. Quantitatively spectral analysis requires sophisticated statistical techniques. Many statistical methods have been applied to determine soil attributes [21]. For example, multiple regression analysis has been used to relate specific band in the NIR spectrum to a number of soil properties [22]. Other statistical methods such as partial least square regression [23], principle component regression [24], and neural-networks [25] have also been used for material analysis.

Based on the spectrum range, DRS can be categorized into visible and near-infrared diffuse reflectance spectroscopy (VNIR-DRS) and mid-infrared diffuse reflectance spectroscopy (MIR-DRS). Both spectroscopy systems can be effectively used for material analysis. However, the MIR-DRS system requires additional cooling system for the spectrograph, which prevents the possibility for on-the-go in-field measurement. On the other hand, VNIR-DRS system is cheaper, more portable, and light weight, hence providing the potential adaptability for on-the-go in-field measurement.

The VNIR range is of particular interests in soil science because the distinctive spectral signature of the overtone and combination of soil minerals mainly occurs within this spectrum range [26]–[29]. Therefore, VNIR-DRS can provide quantitative information about soil properties and a single spectrum could allow simultaneous determination of different soil constitutes and properties [18], [21], [30]–[33].

3.2 Design of the micromachined optical soil probe

Due to soil's highly scattering nature, the intensity of the diffuse reflectance would quickly diminish at locations far away from the soil surface. Therefore, to ensure an effective collection of the diffuse reflectance, the optical probe should be placed directly onto or near the soil surface. Figure 3.3(a) shows the schematic of current VNIR-DRS probe for soil analysis [34]. It consists of a straight optic fiber bundle as the detector to collect the diffuse reflectance. Depending on the actual probe configuration, a small halogen lamp or another straight fiber bundle (coupled to an external light source) serves as the incident light source. It assumes a front-viewing configuration, in which the probe head is in line with the direction of the straight source/collection fiber bundles. Although the front-viewing configuration makes the VNIR-DRS probe suitable for *ex-field* measurements on extracted soil samples, it poses a challenge to *in-field* measurements.

To conduct *in-field* soil measurements, the VNIR-DRS probe will need to be installed into a soil penetrometer (figure 3.3(b)). The soil penetrometer consists of a hollow metal tube with a sharp tip (to facilitate penetrating into the soil). The typical inner diameter of the soil penetrometer is about 1 inch. While the soil penetrometer is pushed into the soil, the VNIR-DRS measurements will be performed at different depths, such that the extraction of the soil sample is avoided. During the soil penetration, the tip of the soil penetrometer is subject to a large compression pressure and also potential abrasion damage from various soil contents. This situation precludes the possibility of directly using the existing front-viewing probes. As a result, miniaturized side-viewing

optical probes are necessary (figure 3.3(b)). Different from the front-viewing configuration, the side-viewing configuration allows the incident light to be delivered and the diffuse reflectance to be collected through a transparent window opened on the side wall of the penetrometer tube.

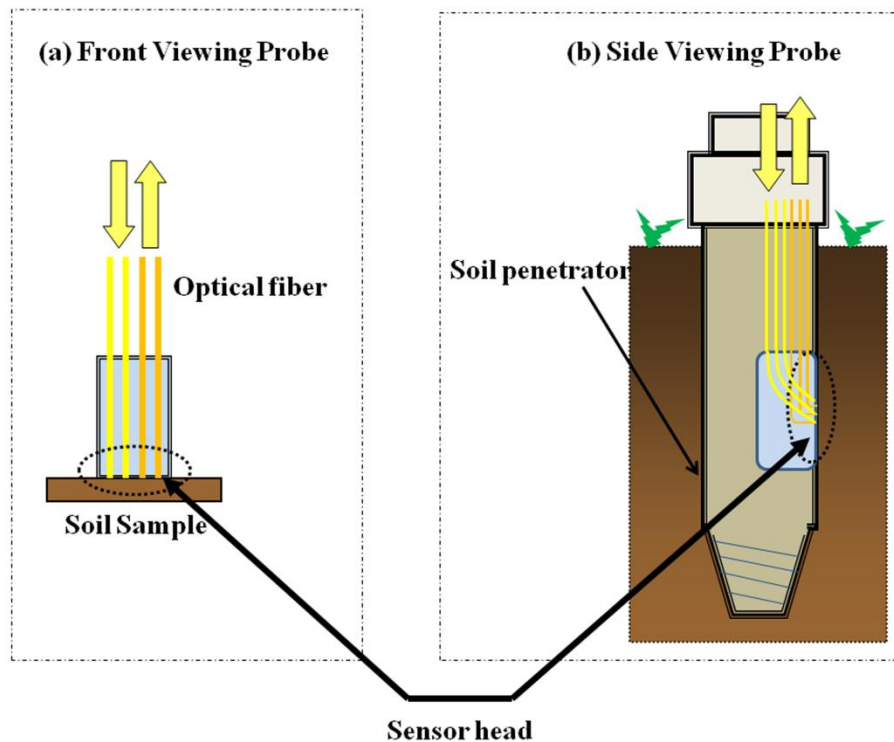


Figure 3.3 Different configurations of VNIR-DRS probe for soil characterization: (a) Front viewing; (b) Side viewing.

Previously, we have demonstrated both front- and side-viewing DRS probes for biomedical applications, which mainly operate within the visible range of 400 - 760 nm [15], [35]. To ensure good signal quality, a high-sensitivity CCD camera was used to capture the diffuse reflectance from various human epithelial tissues with moderate

optical absorption and scattering [36]. However, compared with human tissues, the optical absorption and especially scattering of soils are usually much higher, which result in a much weaker diffuse reflectance signal. On the other hand, due to the requirement of a wide operation spectrum range, the mainstream commercial VNIR-DRS spectrometers currently used for soil analysis generally have a relatively low sensitivity. This situation poses a new challenge on the development of the side-viewing VNIR-DRS probe for *in-field* soil measurement.

Figure 3.4 shows the design of the side-viewing VNIR-DRS probe for *in-field* soil measurements. The fundamental probe structure consists of one source chip for light delivery and one collector chip for receiving the diffuse reflectance. As shown in figure 3.4(a), the source chip has a linear array of micro channels to house a group of optical fibers, which are oriented at certain angle to provide oblique light incidence. For a small oblique incidence angle (e.g., $\leq 45^\circ$), the optical fibers are able to withstand certain degree of bending inside the penetrometer without incurring severe light loss and leakage. As shown in figure 3.4(b), the collector chip is used to receive the diffuse reflectance from a vertical direction above the soil sample surface. This requires a sharp 90° bending of the collection optic fibers within a tight space, which would cause severe light loss and leakage and even mechanical fracture of the optical fibers. To solve this problem, a hybrid optical waveguide structure is used for effective light “bending” and efficient transmission [35]. The hybrid optical waveguide consists of a micro channel coupled with optical fibers (400 μm core diameter and 470 μm outer diameter, 0.22 N.A) at its two terminals. The side walls of the micro channel are coated with a highly

reflective metal layer to prevent light leakage from the micro channel waveguide. The curved portion of the micro channel is responsible for “light bending” and the straight portion of the micro channel serves as the self-alignment structure for fitting the optical fibers. When light is traveling inside the metal-coated micro channel waveguide, it undergoes many times of reflections on the side walls. Because this reflection is not a total reflection, a small reflection loss will inevitably occur during each reflection. When a large number of reflections are encountered (e.g., in longer waveguides), the optical transmission efficiency could be significantly reduced as the result of the accumulation of the reflection losses. Although this was not a concern in our previous developments, it was found to form a performance-limiting factor for the side-viewing VNIR-DRS probe due to the weaker diffuse reflectance signal from the soils and lower sensitivity of the spectrometer. To solve this problem, optical fibers (with the jacket layer removed) are fitted into micro channel waveguide up to the full length of the straight portion at both the input and output terminals. This arrangement provides two major benefits. First, larger portion of the light traveling in the micro channel waveguide can be effectively coupled into the optical fiber for lossless transmission through total internal reflection. Second, the limited acceptance angle of the optical fibers (determined by the numerical aperture (NA)) at the input terminal help to reject specular reflectance from the soil surface, thus resulting in “cleaner” diffuse reflectance signals. Meanwhile, optical fibers with relatively large core diameters (e.g., 400 μm) are used to further facilitate the collection and transmission of the diffuse reflectance. This makes it possible to use fewer collection channels while maintaining a good signal-to-noise ratio (SNR) and high

coupling efficiency. It should be noted that the above probe design allows a reconfigurable probe structure. Multiple source and collector chips can be used and configured in different ways for different applications (figure 3.4(c)).

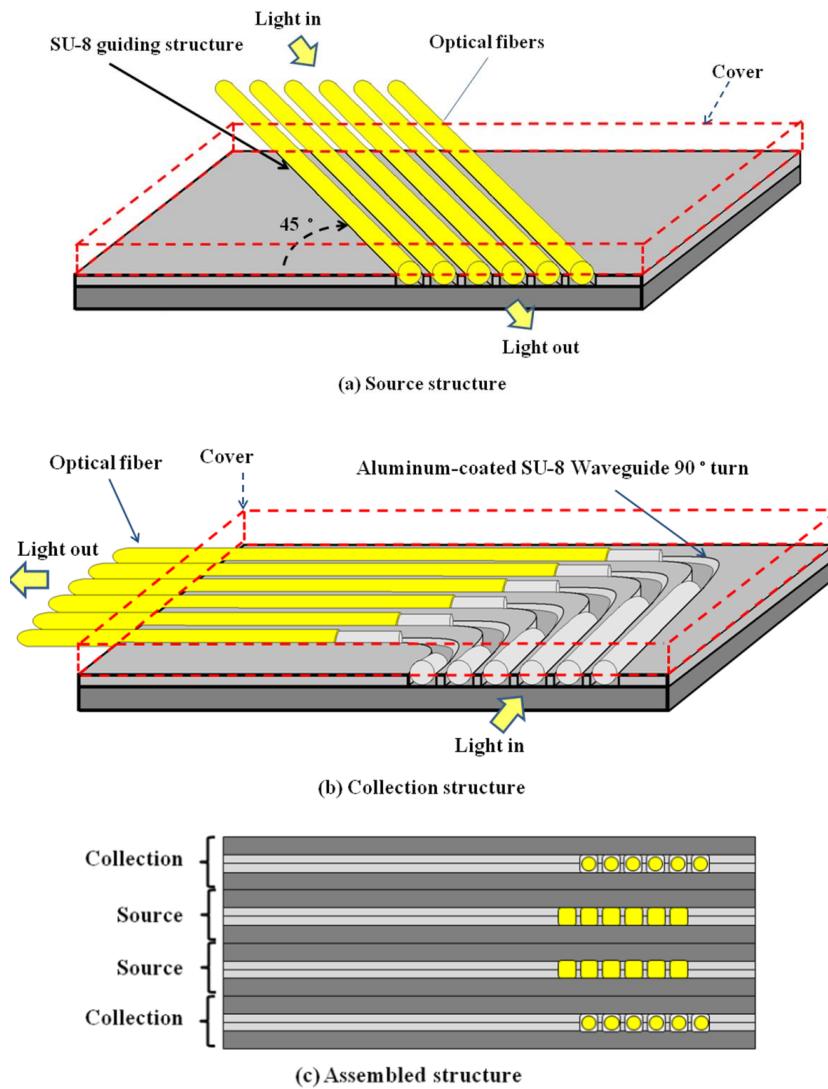


Figure 3.4 Schematic design of the side-viewing VNIR-DRS probe for soil measurement: (a) Source chip; (b) Collector chip; and (c) Front-view of probe assembly with source structures sandwiched between collection structures.

3.3 Fabrication of the micromachined optical soil probe

The fabrication of the side-viewing VNIR-DRS probe starts from the preparation of the source and collector chips. SU-8 resist (MicroChem, Newton, MA, USA) was used to make the source guiding structures and the collection waveguide structures. SU-8 can be directly patterned with photolithography to form a thick and high aspect ratio structure (100 ~ 1000 μm), which results in a simple and low-cost process. To fabricate the SU-8 structures, SU-8 100 resist was first spun on a pre-cleaned silicon wafer (~ 500 μm thick) at a calibrated spinning rate to reach a final thickness of ~ 250 μm . A photolithography process based on the manufacturer suggested recipe was conducted [37]. A slow temperature ramping was maintained to minimize the internal stress and cracking of the SU-8 structures. The bottom and two side walls of the SU-8 structures were coated with a thin aluminum layer. Figure 3.5(a) and Figure 3.5(b) show a fabricated source guiding structure and a collection waveguide structure, respectively. They consist of 6 channels with a width of 500 μm and an inter-channel spacing of 100 μm .

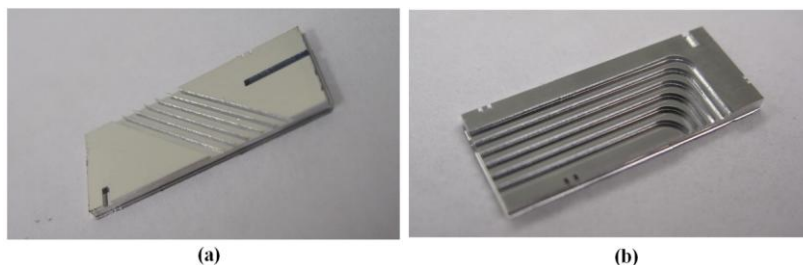


Figure 3.5 Microfabricated aluminum-coated SU-8 structures for making the side-viewing VNIR-DRS probe: (a) Source guiding structure; and (b) Collection waveguide structures.

After the fabrication of the SU-8 guiding and waveguide structures, the probe assembly was conducted. To ensure good light coupling, both ends of all the optical fibers were polished. To assemble the source chip, the incident optical fibers were placed into the SU-8 alignment structures and fixed with optical epoxy (figure 3.6(a)). A second silicon substrate with SU-8 alignment structures (forming a mirror image with those on the first one) was used to form a closed channel to accommodate the incident optical fibers (see figure 3.6(a)). To assemble the collector chip, after their jackets were removed, short sections of optical fibers were placed into the input terminals of the SU-8 waveguide structures and fixed with optical epoxy. The inter-connection fibers (with their jacket removed at the tip) were placed into the output terminals of the SU-8 waveguide structures and fixed with optical epoxy (figure 3.6(b)). Next, a second silicon substrate with SU-8 waveguide structures (forming a mirror image with those on the first one) was used to form a closed waveguide channel to accommodate all the optical fibers (figure 3.4(b)). The above assembly process was repeated to obtain multiple source and collector chips for the final assembly of the probe. Figure 3.6(c) shows a completely assembled prototype side-viewing VNIR-DRS probe. It consists of two source chips and two collector chips stacked together (with the source chips placed in the middle). The overall size of the complete probe is 6 mm × 15 mm × 6 mm, which makes it compact enough to be fitted into a typical soil penetrometer.

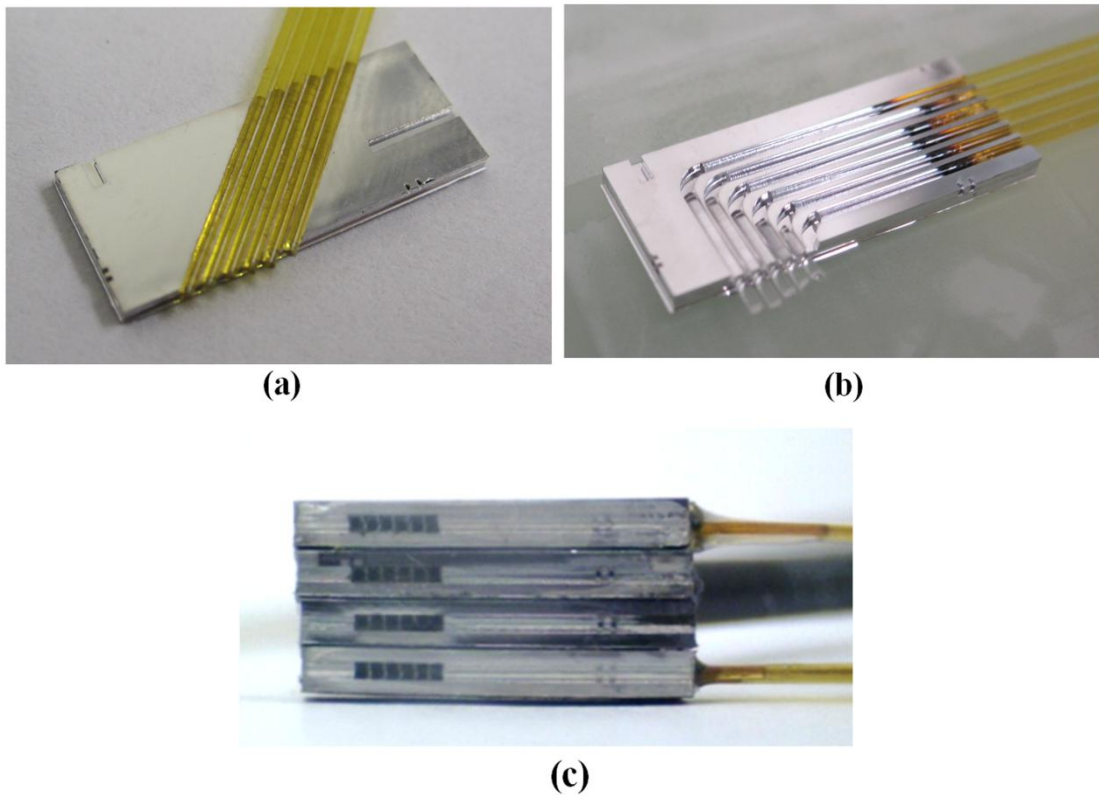


Figure 3.6 Assembly of the side-viewing VNIR-DRS probe: (a) Source chip; (b) Collection chip; and (c) Assembled probe.

3.4 Application: Soil characterization

3.4.1 Introduction to soil analysis

In the past few years, there has been an increasing interest in quantitative evaluation of soil composition for land resource assessment and environmental protection [38]–[44]. This information can provide spatial information of soil and land attributes to support applications such as quantitative soil-landscape modeling, precision agriculture, and global soil C monitoring. Although a number of techniques have been developed for high-resolution horizontal sampling, rapid characterization of soil

composition in the vertical direction is still lacking. The problems faced by soil scientists are the current methods for soil analysis in vertical direction are too expensive and time-consuming. The current standard approach is to conduct a detailed lab analysis along the longitudinal direction of the soil pedons extracted from the test site. However, both the extraction and analysis procedures are laborious, time-consuming and costly. For example, standard soil characterization procedures from the National Soil Survey Center cost about \$2500 per pedon and take 6 to 12 months to process [26]. This creates a challenging situation to appropriate soil and land resources, increasing the difficulty for large-scale sampling tasks or some urgent situations (e.g., for the recent oil spill in the Gulf of Mexico). As a result, methods that can rapidly qualify soil properties (especially in the depth direction) are needed for soil analyzing.

Current methods for soil analysis are soil survey, laboratory measurement, and spectroscopic techniques. In soil survey, the morphology of soil such as field texture, pH, structure, and color are collected. However, this method provides limited information of the soil. From laboratory measurement, functional soil properties can be collected. Functional soil properties are more useful than basic soil properties because they can provide information of the physical, chemical, and biological functions of soils. The spectroscopic technique involves the use of mass spectroscopy, nuclear magnetic resonance, visible, near-infrared, mid-infrared spectroscopy. These techniques are non-destructive, rapid, and inexpensive. The preservation of the soil integrity enables soil samples to be measured many times with different techniques. The preparation of soil sample is shorter compared with the laboratory method. In addition, a complete scan of

the soil sample may take about few seconds. The total cost of the spectroscopic method is much less than other methods when a large amount of samples have been scanned.

VNIR-DRS has been widely used for fast characterization of the composition of different soils [22], [26], [45]–[48]. It has been demonstrated that it can be quite effective in predicting the physical, chemical and the biological properties of air-dried soil samples in the lab [31]. Meanwhile, the feasibility of using VNIR-DRS for *in-situ* quantification of the clay content under different soil conditions have also been investigated, which shows that it is capable of predicting soil clay content at variable soil moistures and particle sizes [30].

To conduct VNIR-DRS, a special optical probe is needed to collect the diffuse reflectance from the soil sample in contact. However, existing optical probes are only suitable for *ex-field* measurements on prepared soil samples after being extracted from the ground. Although fast soil characterization is possible, the tedious extraction steps still cannot be avoided. In addition, the soil sample preparation is time-consuming and laborious. Therefore, to fulfill the potential of VNIR-DRS in soil characterization, the developed micromachined optical probes was used to enable *in-field* measurements (without the need of soil extraction and sample preparation).

3.4.2 Testing setup for soil characterization

The measurement setup consists of a halogen lamp as the white light source, the side-viewing VNIR-DRS probe, an ASD LabSpec 5000[®] VNIR spectrometer (Analytical Spectral Devices, Inc., Boulder, CO, USA) and a personal computer (figure 3.7). The VNIR spectrometer operates over a wide wavelength range from 350 nm to

2500 nm with a sampling resolution of 2 nm. The source fiber bundle of the side-viewing VNIR-DRS probe is connected to the output of the white light source through a SMA connector to deliver oblique light incidence onto the soil sample surface. The collection fiber bundle of the side-viewing VNIR-DRS probe is connected to the input of the spectrometer to resolve the diffuse reflectance spectra. The spectrometer is linked to the personal computer through an RS-232 interface for data acquisition and transfer.

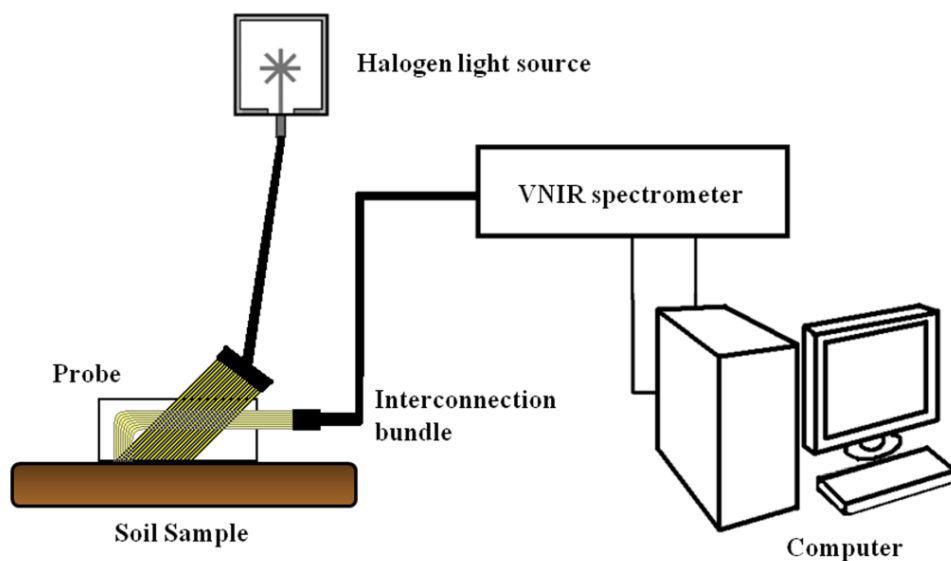


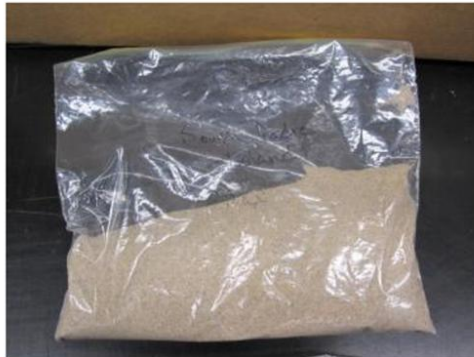
Figure 3.7 Schematic of the VNIR-DRS measurement setup.

Prior to the soil measurement, the entire measurement setup was calibrated with a spectralon panel with 99% reflectivity as the white reference. After the calibration, the side-viewing VNIR-DRS probe was used to collect the diffuse reflectance of several soil samples. A typical soil sample is shown in figure 3.8(a). On each soil sample, VNIR-

DRS measurements were also performed using the commercial front-viewing VNIR-DRS probe (ASD[®] 135680 bifurcated reflectance probe) for comparison.

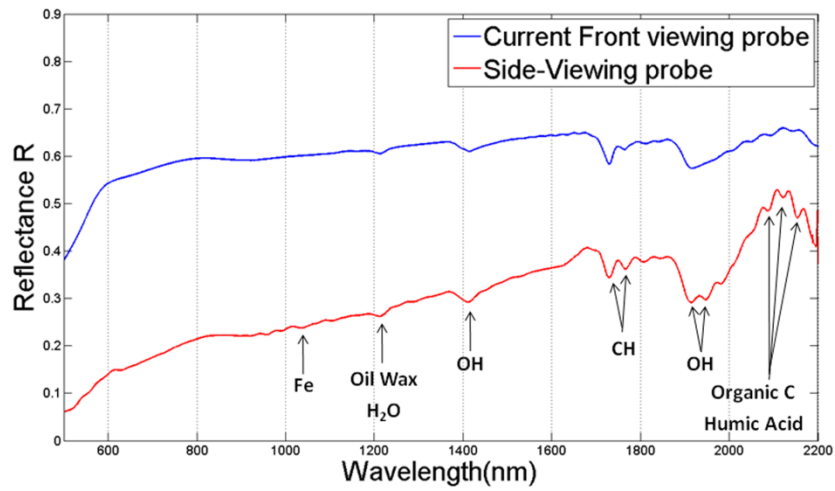
3.4.3 *Experimental results and discussion*

After all the measurements were complete, the diffuse reflectance spectra were digitally filtered using a Remez function with Park-McClellan algorithm in Matlab[®] (The MathWorks, Natic, MA, US) to eliminate high frequency noise. Due to the limitation in the transmission wavelength range of the optical fibers used in probe construction, the diffuse reflectance spectra below 500 nm and above 2200 nm have a low signal to noise ratio (SNR) and thus were removed (figure 3.8(b)). To better analyze the diffuse reflectance data, absorption spectra were derived as the natural logarithm of the diffuse reflectance (figure 3.8(c)).

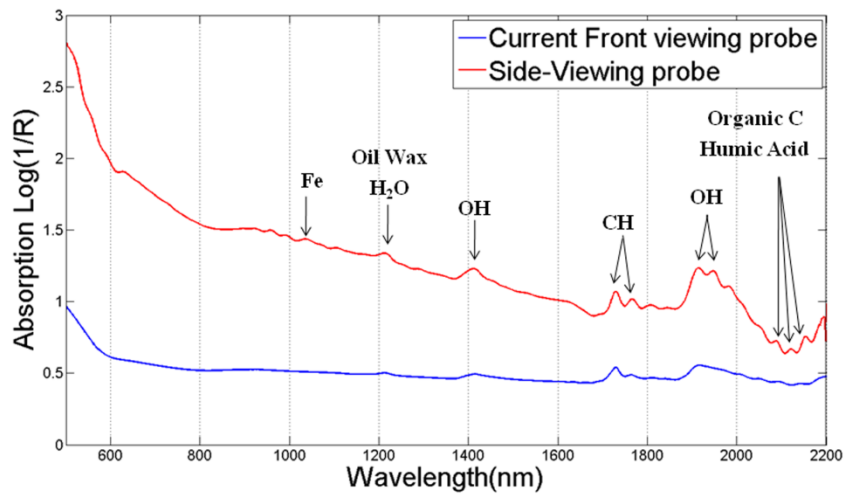


(a)

Figure 3.8 (a) A representative soil sample for VNIR-DRS measurements; (b) Measured diffuse reflectance spectra; and (c) Calculated absorption spectra of the soil sample shown in figure 3.8(a).



(b)



(c)

Figure 3.8 Continued.

As shown in figure 3.8(b) and figure 3.8(c), similar diffuse reflectance and absorption spectra were obtained from the side-viewing VNIR-DRS probe and its front-viewing counterpart, except that a lower magnitude of diffuse reflectance and more

pronounced absorption peaks exist in the spectra from the side-viewing VNIR-DRS probe. We believe that they are possibly caused by the different configuration of the light incidence and collection in these two probes. As shown in figure 3.3(a), the front-viewing probe utilizes optical fiber bundles, in which the incidence and collection fibers are closely packed in the same orientation with a core-to-core distance of $\sim 250 \mu\text{m}$. Therefore, this closely-packed configuration collects certain portion of the specular reflectance light and diffuse reflectance with a shorter diffusion length and stronger intensity. On the other hand, in the side-viewing probe (figure 3.3(b)), the incident fibers and collection fibers are oriented at different angles with respect to the soil surface, respectively. In addition, they are also separated by a larger gap ($\sim 1.5 \text{ mm}$). The larger gap provides a longer path for the incident light to be fully diffused and absorbed before it reaches the collection fibers. More absorptions and scatterings occur along the light path and the collected diffuse reflectance intensity is reduced. As the relatively lower reflectance is not an issue for soil analysis that uses the first and second derivative of the absorbance, this longer distance has two extra beneficial effects. First, the diffused light has more interactions with the medium, so the spectrum signature of the medium will be more dominant. Second, the larger gap can assure less unwanted specular reflectance being collected that masks the diffuse reflectance of interest, and also contains higher diffuse reflectance component from the collected reflectance; thus, the side-viewing probe has a higher sensitivity to the optical absorption of the different soil components. The gradually increased reflectance from shorter wavelength to longer wavelength is also related to the scattering during light diffusion. Scattering pattern is a function of the

particle size and the wavelength. In our measurement, light with shorter wavelength has larger amount of scattering and less diffuse reflectance to reach the detector. The typical absorption peaks of soils have been well studied for soil analysis [49]. For example, the ones around 1400 nm and 1900 nm are due to the O-H group in a water molecule, while those close to 1700 nm and 2100 nm are related to the C-H group in humic acid. Absorption peaks around 1040 nm (due to iron content) and 2100nm (due to organic carbon) are not obvious from the spectrum of the front-viewing probe, but it is evident in that from the side-viewing probe. From the diffuse reflectance spectra, quantitative information about soil composition can be further extracted or estimated based on a number of statistical-library based methods [21], [24].

3.5 Conclusions

A prototype side-viewing optical probe has been successfully designed, fabricated and tested for VNIR-DRS measurements on soil samples. Its unique small dimension, side-viewing capability and wide optical transmission spectrum make it suitable for *in-field* VNIR-DRS measurement. Using this probe, diffuse reflectance of soil samples has been successfully measured, which matches well with those obtained with the existing commercial probe. Due to the probe configuration, the side-viewing VNIR-DRS probe can provide similar or potentially superior performance than the commercially-available front-viewing VNIR-DRS probe. Meanwhile, the probe collects diffuse reflectance light within area around 4 mm × 3 mm to achieve better signal to noise ratio, while this could sacrifice the spatial resolution of the probe. Further

development will focus on soil characterization based on the measurement and attach the sensor probe on an penetrometer to conduct real-time *in-field* VNIR-DRS.

4. MICROMACHINED SILICON ACOUSTIC DELAY LINES FOR ULTRASONIC AND PHOTOACOUSTIC IMAGING APPLICATIONS*

4.1 Introduction

4.1.1 Ultrasound transducer array receiving system

Ultrasound transducer arrays have been widely used in ultrasound and photoacoustic imaging [50]. In either case, the transducer array receives the incoming ultrasound waves from the source point(s), and the received signals are amplified and digitalized by the data acquisition (DAQ) electronics simultaneously (figure 4.1).

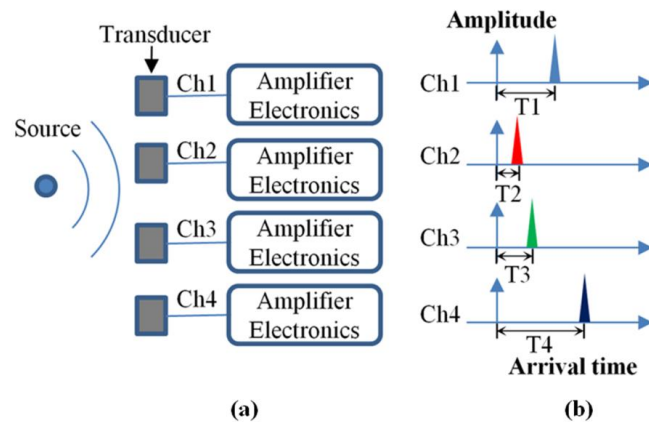


Figure 4.1 Ultrasound transducer array system: (a) Transducer array setup; (b) Signals received by each transducer. The arrival time is determined by the travel distance and acoustic velocity in the medium.

*@ 2013 IOP Reprinted with permission from Cheng-Chung Chang, Young Cho, Lihong Wang, and Jun Zou, "Micromachined silicon acoustic delay lines for ultrasound applications," *Journal of Micromechanics and Microengineering*, 23(2), 025006, 2013. doi:10.1088/0960-1317/23/2/025006

To achieve high imaging resolution and speed, large high-frequency transducer arrays and complex DAQ electronics will be needed [51], [52]. As a result, the entire ultrasound imaging system could become costly.

4.1.2 Ultrasound delay line receiving system

To address this issue, a new ultrasound receiving system design using acoustic time delay was demonstrated [53]. As shown in figure 4.2(a), a series of acoustic delay line detectors are used to replace the transducer elements. Each delay line receives the acoustic wave (figure 4.2(b)) and introduces proper delay time for the signal to reach the other end (figure 4.2(c)), where a single transducer is connected to serially receive the time-delayed signals (figure 4.2(d)). The delay line system converts multi-channel parallel signals into single-channel serial signals and therefore requires fewer transducer elements and DAQ channels. It could be a more economical new approach for ultrasound receiving system design.

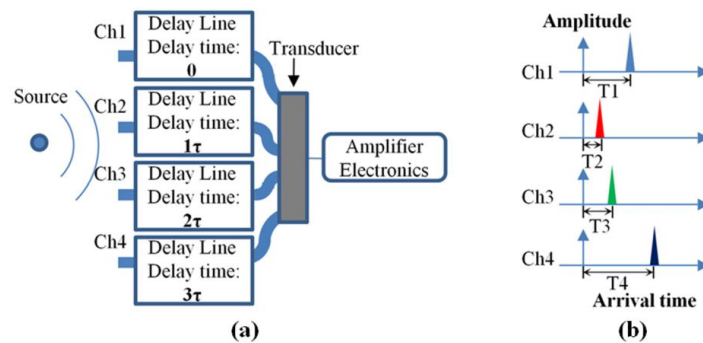


Figure 4.2 Delay line receiving system: (a) Delay lines with single receiving transducer; (b) Ultrasound signals before entering the delay lines; (c) Ultrasound signals with proper delay time; and (d) Ultrasound signals received by the single transducer.

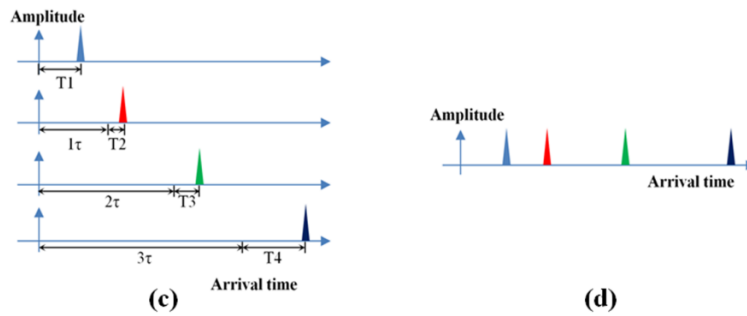


Figure 4.2 Continued.

Different kinds of delay lines have been investigated by researchers. Delay lines with different shapes have been characterized, including wire, tape, and polygon. Various medium have been used for delay line construction. Liquid delay lines using mercury have found application in memory. Solid delay lines using quartz, metal and optical fibers have been applied to radar system. The acoustic propagation in these delay lines were also studied [55]-[57]. However, delay line systems for ultrasound imaging applications have never been implemented. To validate the concept, an optical fiber delay line system was built prior the use of silicon as the delay line material.

4.2 Optical fiber delay line system and its limitations

Optical-fiber delay lines are most desirable due to their low acoustic loss, small dimensions, and abundance of materials. The acoustic velocity and attenuation were first measured by an ultrasound through-transmission setup with 1 MHz transducers, where the sending transducer (V303, Olympus NDT, Waltham, MA, USA) and the receiving transducer (V303, Olympus NDT, Waltham, MA, USA) were connected on the two ends of an optical fiber with given length (figure 4.3). The sending transducer generated

an ultrasound pulse controlled by a pulser-receiver unit (5072-PR, Olympus NDT , Waltham, MA, USA). The ultrasound signal travelled through the optical fiber sample and was received by a receiving transducer at the other end. The received signal was amplified by the pulser-receiver unit and displayed on the oscilloscope. By measuring the travelling time inside the optical fiber, the acoustic speed in the optical fiber can be determined. By measuring the signal amplitude with respect to the length change, the acoustic attenuation can be derived. As shown in figure 4.4, the acoustic velocity and attenuation were calculated. The measurement result shows that the acoustic velocity is around 5108 m/s and the attenuation is 0.2 dB/cm.

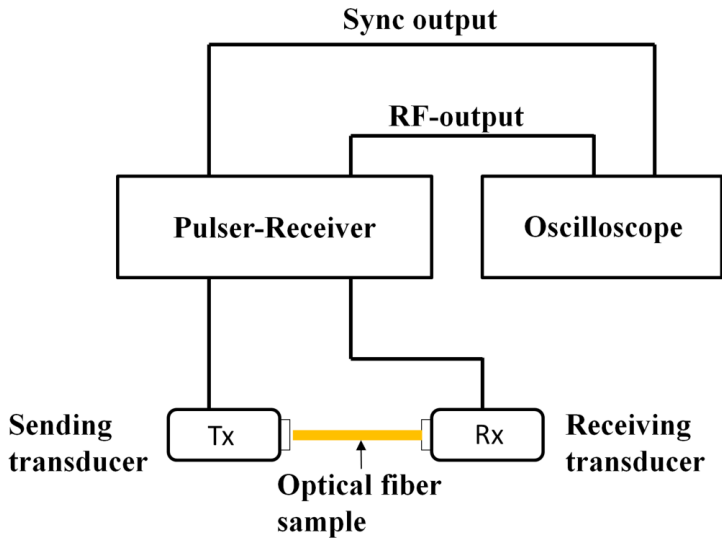


Figure 4.3 Ultrasound through-transmission setup

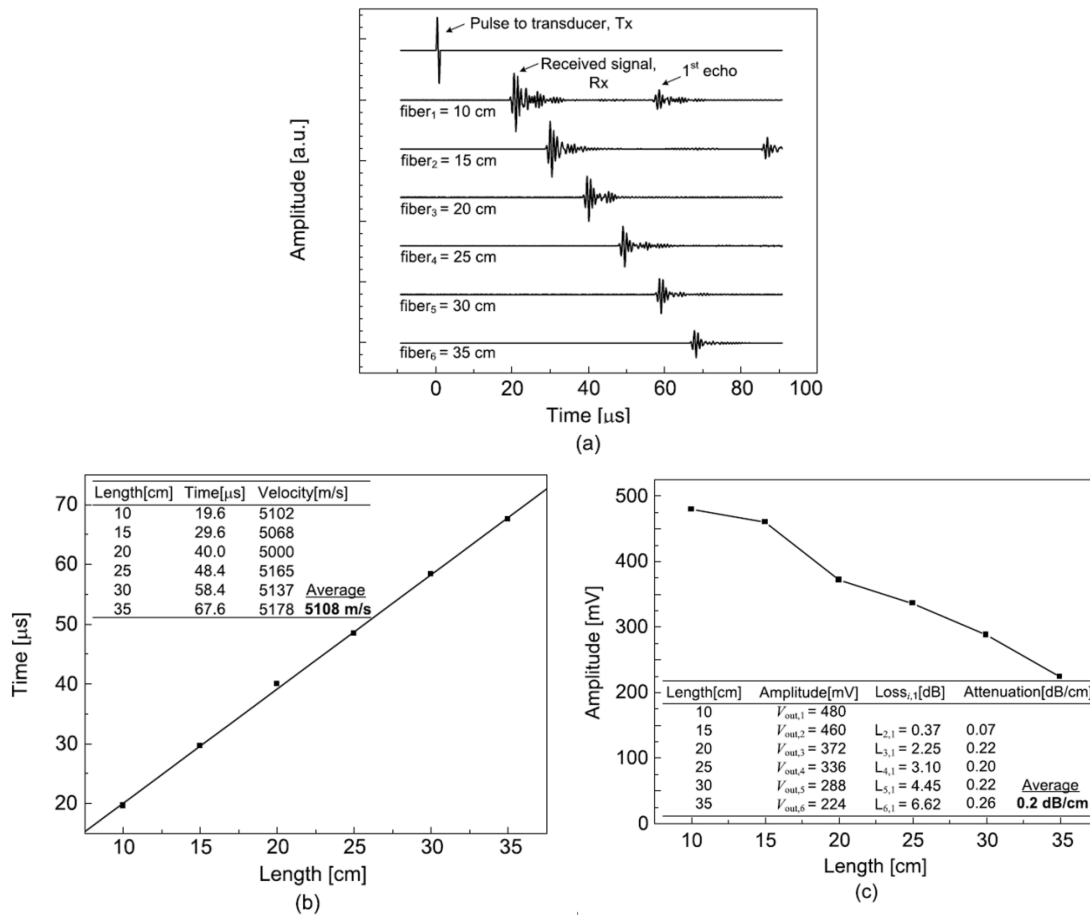


Figure 4.4 Acoustic velocity in optical fiber. (a) Ultrasound signals arrive at different time with respect to the fiber length. (b) The acoustic velocity is determined by the length/time ratio and is about 5108 m/s.*

*Murat Kaya Yapici, Chulhong Kim, Cheng-Chung Chang, Mansik Jeon, Zijian Guo, Xin Cai, Jun Zou, and Lihong V. Wang, "Parallel acoustic delay line for photoacoustic tomography," Lihong V. Wang, Joseph R. Lakowicz, John A. Parrish, Bruce J. Tromberg, Editors, Journal of Biomedical Optics 17(11), 116019, 2012.

Copyright 2012 Society of Photo-Optical Instrumentation Engineers. One print or electronic copy may be made for personal use only. Systematic electronic or print reproduction and distribution, duplication of any material in this paper for a fee or for commercial purposes, or modification of the content of the paper are prohibited.

<http://dx.doi.org/10.1117/1.JBO.17.11.116019>

Based on the measurement results, a 16-channel optical fiber delay line system was designed. The fiber length and ultrasound signal arrival time information are shown in table 1. Based on the ultrasound signal duration ($\sim 12 \mu\text{s}$), the signal arrival time difference was designed to be $12 \mu\text{s}$, which is long enough to prevent signal overlapping. The fiber length were also carefully designed to prevent the echo signal from the shortest channel (arrived at $132 \mu\text{s}$) to interfere with the ultrasound signal from the longest channel (arrived at $128 \mu\text{s}$).

Table 1 Fiber length and signal/echo arrival time for each channel.

Channel #	Fiber length (mm)	Signal arrival time (μs) / 1 st echo arrival time
1	225	44 / 132
2	286	56 / 168
3	347	68 / 204
4	409	80 / 240
5	470	92 / 276
6	531	104 / 312
7	593	116 / 348
8	654	128 / 384

The 16-channel delay line system was constructed by using two 8-channel delay line systems in parallel (figure 4.5). The optical fibers were held in air with styrofoam supporting structure in the middle and acrylic holder at the input and output terminals. The optical fibers were polished in two ends to insure good acoustic coupling. The optical fiber delay line system was later tested with the ultrasound through-transmission setup, with one input transducer for sending ultrasound signals and two output transducers to receive the signals. As shown in figure 4.6, each output terminal clearly

shows 8 distinctive ultrasound signals, which implies multiple-channel ultrasound signals can be delayed and received serially with a single transducer.

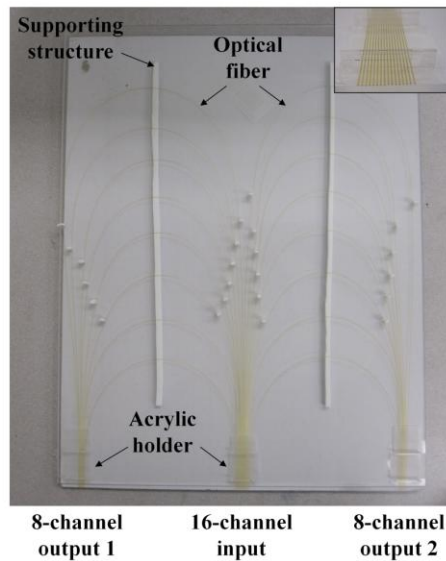


Figure 4.5 Optical fiber delay lines system with 16-channel common input and two 8-channel outputs. Inset: Close up look of the 16-channel input terminal with acrylic holder.

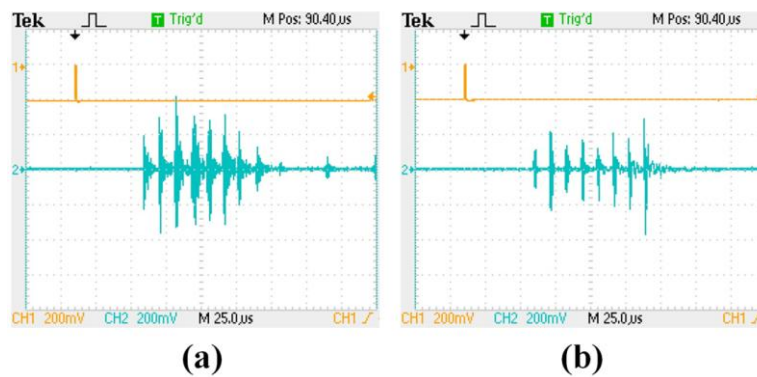


Figure 4.6 Ultrasound signals received by the 16-channel optical fiber delay line system. (a) Signals received by the 8-channel output terminal 1. (b) Signals received by the 8-channel output terminal 2.

Although the optical fiber delay line system validate the delay line receiving system concept by effectively receiving multiple-channel signals with two output transducers, the optical fiber delay line system still has several limitations. Because of the high acoustic velocity of quartz (e.g., ~6000 m/sec), the length of the optical-fiber delay lines need to be very large to provide sufficient delay time [53]. Even by dividing 16 channels into two 8 channel systems, the longest channel is still 40 cm longer than the shortest channel. With the additional expense of two receiving transducers and to prevent signal cross talk and mechanical fracture of optical fibers, the required space for the optical fiber delay line system is huge. The plastic jacket layer would cause extra attenuation and distortion of the acoustic signals. In addition, the manual assembly and alignment of the optical fibers are very tedious and inaccurate. To address these issues, a new micromachined silicon acoustic delay lines was developed, which capitalize upon the extremely low acoustic loss of single-crystalline silicon and the micro scale precision of micromachining process. Compared with the optical-fiber delay lines, the micromachined silicon delay lines offer higher transmission efficiency, more compact and functional structures, easier assembly, and mass production. By using the silicon delay lines, two acoustic delay line systems (parallel and serial) and a delay line probe have been successfully demonstrated to create controlled time delays in multiple channels of ultrasound signals, which allows their reception with a single-element transducer.

4.3 Design of silicon acoustic delay line

Silicon is considered as the delay line material for three reasons. First, it has extremely low attenuation in the MHz range ($\sim 10^{-4}$ dB/mm·MHz² @ 10 MHz) [57]. The dispersion of ultrasound wave propagation can be minimized with proper design [58]. Second, it is a mechanically strong material with excellent thermal stability. Third, it is compatible with well-developed microfabrication and micromachining technologies. Multiple delay line structures can be simultaneously fabricated with high precision in a compact space without tedious assembly process.

The dimension of the delay lines affects the transmission of the acoustic signal. To operate only in the lowest longitudinal mode, the dimension of a rectangular-shaped delay line should satisfy $(df/V_0) \ll 1$, where d is the width or thickness of the delay line (whichever is smaller), f is the frequency of the signal, and V_0 is the acoustic velocity of the delay line material [58]. For example, suppose the acoustic velocity in silicon is around 8430 m/s [59], the dimension for the single mode delay line should be much smaller than 3.7 mm for a 2.25 MHz center frequency wave transmission. In this work, all the fabricated delay line structures have a width of 500 μm and a thickness of 250 μm .

In the delay line system, each channel has a designated delay time, which is controlled by the travelling length of the signal. Two different layouts, parallel and serial, can be applied for silicon delay lines. In the parallel design, each channel carries one signal with a specific propagation path and delay. All the channels connect to the same transducer in a parallel fashion. Signal from each channel arrives at the transducer at different time (figure 4.7). Since the acoustic velocity of silicon is high, the delay lines

need to be long to achieve sufficient delay time in each channel. To satisfy the length requirement and remain compact in size, each channel is made of multiple U-turns with different radius winding together. In the serial design, all channels merge into the main channel at different locations with Y-shaped junctions. The delay time is controlled by the travelling length in the main channel (figure 4.8).

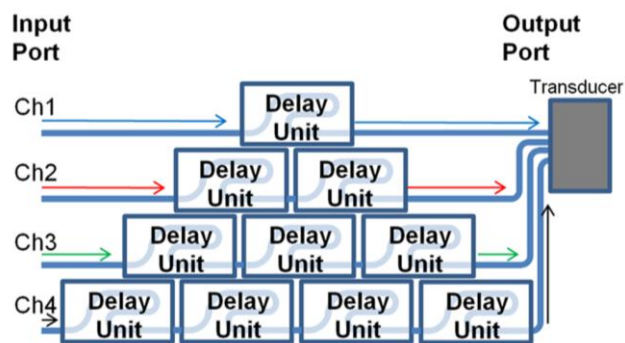


Figure 4.7 Schematic of parallel delay lines.

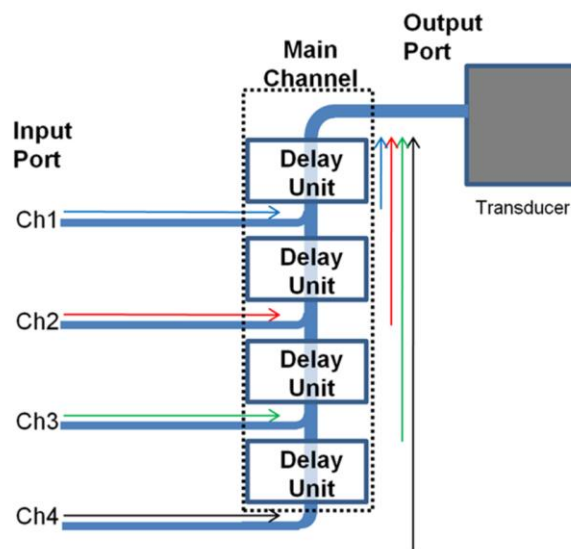


Figure 4.8 Schematic of serial delay lines.

4.4 Materials and methods

To ensure a good design of the silicon-based delay lines, the acoustic properties of silicon, such as the velocity and attenuation were first characterized. In the second step, the wave propagation in the three fundamental building-block structures (straight line, U-turn, and Y-junction) in the parallel and serial delay lines were investigated.

4.4.1 Delay line structure fabrication

The delay line structures were fabricated using 250- μm -thick 4-inch {100} single-crystalline silicon wafers. The silicon wafer was first coated with a 300 nm thick aluminum layer using e-beam evaporation. The aluminum layer was patterned using photolithography, which served as a mask for silicon etching. The etching of the delay line structures was conducted using a cryogenic deep reactive ion etching (RIE) process on a Plasmalab[®] 100 RIE system (Oxford Instruments, Oxfordshire, UK). The cryogenic etching process can provide high etch rate and vertical sidewall profile [60]. The etching parameters can be found in Appendix A. The silicon wafer was first glued on an aluminum-coated dummy wafer with Fomblin oil (Fomblin 06/6, Solvay Plastics, Brussels, Belgium). The whole sample was later clamped on the chuck cooled down to -120° Celsius by using liquid nitrogen with liquid helium backing between the dummy wafer and the chuck. The RIE etching was conducted for 60 minutes to completely etch through the silicon wafer. After etching, the delay line structures were carefully detached from the etched silicon wafer.

4.4.2 *Characterization setup*

As shown in figure 4.9, the silicon samples are supported by acrylic plates with small holding structures to minimize signal leakage. The acrylic plates together with the sample and a transducer are fixed on a three axis translation stage. The acoustic wave signal is directly generated in silicon through the photoacoustic effect [61].

Photoacoustic effect is the generation of acoustic wave by pulsed light excitation. The material absorbs light energy and heats up, and the sudden thermal expansion creates pressure waves that radiate away from the excitation spot. Using photoacoustic setup, the acoustic wave can be generated at any points on the sample by changing the location of the laser focal point. The small laser focal spot is particularly suitable for acoustic wave excitation in sub-millimeter structures. Nanosecond laser pulses with 1064 nm wavelength are delivered onto the sample from a Nd: YAG laser (Quanta-Ray Pro-200, Newport Corporation, Irvine, CA, USA) with a 10 Hz repetition rate and 10 nanosecond pulse width. A shutter controlled by the trigger in the laser system is used to allow single pulse excitation. The laser is attenuated by a half-wavelength wave plate, a dielectric polarizer, two filters, and focused by an objective lens to form a beam spot of 10 μm in diameter. The focused pulse energy is 280 J/mm^2 with 10 percent variance. Silicon sample absorbs light energy and induces a pressure wave in all directions. The pressure wave propagates along the silicon delay line structure and is received by an ultrasound transducer with a 2.25 MHz center frequency (V105, Olympus NDT, Waltham, MA, USA). The ends of the silicon are polished to create flat contact surfaces and mineral oil is applied at the silicon-transducer interface to improve contact and coupling efficiency.

The received signal is amplified by the pulser-receiver unit (5072-PR, Olympus NDT , Waltham, MA, USA) with 1 MHz high pass filter and 10 MHz low pass filter. The acoustic signal and the laser trigger signal are displayed on an oscilloscope. The data are collected for three times and averaged for each measurement. A similar setup was used with ultrasound simulation software (Wave2000, Cyberlogic Inc., New York, USA) to simulate ultrasound propagation.

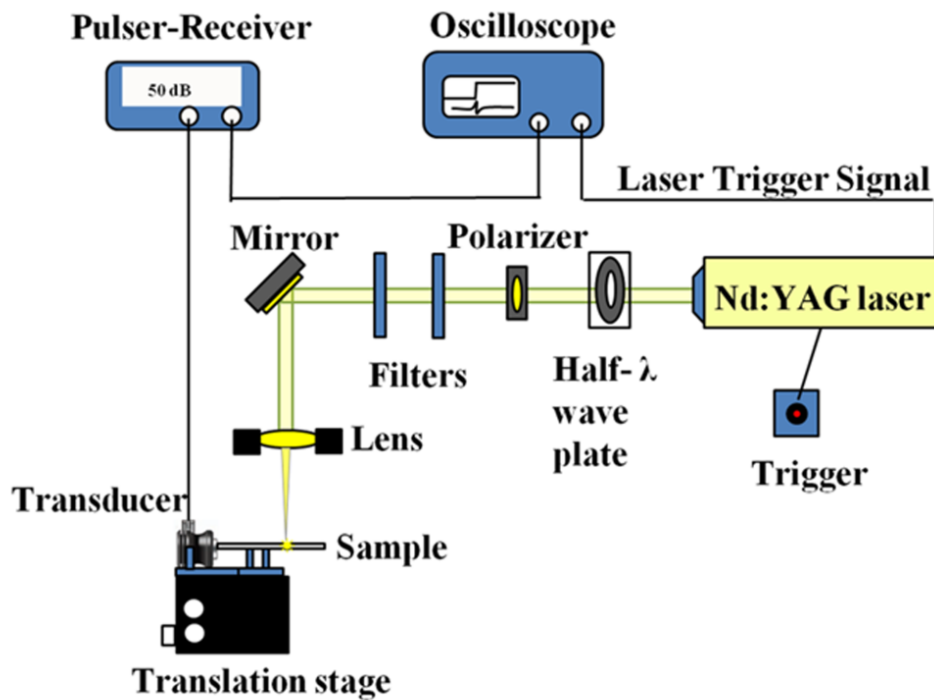


Figure 4.9 Schematic of the photoacoustic excitation setup.

4.5 Experiment and results

4.5.1 *Acoustic properties: Attenuation and velocity*

A 7-cm-long straight silicon delay lines etched along the $\langle 1\ 1\ 0 \rangle$ crystal direction was used to measure the acoustic attenuation and velocity (figure 4.10(a)). Laser light was focused on the delay line at a particular distance away from the transducer (figure 4.10(b)). The generated acoustic wave propagates in two directions. The wave traveling toward the transducer is received first, and the wave traveling away from the transducer is reflected on the other end and reaches the transducer at a later time. To avoid the reflected signal to mix with the first signal, the measuring locations were kept away from both ends of the delay line. Signals from eight different points with ~ 5 mm intervals were measured along the delay line. The received signals were used to determine the acoustic velocity and attenuation. The velocity can be calculated based on the ratio of the travelling length and arrival time. The averaged velocity for a straight delay line is determined to be ~ 8454 m/s (figure 4.11(a)). The attenuation can be determined by measuring the peak to peak amplitude change of the signal. As shown in the simulation results in figure 4.11(b) and the experimental results in figure 4.11(c), there is no significant change in amplitude as the travelling length increases. The small variation is due to the tolerance of laser power and the difference in surface condition at the focus location. The result implies that at 2.25 MHz, the acoustic attenuation is extremely low and can be negligible.

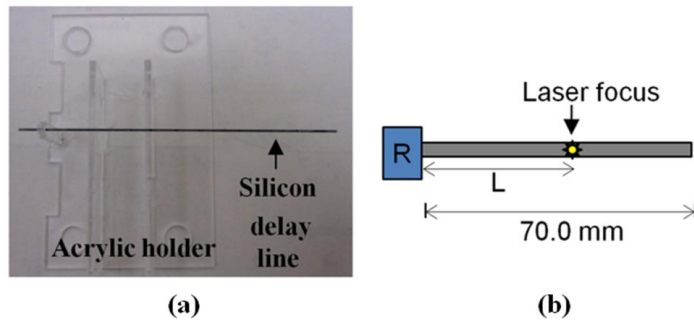


Figure 4.10 Straight silicon delay line. (a) Sample; (b) Measurement setup: Receive signal from focus points along the straight delay line. L: Traveling length (distance from the focal point to the transducer). R: Receiving transducer.

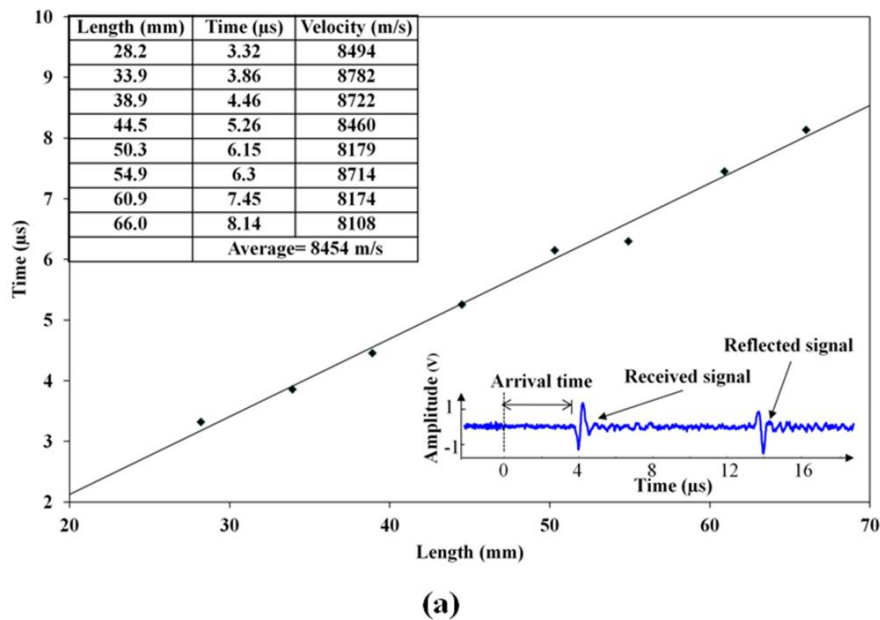
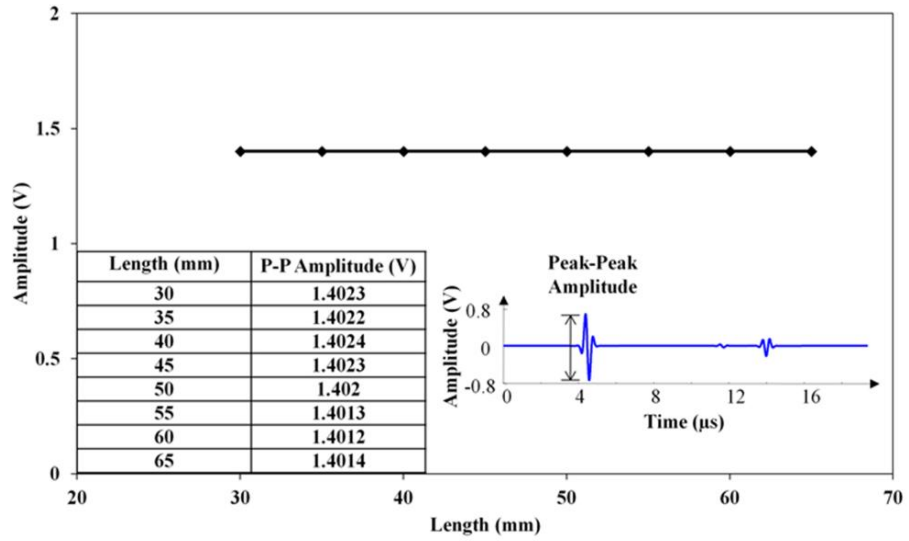
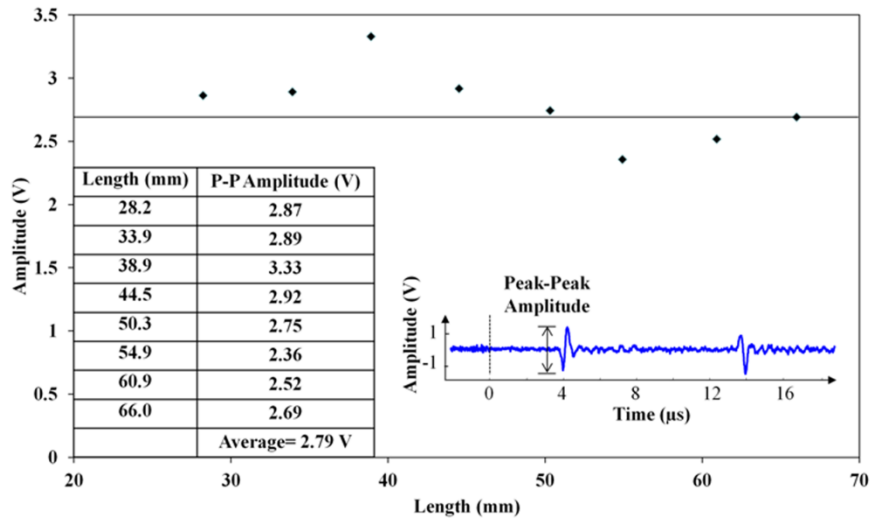


Figure 4.11 Straight silicon delay line measurement. (a) Plot of the arrival time versus traveling length. The average velocity in straight silicon delay line is ~8454 m/s. Inset: Representative signal shape from L: 28.2 mm; (b) Simulation results of signal peak–peak amplitude versus traveling length. Inset: Representative signal shape from L: 30 mm; and (c) Experimental results of signal peak–peak amplitude versus traveling length. Inset: Representative signal shape from L: 28.2 mm.



(b)



(c)

Figure 4.11 Continued.

4.5.2 Propagation in U-turn structures with different curvature

As shown in figure 4.12(a), U-turn structures with six different bending radii of curvature were attached to the receiving transducer. Each U-turn structure consists of two straight portions (with lengths of 3 cm and 1 cm) connected by a 180° round portion. The laser focal spot was positioned on the two junction points (i.e., points A and B in figure 4.12(b)) between the straight portion and the bending portion, respectively. The first-arrival signal from point A only travels in the 3-cm-long straight portion before reaching the transducer. The first-arrival signal from point B travels in both the curved and straight portion. Since the attenuation of silicon is very low at 2.25 MHz, any difference between these two signals is mainly due to the bending portion. Therefore, the insertion loss of the bending portion can be estimated by comparing the peak-to-peak amplitude of these two signals. As shown in figure 4.13, the amplitude ratio decreases as the bending radius decreases. The reduction is due to the mode conversion and direct reflection of the wave. As a longitudinal wave hits on the wall of the delay line with an angle, the wave will go through reflection. Part of the reflected wave will remain in longitudinal mode and part of the wave will go through mode conversion and become transverse mode, which cannot be effectively detected by the longitudinal mode transducer. In addition, when the bending radius is small, some of the waves will be reflected back and never reach the transducer. It is also noticed that the signal wave form is similar to the signal from a straight delay line and no signal distortion is observed. However, after receiving the first peak and the reflected peak from the other end, the signal becomes more distorted as the radius decreases.

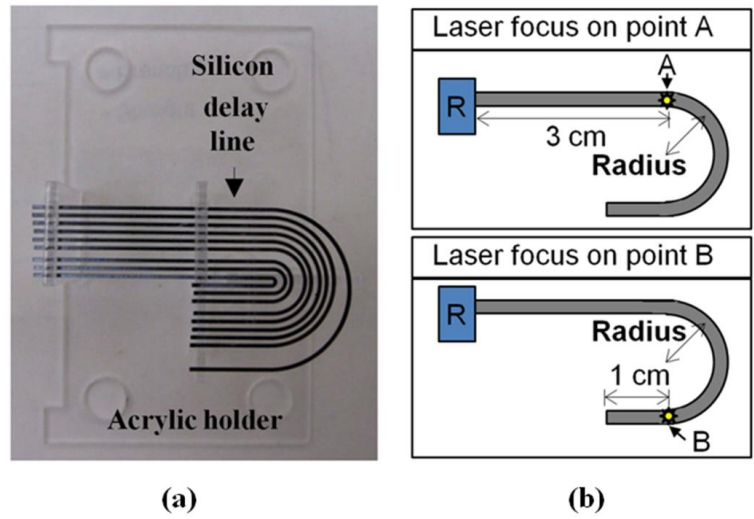


Figure 4.12 U-turn structure measurement. (a) Sample; (b) Measurement setup: Receive signals from different focus points, A: without bending, B: with bending.

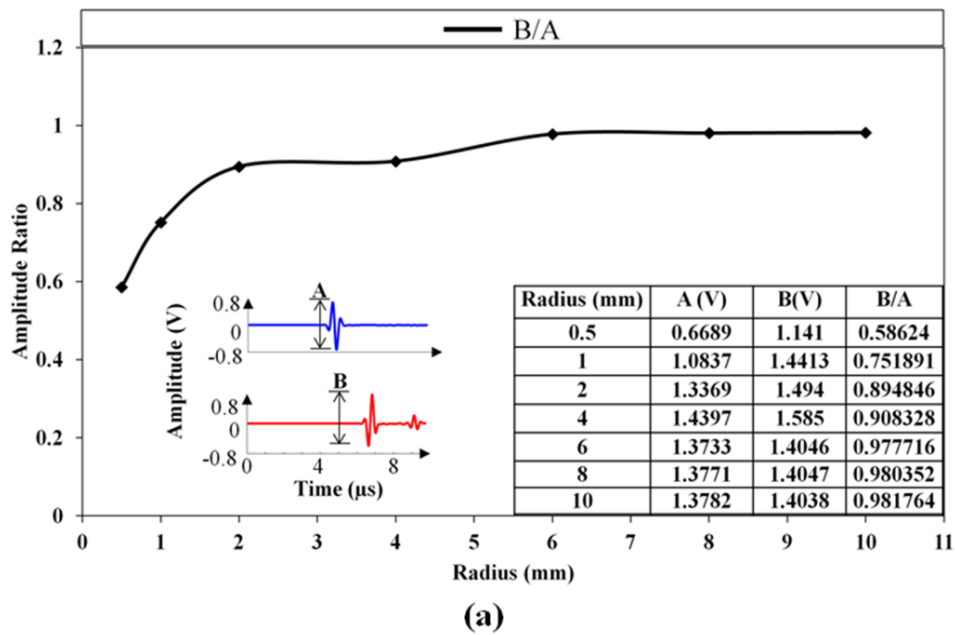


Figure 4.13 U-turn structure measurement. (a) Simulation results of radius versus amplitude ratio. Inset: Representative signal shape from turning with 6 mm radius; and (b) Experimental result of radius versus amplitude ratio. Inset: Representative signal shape from turning with 6 mm radius.

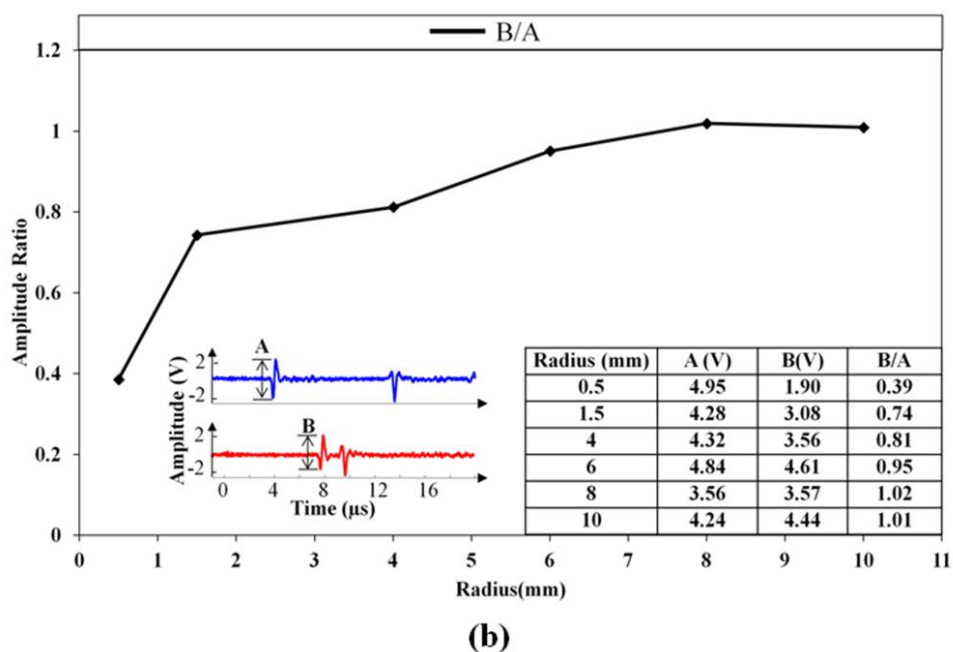


Figure 4.13 Continued.

4.5.3 Propagation in Y-junction structures with different angles

Six Y-junction structures with cross angles ranging from 5 degrees to 30 degrees (with a 5-degree increment) (figure 4.14(a)) were tested. Each structure has a 4-cm-long straight line with a 3-cm-long branch. The intersection point is located 1 cm away from the transducer (figure 4.14(b)). The laser focal spot was positioned at three points one at a time to determine the insertion loss at the junction. Signal generated from point A does not go through the junction and is used as the reference signal. Signal from point B comes from the branch and enters the straight line through the junction. Signal from point C is from the straight line and passes the junction. By comparing the peak-to-peak amplitude of the signals from the three points, the insertion loss of the straight and branch parts at the junction can be estimated.

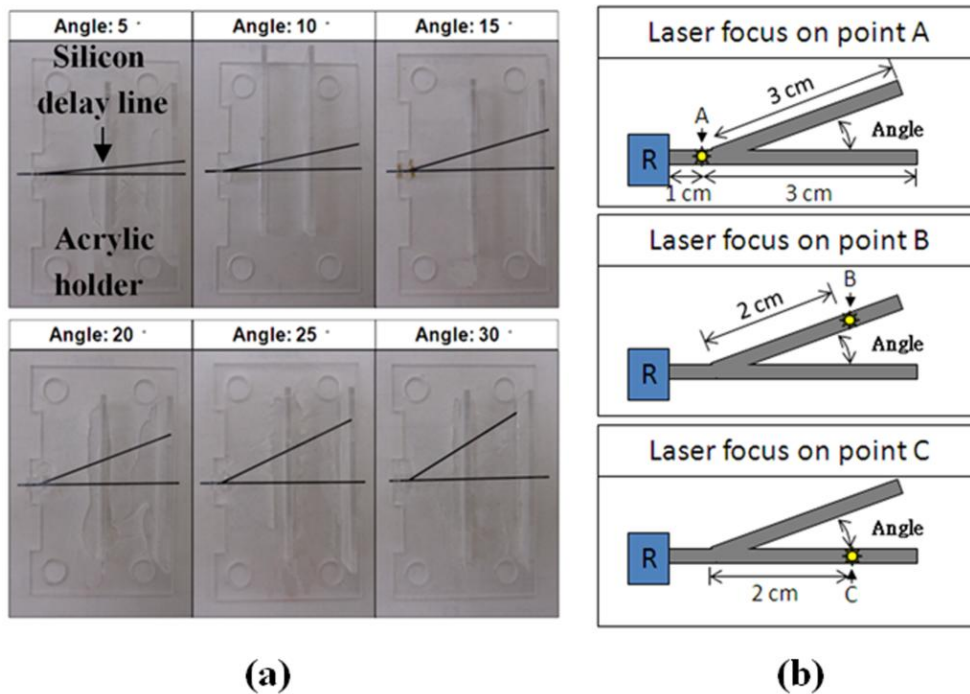
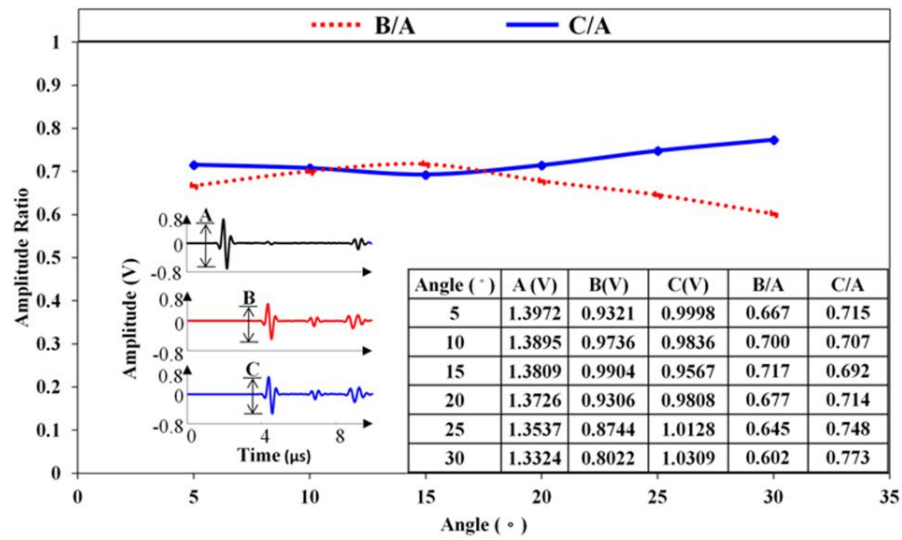
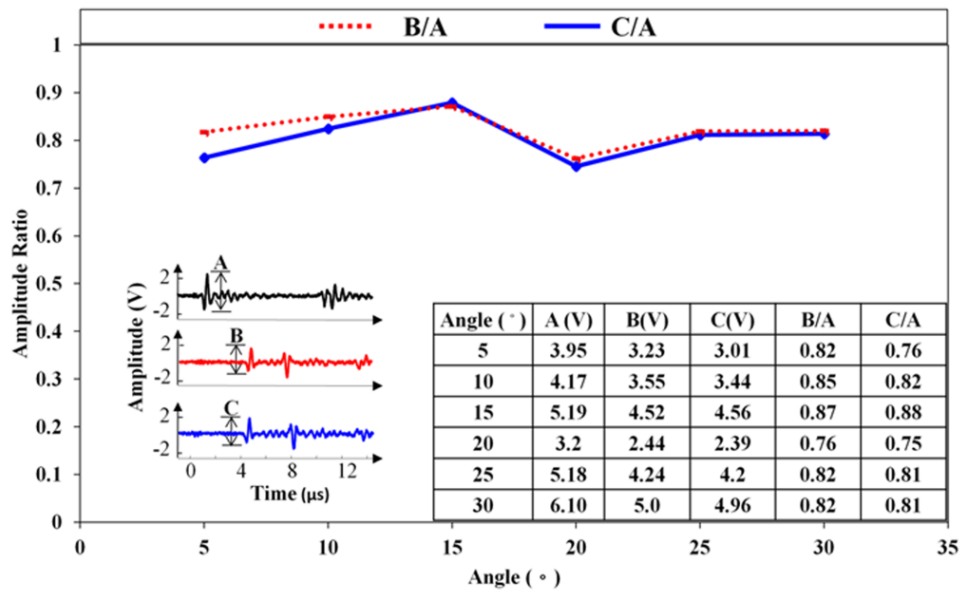


Figure 4.14 Y-junction structure measurement. (a) Samples; (b) Measurement setup: Receive signals from different focal points, A: without passing junction, B: passing junction through branch with an angle, C: passing junction through straight line.

As shown in figure 4.15, at a small cross angle, the insertion loss is not significantly affected by the change of the angle. Signals coming from the straight part or the branch do not have much difference. The average insertion loss of the Y-junction is around 20%, which is due to the wave leakage and reflection into the other branch.



(a)



(b)

Figure 4.15 Y-junction structure measurement. (a) Simulation results of angle versus amplitude ratio. Inset: Representative signal shapes from junction with 15 degrees; and (b) Experimental results of angle versus amplitude ratio. Inset: Representative signal shapes from junction with 15 degrees.

4.5.4 Comparison of signal shape from different structures

The typical acoustic pulse shape and spectrum of the first received signal are compared to investigate the structural effect on wave form in each structure (figure 4.16). All signals appear to have similar pulse shapes, and the pulse duration remains within 1 μs . The power spectrum shows that most signals are below 5 MHz, which matches well with the frequency response of the transducer.

Our experimental results show that the difference in structure of the delay line does not cause significant signal distortion, but only changes in amplitude. By carefully design the length and structure, acoustic signal can have a designated time delay with a distinguishable pulse shape. As a result, the straight, U-turn, and y-junction structures can be applied in the design for serial and parallel delay lines.

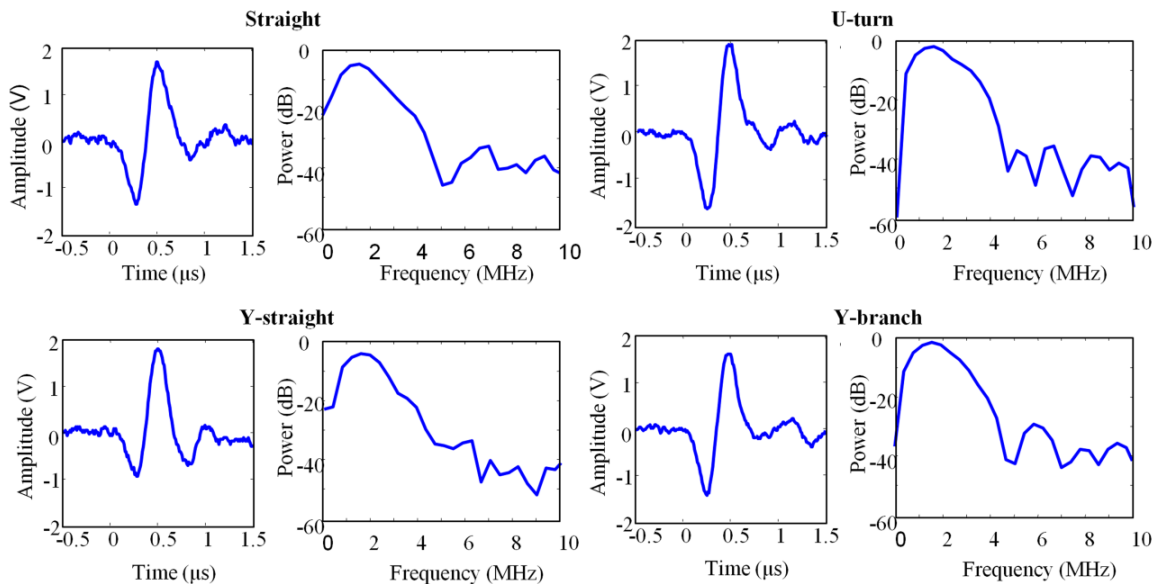


Figure 4.16 Pulse shape and spectrum of different structures.

4.6 Multi-channel serial and parallel delay lines

A 4-channel serial delay line and a 4-channel parallel delay line were designed, fabricated and tested. The serial delay line has four inputs and one output, which consists of straight lines, U-turns with 4 mm radius, and 30- degree Y-junctions (figure 4.17). The parallel delay line has four inputs and four outputs. Each channel consists of a multiple-turn spiral structure with a minimal radius of 2.5 mm (figure 4.18). The serial and parallel delay lines were tested using a two-port ultrasound measurement setup (figure 4.19). The delay lines were fixed on an acrylic holder with its inputs and outputs polished. A pulser-receiver unit was used to generate a driving voltage pulse for a 2.25 MHz transmitting transducer (V106, Olympus NDT, Waltham, MA, USA). The four delay line inputs received the ultrasound pulse at the same time from the transmitting transducer. The four pulses traveled different length in the delay line and arrived at the outputs at different time. The receiving transducer captured the signals from the outputs, which were amplified by pulser-receiver unit. The signals were averaged 128 times and displayed on the oscilloscope.

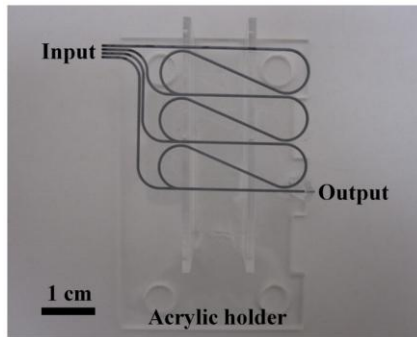


Figure 4.17 4-channel serial delay lines assembled on an acrylic holder.

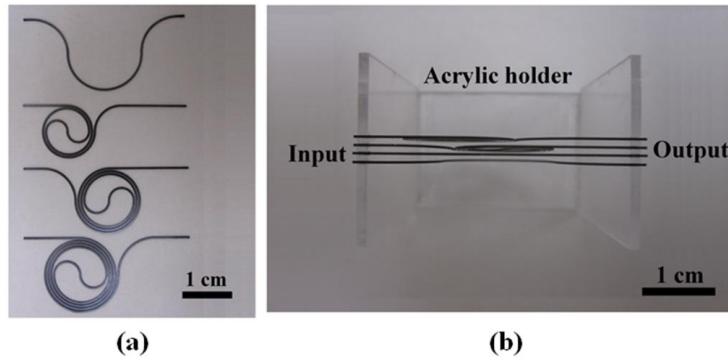


Figure 4.18 4-channel parallel delay lines. (a) Fabricated; and (b) Assembled on an acrylic holder.

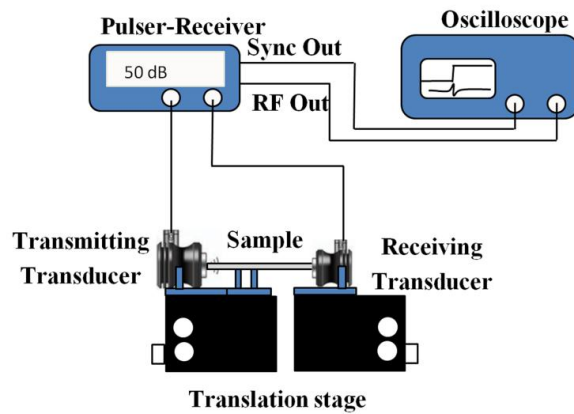


Figure 4.19 Two-port through-transmission setup.

Figure 4.20 shows the received signals from the serial and the parallel delay lines. Both delay line structures successfully achieved four time-delayed signals with approximately $7\ \mu\text{s}$ interval between adjacent channels. It is observed that the signal amplitude in both designs decreases from channel 1 to channel 4. Since the attenuation in silicon is negligible, the loss is due to the delay line structure. In the serial delay line structure, the loss is from both the U-turns and Y-junctions. While in the parallel delay line structure, the loss is from the curve structures. Because the signal in longer channel goes through more U-turns and Y-junctions, it has a higher total insertion loss resulting in a smaller signal. Despite of the loss, signals from the delay line structures remain clear and distinctive.

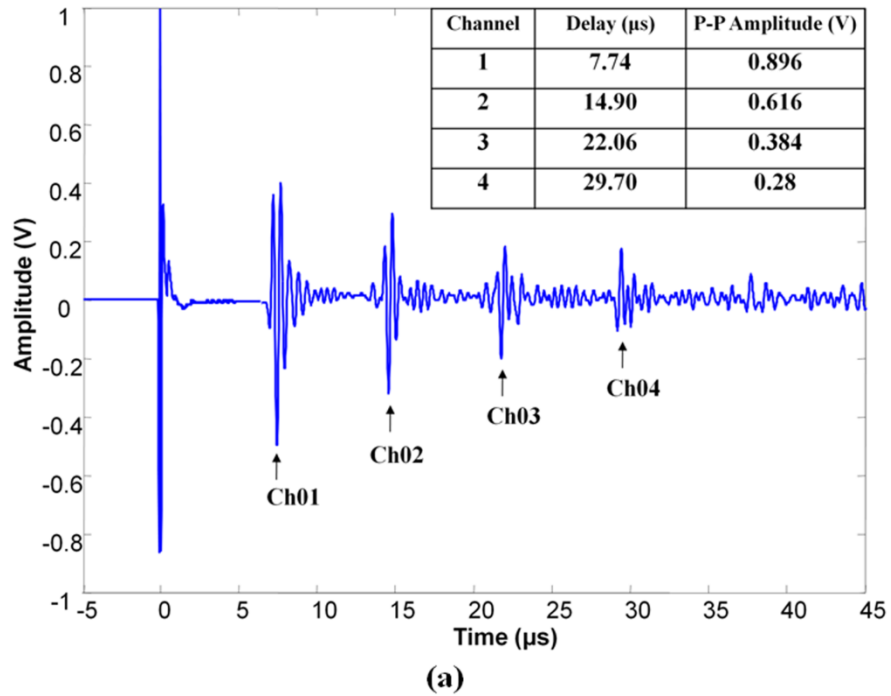


Figure 4.20 Time-delayed signals from. (a) 4-channel serial delay lines; and (b) 4-channel parallel delay lines.

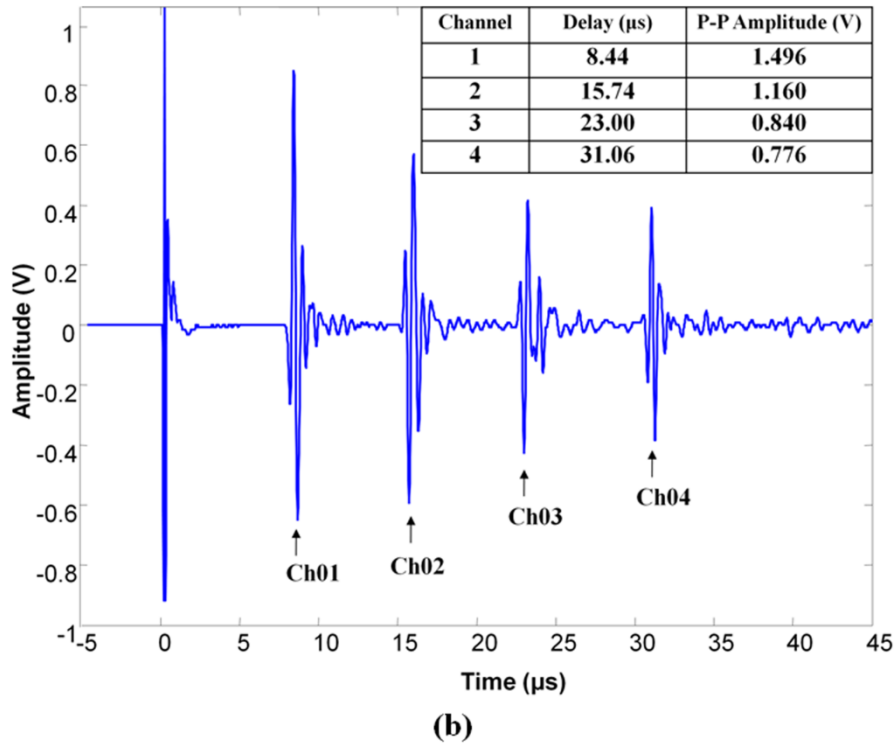


Figure 4.20 Continued.

4.7 Silicon parallel acoustic delay line probe

The feasibility of using serial or parallel delay line systems for ultrasound receiving system is proven in the previous experiment. To further capitalize its function and to reduce the size of the delay line system, a miniaturized 16-channel silicon parallel delay line probe was developed. The silicon fabrication followed the process described in 4.4.1. The etched individual channels are shown in figure 4.21 and the design parameters are listed in table 2.

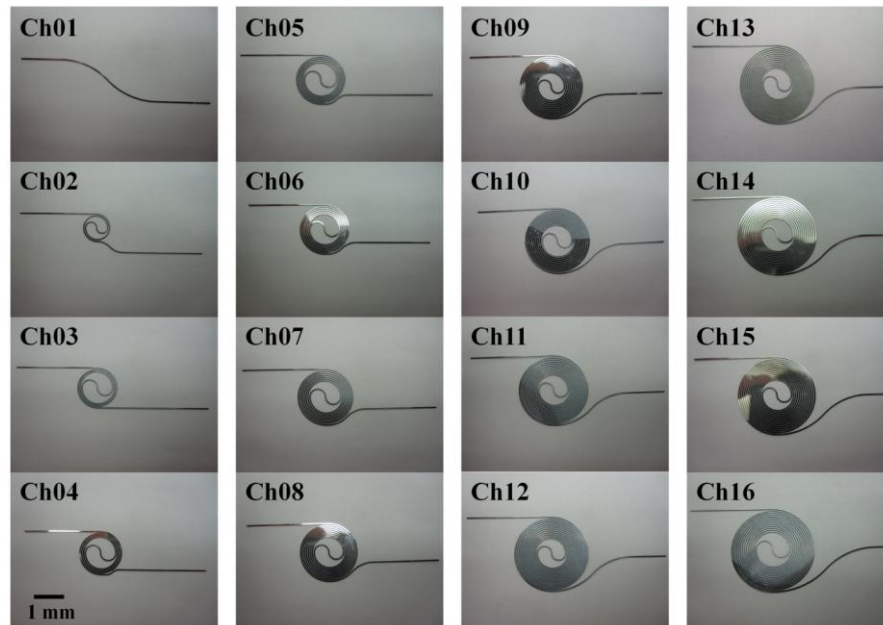


Figure 4.21 Etched silicon acoustic delay lines.

Table 2 Delay line design parameters.

Number of channels	Shortest delay (μs)	Longest delay (μs)	Incremental delay (μs)	Operation frequency (MHz)	Cross section (μm x μm)	Minimum radius of curvature (mm)
16	9.5	107	6.5	2.25	500 x 250	2

After the silicon delay lines fabrication, an acrylic probe structure was cut with laser machining and dicing saw. The acrylic probe was used to hold up the silicon delay lines to support and protect them. Prior to assembly, the two ends of silicon delay lines were carefully polished to create flat surface and enhance signal coupling. 16 silicon delay lines were carefully placed inside the acrylic probe structure and secured with superglue. Figure 4.22 shows the assembled silicon delay lines probe.

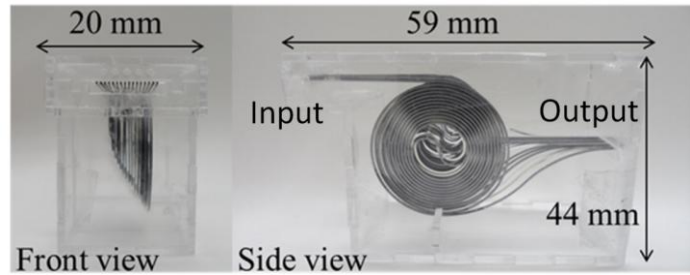


Figure 4.22 Assembled 16-channel silicon acoustic delay lines probe.

The silicon delay line probe was tested with the ultrasound through-transmission setup. Figure 4.23 shows the time-delayed ultrasound signals received by a single transducer. The difference in signal's strength is due to the non-uniform contacts between the silicon delay lines and the transducers. 16 distinctive ultrasound signals' peaks can be determined, which implies that the silicon delay line probe can effectively receive 16 ultrasound signals serially with only a single transducer.

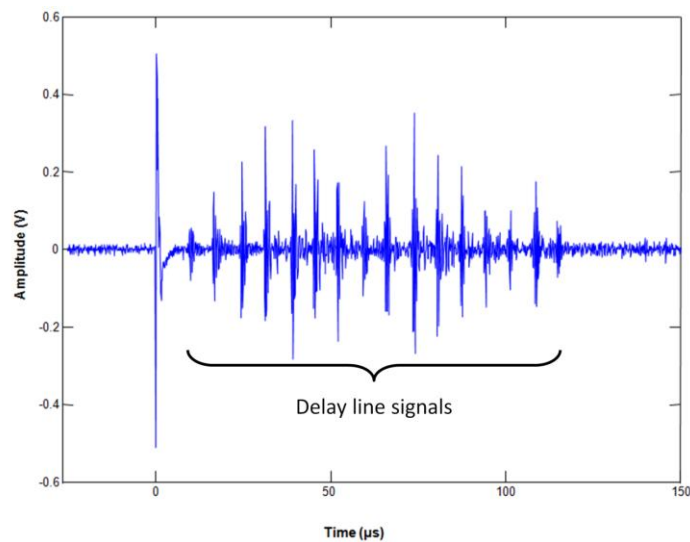


Figure 4.23 Ultrasound signals propagating in the 16-channel silicon acoustic delay line probe received by a single transducer.

The silicon acoustic delay line probe is more compact than the optical fiber delay line system. However, due to the brittleness of silicon, the mechanical stability of the silicon delay line probe is still problematic and difficult to maneuver. To improve the structure integrity, new designs and construction methods are required to further improve its usability.

4.8 Conclusion

In this work, we have successfully demonstrated the concept of delay line receiving systems using optical fiber delay lines and micromachined silicon acoustic delay lines. The acoustic velocity, attenuation, and propagation through bending and junction structures of silicon have been characterized. True acoustic time delay has been demonstrated using 4-channel serial and parallel delay lines and a 16-channel silicon delay line probe. Our experimental results show that with proper design and construction of the delay line structure, acoustic signals can be transmitted with minimal attenuation and distortion. With the addition of acoustic time delay, it is possible to receive multiple acoustic signals using one single-element transducer, followed by a single-channel of data acquisition electronics. We expect that the micromachined silicon delay lines can be applied to simplify the ultrasound receiver system architecture and reduce its costs, thereby helping to widen the applications of ultrasound imaging by enabling new modalities. Our future work will investigate the high-frequency transmission and switching of the silicon delay lines to achieve highly functional and integrated reconfigurable delay line systems.

5. MICROMACHINED ACOUSTIC MULTIPLEXER FOR ULTRASONIC AND PHOTOACOUSTIC IMAGING APPLICATIONS*

5.1 Introduction

5.1.1 *Electronics multiplexing in ultrasound receiving system*

In photoacoustic (PA) ultrasound receiving system, multiple channels of transducers and electronics are required [50]. As shown in figure 5.1, the 4-element transducer array receives ultrasound signals generated from an acoustic source and the received signals are processed by the data acquisition (DAQ) electronics simultaneously. The 4 to 1 multiplexer control the processed electrical signals and fed them serially into the computer for recording and image reconstruction. The acoustic waves were first transformed into electrical signals and processed by the data acquisition circuitry. To achieve fast speed and high resolution imaging, it is inevitable to use massive transducer array and DAQ electronics [51], [52]. As a result, the entire ultrasound imaging system becomes complex and costly. Electronic multiplexing has been used to reduce the number of DAQ channels by selecting and serially receiving PA signals from multiple transducers. However, the transducer array and its sophisticated electrical interface still remain.

*@ 2014 IEEE. Reprinted, with permission, from Cheng-Chung Chang, Young Cho, and Jun Zou, "A micromachined acoustic multiplexer for ultrasound and photoacoustic imaging applications," IEEE Journal of Microelectromechanical Systems, 23(3), pp. 514-516, 2014.

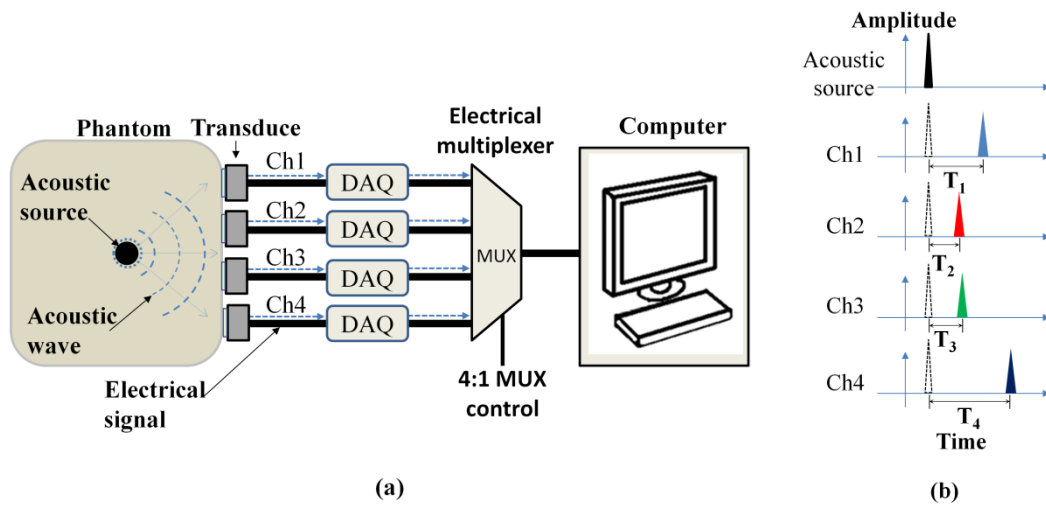


Figure 5.1 Ultrasound transducer array receiving system. (a) Transducer array and electronics setup; (b) Ultrasound signals received by the transducer array. T_1 , T_2 , T_3 , T_4 are the acoustic signal traveling time inside the phantom.

5.1.2 Acoustic multiplexing in ultrasound receiving system

The multiplexing concept has been widely used in switching electrical signals [62]. However, this concept has never been successfully applied in multiplexing acoustic signal. Previously, researchers have designed an acoustic multiplexer using wires and springs, but it can only selectively transfer acoustic wave in particular wavelength and no actual device was fabricated [63]. Others investigated on frequency multiplexing of surface acoustic wave, while no bulk acoustic wave device has been developed [64].

To address the issue of electronic multiplexing in ultrasound receiving system, a novel acoustic multiplexer concept is introduced. Unlike the electronic multiplexing method that go through the sequence of transformation (acoustic to electronics) then processing steps, the acoustic multiplexing method directly processes the acoustic signals first then transform them into electronic signals. As shown in figure 5.2(a), an

acoustic multiplexer is used to replace the transducer array. Upon excitation, an acoustic source generates acoustic waves, which are detected by the input terminals of the acoustic multiplexer (figure 5.2(b)). The acoustic multiplexer selects one acoustic signal from multiple input channels to reach the output terminal, where a single transducer and DAQ are connected to receive and process the acoustic signal. The excitation-selection-receiving cycles are repeated several times until all input channels have been selected sequentially (figure 5.2(c)). Signals from all channels are received serially by the single transducer and can be used for image reconstruction (figure 5.2(d)). The acoustic multiplexer converts parallel signals from multiple channels into serial signals in a single channel and thereby effectively reduces the transducer and electronics being used. Therefore, both the number of the transducer elements and DAQ channels could be reduced.

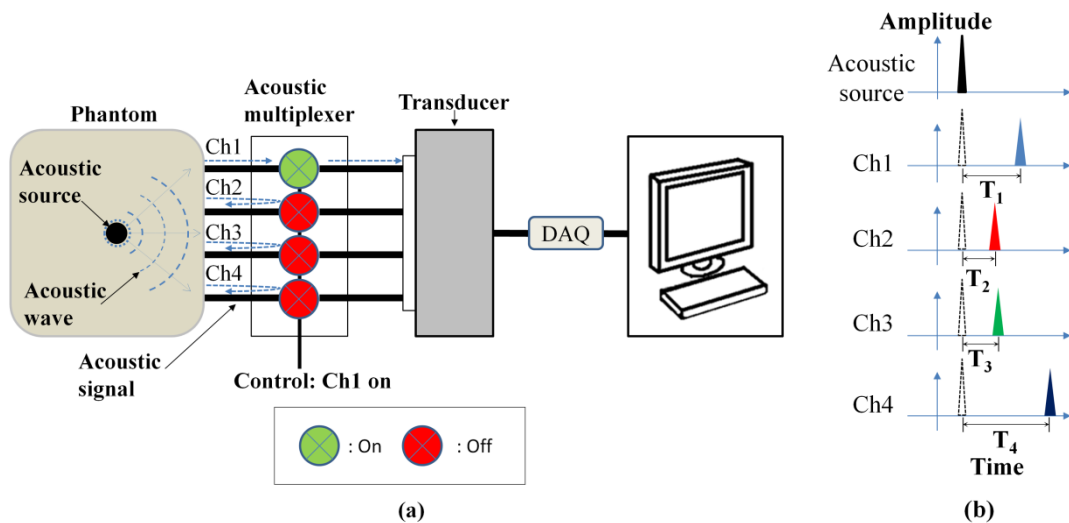
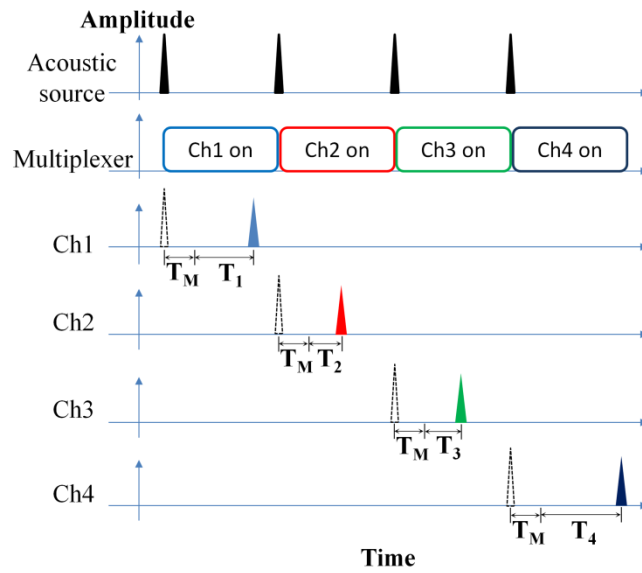
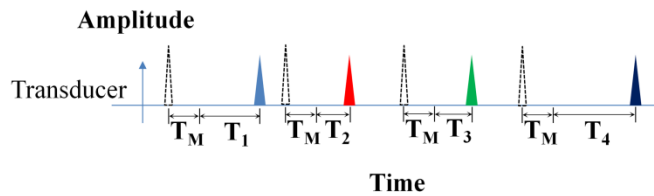


Figure 5.2 Acoustic multiplexer receiving system. (a) System setup; (b) Acoustic signals received by the multiplexer input; (c) Acoustic signals after multiplexing; (d) Ultrasound signals received by the single transducer. TM is the acoustic signal traveling time inside the multiplexer.



(c)



(d)

Figure 5.2 Continued.

With advanced micromachining technologies, all the essential components of the acoustic multiplexer can be fabricated or integrated with MEMS technologies simultaneously in one step without intensive assembly or packaging. As a result, the micromachined acoustic multiplexer could be a more economical and simpler approach for ultrasound receiving system. In this chapter, we report for the first time, a microfluidic silicon-based acoustic multiplexer which is capable of selecting bulk acoustic wave signal. It utilizes the acoustic properties of single-crystalline silicon and mercury, and the precision fabrication of the micromachining process. By using the

fabricated device, the acoustic multiplexing has been successfully demonstrated in the photoacoustic imaging receiver system.

5.2 Design of the acoustic multiplexer

Figure 5.3 shows the schematic of the micromachined acoustic multiplexer. It consists of multiple pairs of acoustic waveguides, each of which forms an acoustic channel for ultrasound signal transmission. A microfluidic channel lies between each pair of the acoustic waveguides and serves as an on/off switch for the acoustic waveguides. The acoustic waveguides and the microfluidic channel were made of single-crystalline silicon.

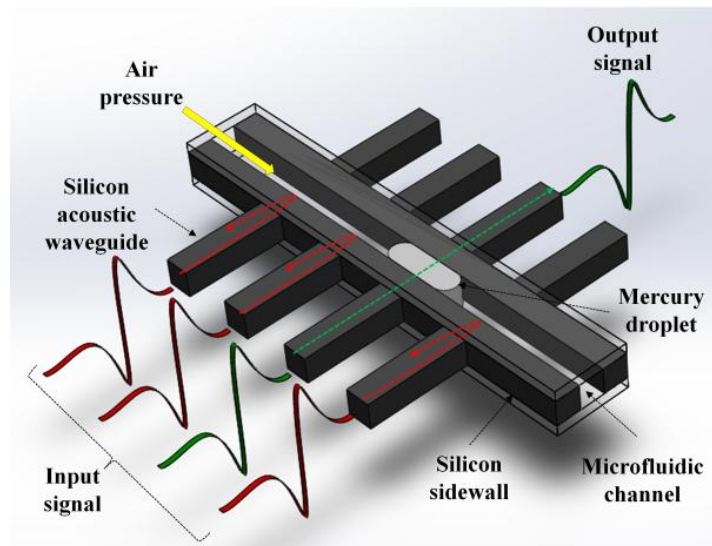


Figure 5.3 Schematic design of the acoustic multiplexer. Acoustic signal can be coupled to the output end through mercury droplet. The location of the mercury droplet is controlled by external air pressure.

Silicon was considered as the structural material for three reasons. First, the acoustic attenuation of silicon is extremely low in the MHz range ($\sim 10^{-4}$ dB/mm·MHz² @ 10 MHz) [59]. Second, silicon is mechanically strong with good thermal stability. Third, it has been widely used as structural material and is suitable for advanced microfabrication and micromachining. To transmit single longitudinal mode ultrasound signal, the rectangular-shaped silicon acoustic waveguide should have a cross section dimension satisfies $(df/V_0) \ll 1$, where d is the width or thickness of the acoustic waveguide (whichever is smaller), f is the frequency of the signal, and V_0 is the acoustic velocity of silicon [58]. To transmit 2.25 MHz center frequency signals in a silicon waveguide with acoustic velocity of 8430 m/s [59], the dimension should be much smaller than 3.7 mm. In this session, the silicon acoustic waveguides have 500 μ m in width and 300 μ m in thickness. To obtain high spatial resolution, the input ends of the silicon waveguides should be closely placed. This is achieved by using bending waveguide structure to merge the input ends. The bending radius of the waveguide should be larger than 2 mm to ensure good signal transmission for silicon waveguide in this dimension [65]. In this work, the minimum bending radius used is around 20 mm and the pitch for the waveguide ends is 500 μ m. The resulting input/output terminals have a width of 7.5 mm. The close arrangement of the output ends also enables smaller and cheaper transducer to be used to receive the ultrasound signals. The acoustic multiplexing is achieved by using a liquid-coupling acoustic switch, which is made of a microfluidic channel and a mercury droplet. Mercury is chosen for its mechanical and acoustical properties. The high surface tension of mercury enables the mercury droplet to

maintain its shape without spreading in the microfluidic channel. The size of the mercury inside the microfluidic channel can be designed by adjusting its volume. The width of the mercury droplet should be close to the acoustic waveguide to enhance coupling. The location of the mercury droplet is controlled by external pneumatic source. The acoustic impedance of mercury is very close to silicon [66], which allows efficient acoustic coupling between these two materials. When the mercury droplet is placed at the gap between two silicon acoustic waveguides, the incoming ultrasound signal from one silicon waveguide (input) can be effectively coupled to the silicon waveguide at the other end (output). The waveguides pair forms an “ON” state acoustic channel. Ultrasound signals in other acoustic waveguides are blocked due to the large acoustic impedance mismatch of air and silicon, thus act as “OFF” state acoustic channels.

The switching principle was simulated using ultrasound simulation software (Wave2000, Cyberlogic Inc., New York, USA). Two silicon delay lines were placed in line between a 2.25 MHz input transmitting transducer and a 2.25 MHz output receiving transducer. The gap between two silicon delay lines was filled with air or mercury to simulate the "OFF" state and "ON" state acoustic channels. Figure 5.4 shows the simulation results of the received signals at the output end from the “ON” state and “OFF” state acoustic channels. From the simulation results, the mercury-coupling “ON” state effectively transmitted the ultrasound signal while the air-coupling “OFF” state rejected the ultrasound signal.

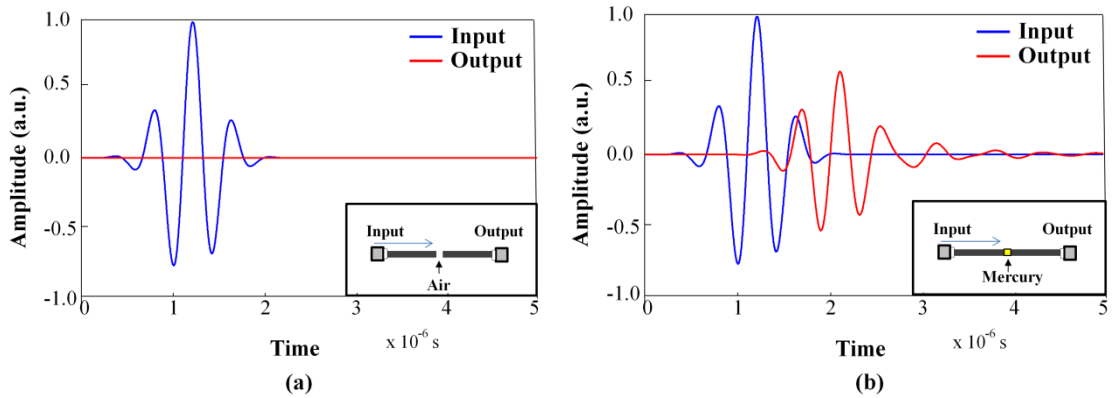


Figure 5.4 Simulation results of the "ON" state and "OFF" state acoustic channels. (a) Air-coupling "OFF" state; (b) Mercury-coupling "ON" state. Inset: Simulation setup. The air and mercury gaps are 500 μm in width.

5.3 Fabrication of the micromachined acoustic multiplexer

The silicon acoustic delay lines and multiplexer structure (figure 5.5) was etched out from a 300 μm -thick double-side-polished silicon wafer using cryogenic deep reactive ion etching. The width of the silicon delay lines is 500 μm . The tips of the silicon delay lines and the sidewalls of the microfluidic channel were polished to create flat contact surface to ensure good acoustic coupling. The pitch of the distal ends of the silicon acoustic delay lines is set to be 1 mm to maintain good lateral imaging resolution, and that of the proximal ends is set to be 2 mm to provide good acoustic isolation between two adjacent delay lines. The minimum bending radius of the acoustic delay lines is 23 mm, which is much larger than the acoustic wavelength to minimize the signal distortion caused by mode conversion [67].

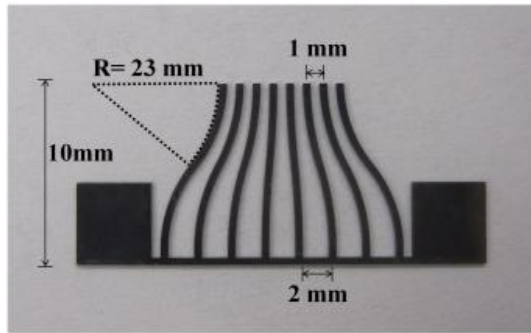
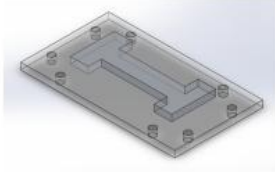


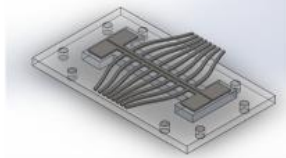
Figure 5.5 Fabricated silicon acoustic multiplexer structure (one side).

The multiplexer assembly process is shown in figure 5.6. First, PDMS sealing pads were directly moulded on a laser-micromachined acrylic sheet. PDMS has high acoustic attenuation and large acoustic impedance mismatch to silicon and mercury, which helps to reduce signal cross talk between adjacent channels. Second, the silicon structures were attached on the PDMS sealing pad and two polyimide micro tubings with a diameter of 300 μm were placed at the two ends of the microfluidic channels. One of the polyimide microtubing was connected to a syringe pump for pneumatically driving of mercury droplet inside the microfluidic channel, while the other one was used to release the gas pressure. To form a closed microfluidic channel, another PDMS sealing pad with acrylic sheet was stacked on top of the silicon-PDMS-acrylic structure. Screws were used to fix and stabilize the structure. After assembly, a mercury droplet of 100 nL was driven into the microfluidic channel to form a micro slug (1 mm \times 0.3 mm \times 0.3 mm) (Fig. 4(d)). The overall dimension of the assembled acoustic multiplexer is 35 mm \times 22 mm \times 6 mm (figure 5.7).

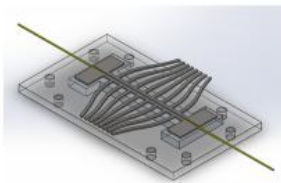
(1) Mould PDMS on acrylic



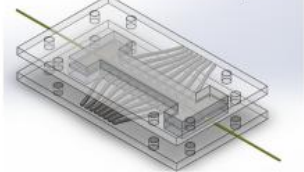
(2) Attach silicon structure



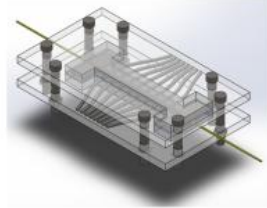
(3) Insert polyimide microtubing



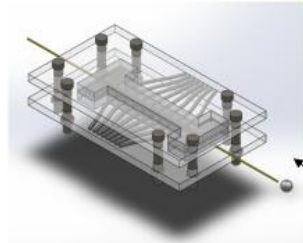
(4) Stack with PDMS-acrylic cover



(5) Fix with screws



(6) Drive mercury droplet into microfluidic channel



(7) The complete device

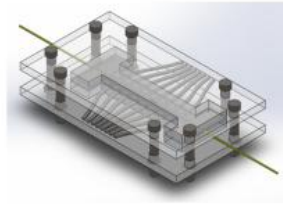


Figure 5.6 Acoustic multiplexer assembly process.

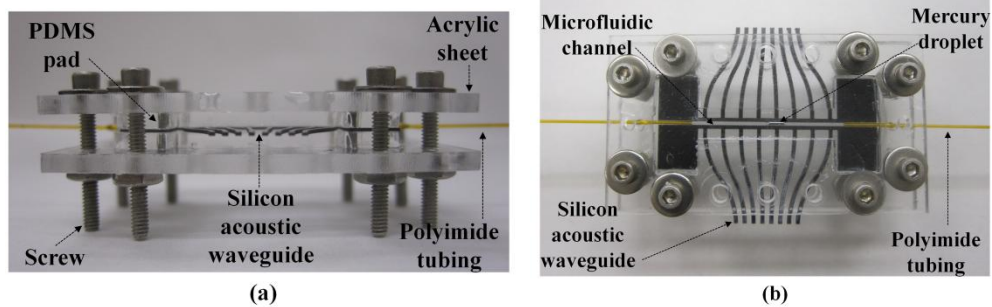


Figure 5.7 Assembled acoustic multiplexer. (a) Side view; (b) Top view.

5.4 Characterization of the micromachined acoustic multiplexer

The multiplexer was tested with the ultrasound transmission setup (figure 5.8). A pulser-receiver unit (5072-PR, Olympus NDT, Waltham, MA, USA) was used to generate a driving voltage pulse for a 2.25 MHz transmitting transducer (V105, Olympus NDT, Waltham, MA, USA). The transmitting transducer was in contact with the input terminal of the acoustic multiplexer and mineral oil was applied at the interface to improve the coupling efficiency between the transducer and silicon. The transmitting transducer sent out ultrasound signals which travel along the acoustic waveguides and reach the silicon sidewall. When the acoustic channel is on (i.e. coupling through mercury), the ultrasound signal is transmitted from the input acoustic waveguide to the output acoustic waveguide at the other end. When the acoustic channel is off (i.e. coupling through air), the ultrasound signal is blocked. A 2.25 MHz receiving transducer (V106, Olympus NDT, Waltham, MA, USA) was used to capture the ultrasound signal. The received signal was amplified by the pulser-receiver unit and displayed on the oscilloscope.

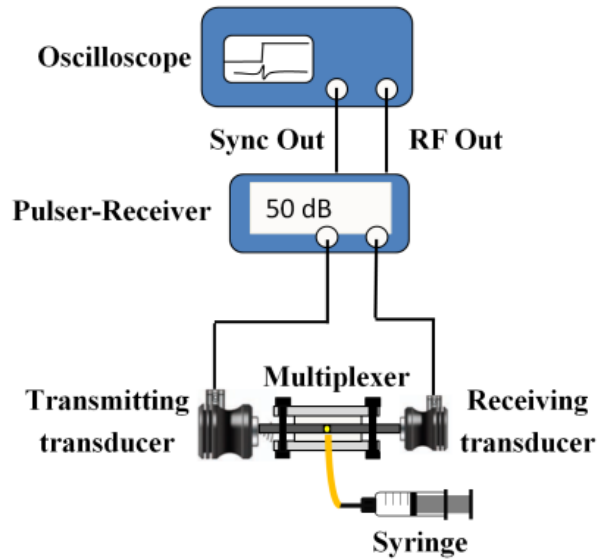


Figure 5.8 Ultrasound transmission experiment setup.

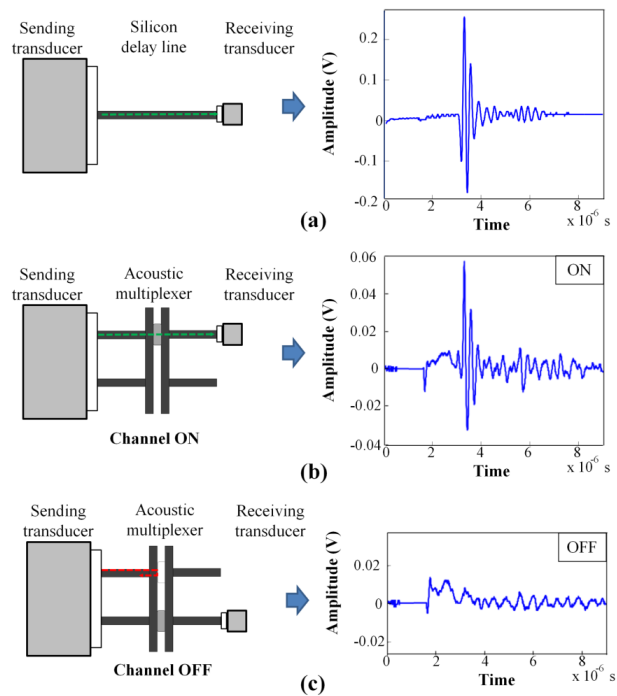


Figure 5.9 Acoustic ON/OFF characterization. (a) Reference signal from silicon delay line; (b) "ON" setup and the transmitted signal; (c) "OFF" setup and the transmitted signal.

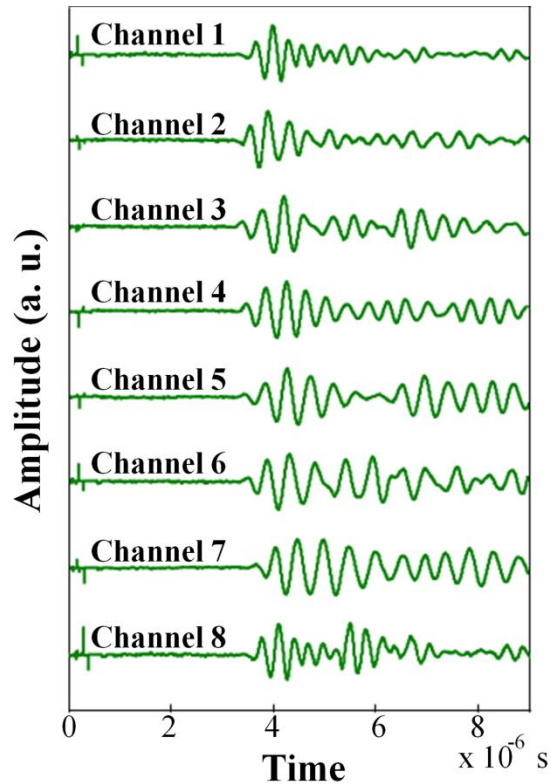


Figure 5.10 Ultrasound signals from each channel received by the transducer.

5.5 Application: Photoacoustic imaging with acoustic multiplexer

5.5.1 Photoacoustic effect

Photoacoustic (PA) imaging is an imaging technique based on the photoacoustic effect [68]. Photoacoustic effect describes an ultrasound generation phenomenon caused by periodic temperature fluctuations. When light hits on a sample, the sample will absorb the optical energy (figure 5.11(a)). Part of the ground state molecular in the sample will be excited into higher energy levels. These excited molecules will subsequently relax through different mechanism. Most of the absorbed energy will transform into heat while others will go through other process such as luminescence,

photochemical reaction, photoelectricity reaction, or into momentum resulting collision. These energy transform mechanisms will eventually turn into heat. The heating process raises the temperature of the sample, and the temperature increment will result in thermal expansion of the sample. Due to the temperature difference between the sample and the surrounding medium, heat will flow from the higher temperature sample into lower temperature surroundings. This heat flow changes the temperature of the surrounding medium and the surrounding medium also goes through thermal expansion. By periodically heating the sample, the sample and the surrounding medium will have temperature fluctuations. This fluctuation will cause the temperature changing medium, sample or the surrounding, to expand and shrink periodically. This volume change thus creates a pressure wave, which can be detected as an acoustic signal. The acoustic signal generation process is shown in figure 5.11(b).

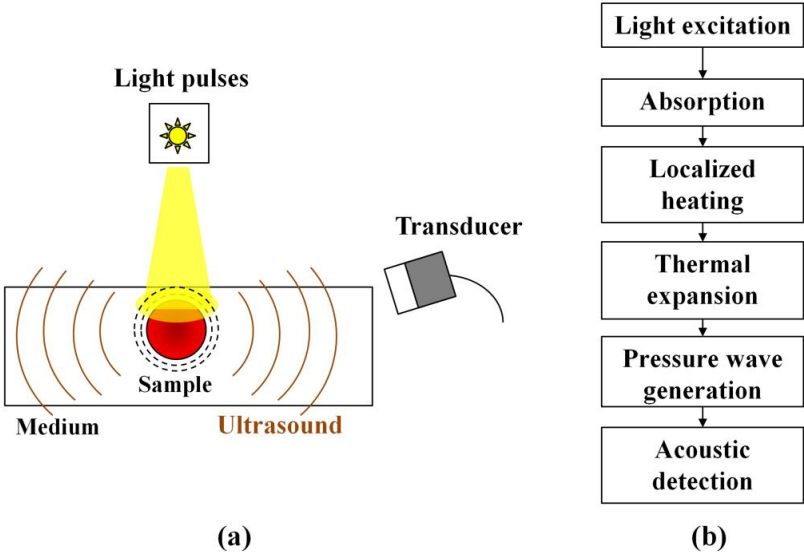


Figure 5.11 Physical process of photoacoustic effect.

5.5.2 *Photoacoustic imaging techniques*

In order to form a photoacoustic image, a single-element ultrasound receiving transducer is scanned around the medium; alternatively, a multi-element ultrasound array can be used to receive signals at different locations. The PA images are reconstructed based on the time-of-flight (i.e. arrival time) of the ultrasonic wave. The imaging contrast is determined by the optical absorption of the sample and the ultrasound receiving frequency. Combining these two parameters, the photoacoustic imaging is not limited by the optical scattering or speckle artifacts and low contrast inherited from ultrasound imaging. Therefore, photoacoustic imaging provides high spatial resolution and is suitable for deep tissue imaging. Based on the imaging application, the spatial resolution and imaging depth can be tuned by selecting proper ultrasound detection frequency.

There are two types of photoacoustic imaging systems. The first type is photoacoustic tomography (PAT), which reconstructs images based ultrasound signals received from multiple locations [69]. The second type is photoacoustic microscopy (PAM), which utilizes raster scan over a subject to collect point-by-point photoacoustic signals. In PAT, a single un-focused transducer or an array of transducers can be used to receive acoustic signal, while the array method can provide faster imaging speed. On the other hand, in PAM, a focused transducer is used in the raster scan. To demonstrate the capability of micromachined acoustic multiplexer in processing multiple acoustic signals, the acoustic multiplexer was applied in PAT system by replacing the array-type transducers.

5.5.3 *Experiment setup*

Figure 5.12 shows the setup of the photoacoustic experiment. A Q-switched Nd:YAG pulsed-laser source (MP-1200mj, Guangzhou Miu Sing Co., Ltd, China) with 532 nm wavelength and 8 ns pulse width was used to deliver light. The laser was controlled by an external trigger to allow single pulse excitation. A photodiode (DET36A, Thorlabs, Newton, NJ, USA) was used to determine the trigger time. The laser light was attenuated with a neutral density filter (NE510B, Thorlabs, Newton, NJ, USA) and focused by a lens on a 5 mm x 5 mm area. The incident laser pulse energy density was 20 mJ/cm². When laser illuminates on an optical absorptive material, the material absorbs the light energy and goes through sudden thermal expansion[70]. The thermal expansion generates acoustic waves that radiates away from the excitation point. The acoustic waves were captured by the acoustic multiplexer, which processes and selects ultrasound signal from one of the 8 channels. The ultrasound signal from the selected acoustic channel was captured by the 2.25 MHz center frequency receiving transducer (V105, Olympus NDT, Waltham, MA, USA) and amplified by a pulser-receiver unit. To improve coupling efficiency, mineral oil was applied at the multiplexer-transducer interface. The laser trigger signal from the photodiode and amplified ultrasound signals were displayed on the oscilloscope. The laser excitations, multiplexer selection, transducer receiving cycles were repeated 8 times to collect signals from all 8 channels for image reconstruction.

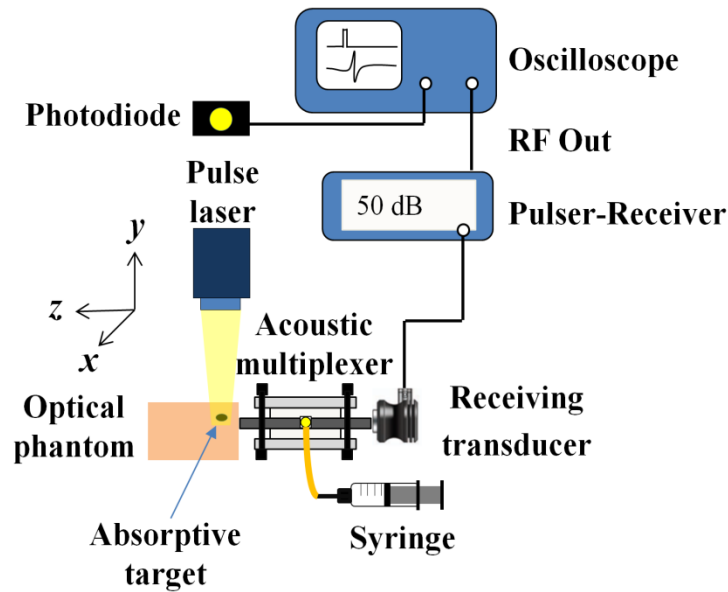


Figure 5.12 Photoacoustic imaging setup.

To demonstrate its application in acoustic imaging, the fabricated 8-channel acoustic multiplexer was used to conduct photoacoustic tomography on an optically absorptive target buried inside an optically scattering phantom (figure 5.13). The optically absorptive target was a silicon piece with a radius of 0.75 mm in the x-z plane and a thickness of 0.3 mm in the y direction. It was located at 4.5 mm away from the surface of the optical phantom (along the z direction). The phantom was made of 3% wt. agar solution. Agar phantom has optical and acoustical properties similar to biological tissue, therefore it has been widely used in photoacoustic imaging [71]. The agar phantom has a dimension of 100 x 30 x 70 mm³ along x, y, and z axes, respectively.

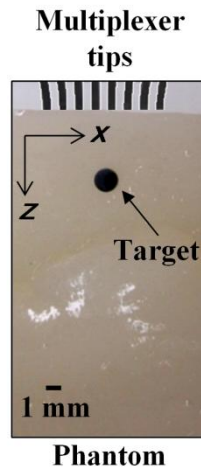


Figure 5.13 Zoom in view of the imaging target inside the optical phantom.

5.5.4 Imaging result

Figure 5.14(a) shows the received photoacoustic signals from the 8 acoustic channels of the acoustic multiplexer. Figure 5.14(b) shows the reconstructed photoacoustic image in Matlab[®] (MathWorks, Natick, MA, USA). The amplitude and the arrival time of the photoacoustic signals were normalized and calibrated, respectively. The envelope of the photoacoustic signals was calculated with Hilbert transform and the photoacoustic image was reconstructed using synthetic aperture focusing technique (SAFT) [72]. The imaging contrast, defined as the signal ratio between the imaging target and the background, is around 3. In the photoacoustic image, the location of the reconstructed object matches well with that of the absorptive target in the optical phantom.

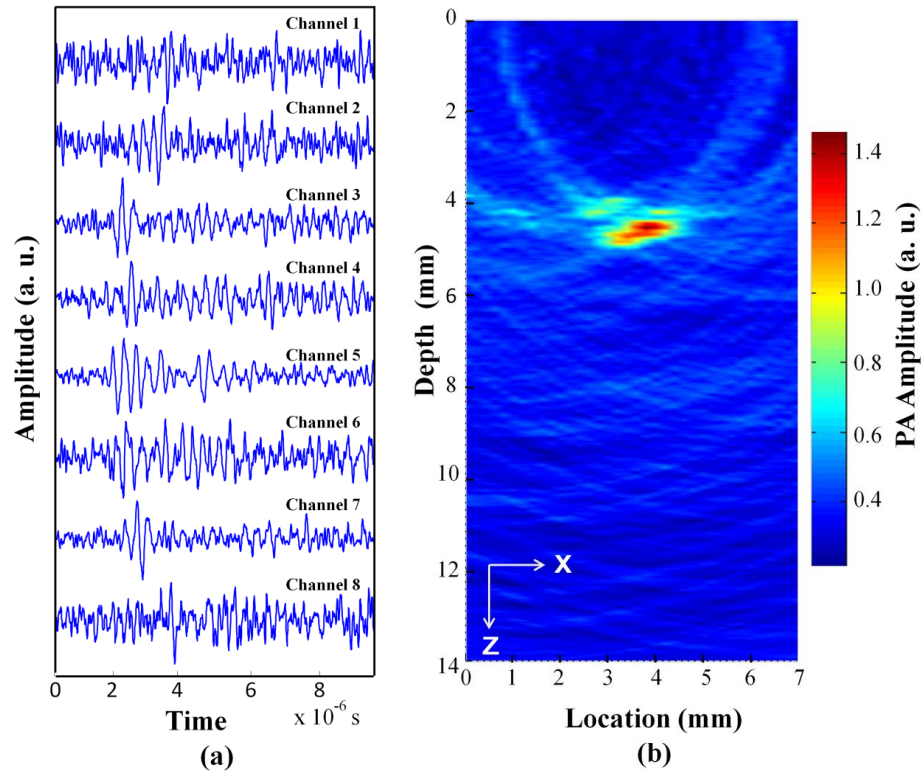


Figure 5.14 Photoacoustic imaging results. (a) Photoacoustic signals received from each channel; (b) Reconstructed photoacoustic image.

5.6 Conclusions

In this work, we have successfully demonstrated a micromachined microfluidic acoustic multiplexer. The acoustic multiplexer is able to select ultrasound signal out from multiple acoustic channels. An 8-channel acoustic multiplexer was constructed and its functionality for ultrasound applications was demonstrated by conducting cross-section photoacoustic imaging of an optically absorptive target. By using the 8-channel acoustic multiplexer, only one receiving transducer was needed to process all the channels. Therefore, the acoustic multiplexer could be a potential method to create cheap and simple ultrasound receiving systems. In the future, we will investigate using on-chip

droplet driving mechanism to improve the stability and switching speed of the acoustic multiplexer. Table 3 compares the possible on-chip driving mechanisms for future investigation.

Table 3 On-chip driving mechanism.

Mechanism	Method	Advantage	Disadvantage
Pneumatic (this work)	<ul style="list-style-type: none"> • Pressure gradient [73] 	<ul style="list-style-type: none"> • Simple 	<ul style="list-style-type: none"> • Require external pressure source • Slow speed
Thermal	<ul style="list-style-type: none"> • Thermal capillary effect [74] • Bubble formation [75] 	<ul style="list-style-type: none"> • No moving parts 	<ul style="list-style-type: none"> • High power consumption • Slow speed
Acoustical	<ul style="list-style-type: none"> • Surface acoustic wave pumping [76] 	<ul style="list-style-type: none"> • Fast speed 	<ul style="list-style-type: none"> • Single direction • High driving voltages
Optical	<ul style="list-style-type: none"> • Photochemical [77] • Opto-electrowetting [78] • Light-induced thermal capillary effect [77] 	<ul style="list-style-type: none"> • No moving parts • Tunable • Biocompatible 	<ul style="list-style-type: none"> • Substrate heating • Slow speed
Electrical	<ul style="list-style-type: none"> • Dielectrophoretics [79] • Electrocapillary [80] • Electrowetting [81], [82] 	<ul style="list-style-type: none"> • Site specific control • No heating • No moving parts • Low power consumption • Fast speed 	<ul style="list-style-type: none"> • Electrolysis • May require high voltages • Polarization of substrate
Structural	<ul style="list-style-type: none"> • Electrochemical with surfactant [83] • Asymmetric surface [84] 	<ul style="list-style-type: none"> • No moving parts • Low power consumption 	<ul style="list-style-type: none"> • Material compatibility • Slow speed
Magnetical	<ul style="list-style-type: none"> • Magnetohydrodynamics [85] 	<ul style="list-style-type: none"> • Low voltage • Suitable for conductive liquid • No moving parts • Fast speed 	<ul style="list-style-type: none"> • Electrolysis • High power consumption • Limited dimensions (conduit size > 100 μm)

6. CONCLUSIONS

In this study, the usefulness of the micromachined optical and acoustic waveguides systems was demonstrated with sensing and imaging applications. The micromachined optical waveguide systems have compact dimensions and side-viewing capability, which enable precise light delivery and receiving inside small cavities. The development of the optical sensor probe required multiple steps including optical path simulation, microfabrication, probe assembly, and experimental testing and validation.

Two different kinds of micromachined optical waveguide systems along with their sensing applications were presented. 1) Micromachined OIDRS optical sensor probe for pancreatic cancer identification; 2) Micromachined VNIR-DRS optical sensor probe for soil characterization. The optical sensor probe together with the OIDRS system successfully determined the tumor margin on a human pancreatic specimen, while the optical sensor probe combined with VNIR-DRS system provided constitution information of the soil.

The micromachined acoustic waveguide systems utilized single crystalline silicon for direct acoustic signal processing. The micromachined silicon structures replace complex transducer array and multi-channel data acquisition electronics, thus allowing the use of only one ultrasound transducer and one data acquisition channel for acoustic imaging. This setup simplifies the imaging system and can be directly fabricated and integrated with acoustic circuitry in one step, thereby significantly reduced the labor or cost for packaging. The development of the acoustic waveguide system includes material acoustic properties characterization, proof of concept

experiment, ultrasound simulation, structure fabrication and assembly, and testing of the imaging system.

Two micromachined acoustic waveguide systems were realized and implemented in ultrasound and photoacoustic applications. 1) Micromachined acoustic delay line system for ultrasound signal processing; 2) Micromachined acoustic multiplexer for photoacoustic imaging. The acoustic delay line system passively controls ultrasound signal by introducing proper time delay in the acoustic channels, thereby enables the conversion of parallel signals into serial signals. The acoustic multiplexer actively selects photoacoustic signals from multiple channels and processed the signals one after another. Both systems utilized the acoustic properties of single crystalline silicon and provides new methods for processing multiple channels' signals with a single transducer and electronics.

Through the waveguide system designs discussed in this thesis, the optical waveguide systems and acoustic waveguide systems combined with micromachining technology have improved the use of optical sensor probes and inspired new acoustic imaging systems. By configure waveguide dimensions and wave transmission directions, the waveguide systems can be tailored for various applications.

REFERENCES

- [1] L. Wang and S. L. Jacques, "Use of a laser beam with an oblique angle of incidence to measure the reduced scattering coefficient of a turbid medium," *Appl. Opt.*, vol. 34, no. 13, pp. 2362–2366, 1995.
- [2] S.-P. Lin, L. Wang, S. L. Jacques, and F. K. Tittel, "Measurement of tissue optical properties by the use of oblique-incidence optical fiber reflectometry," *Appl. Opt.*, vol. 36, no. 1, pp. 136–143, 1997.
- [3] B. W. Farrell, Thomas J., Michael S. Patterson, "A diffusion theory model of spatially resolved, steady-state diffuse reflectance for the noninvasive determination of tissue optical properties in vivo," *Med. Phys.*, vol. 19, p. 879, Jan. 1992.
- [4] L. Wang, S. L. Jacques, and L. Zheng, "MCML—Monte Carlo modeling of light transport in multi-layered tissues," *Comput. Methods Programs Biomed.*, vol. 47, no. 2, pp. 131–146, 1995.
- [5] R. M. Stone, H. B., Brown, J. M., Phillips, T. L., Sutherland, "Oxygen in human tumors: correlations between methods of measurement and response to therapy," *Radiat. Res.*, vol. 136, pp. 422–434, 1993.
- [6] S. Thomsen and D. Tatman, "Physiological and pathological factors of human breast disease that can influence optical diagnosis," *Ann. N. Y. Acad. Sci.*, vol. 838, no. 1, pp. 171–193, 1998.
- [7] L. T. Perelman, V. Backman, M. Wallace, G. Zonios, R. Manoharan, A. Nusrat, S. Shields, M. Seiler, C. Lima, T. Hamano, I. Itzkan, J. Van Dam, J. M. Crawford, and M. S. Feld, "Observation of periodic fine structure in reflectance from biological tissue: a new technique for measuring nuclear size distribution," *Phys. Rev. Lett.*, vol. 80, no. 3, pp. 627–630, 1998.
- [8] "Microchem Corp." [Online]. Available: www.microchem.com. Accessed: January 18, 2009.
- [9] "American cancer society." [Online]. Available: <http://www.cancer.org>. Accessed: March 31, 2010.
- [10] P. R. Bargo, S. A. Prahl, T. T. Goodell, R. A. Slevin, S. L. Jacques, G. Koval, and G. Blair, "In vivo determination of optical properties of normal and tumor tissue with white light reflectance and an empirical light transport model during endoscopy," *J. Biomed. Opt.*, vol. 10, no. 3, 34018, 2005.

- [11] T. C. Zhu, J. C. Finlay, and S. M. Hahn, "Determination of the distribution of light, optical properties, drug concentration, and tissue oxygenation in-vivo in human prostate during motexafin lutetium-mediated photodynamic therapy," *J. Photochem. Photobiol. B Biol.*, vol. 79, no. 3, pp. 231–241, 2005.
- [12] S. Brand, J. M. Poneros, B. E. Bouma, G. J. Tearney, C. C. Compton, and N. S. Nishioka, "Optical coherence tomography in the gastrointestinal tract," *Endoscopy*, vol. 32, no. 10, pp. 796–803, 2000.
- [13] H. Messmann, R. Knüchel, W. Bäumlner, A. Holstege, and J. Schölmerich, "Endoscopic fluorescence detection of dysplasia in patients with Barrett's esophagus, ulcerative colitis, or adenomatous polyps after 5-aminolevulinic acid-induced protoporphyrin IX sensitization," *Gastrointest. Endosc.*, vol. 49, no. 1, pp. 97–101, 1999.
- [14] A. Garcia-Urbe, N. Kehtarnavaz, G. Marquez, V. Prieto, M. Duvic, and L. V Wang, "Skin cancer detection by spectroscopic oblique-incidence reflectometry: classification and physiological origins," *Appl. Opt.*, vol. 43, no. 13, pp. 2643–2650, 2004.
- [15] A. Garcia-Urbe, K. C. Balareddy, J. Zou, and L. V Wang, "Micromachined fiber optical sensor for in vivo measurement of optical properties of human skin," *Sensors Journal, IEEE*, vol. 8, no. 10, pp. 1698–1703, 2008.
- [16] G. Marquez and L. Wang, "White light oblique incidence reflectometer formeasuring absorption and reduced scatteringspectra of tissue-like turbid media," *Opt. Express*, vol. 1, no. 13, pp. 454–460, 1997.
- [17] L. J. Janik, R. H. Merry, and J. O. Skjemstad, "Can mid infrared diffuse reflectance analysis replace soil extractions?," *Anim. Prod. Sci.*, vol. 38, no. 7, pp. 681–696, 1998.
- [18] K. Islam, B. Singh, and A. McBratney, "Simultaneous estimation of several soil properties by ultra-violet, visible, and near-infrared reflectance spectroscopy," *Soil Res.*, vol. 41, no. 6, pp. 1101–1114, 2003.
- [19] P. C. Kariuki, F. Van Der Meer, and W. Siderius, "Classification of soils based on engineering indices and spectral data," *Int. J. Remote Sens.*, vol. 24, no. 12, pp. 2567–2574, 2003.
- [20] Y. Ge, J. A. Thomasson, C. L. Morgan, and S. W. Searcy, "VNIR diffuse reflectance spectroscopy for agricultural soil property determination based on regression-kriging," *Trans. ASABE*, vol. 50, no. 3, pp. 1081–1092, 2007.

- [21] R. A. Viscarra Rossel, D. J. J. Walvoort, A. B. McBratney, L. J. Janik, and J. O. Skjemstad, "Visible, near infrared, mid infrared or combined diffuse reflectance spectroscopy for simultaneous assessment of various soil properties," *Geoderma*, vol. 131, no. 1, pp. 59–75, 2006.
- [22] E. Ben-Dor and A. Banin, "Near-infrared analysis as a rapid method to simultaneously evaluate several soil properties," *Soil Sci. Soc. Am. J.*, vol. 59, no. 2, pp. 364–372, 1995.
- [23] G. W. McCarty, J. B. Reeves, V. B. Reeves, R. F. Follett, and J. M. Kimble, "Mid-infrared and near-infrared diffuse reflectance spectroscopy for soil carbon measurement," *Soil Sci. Soc. Am. J.*, vol. 66, no. 2, pp. 640–646, 2002.
- [24] C.-W. Chang, D. A. Laird, M. J. Mausbach, and C. R. Hurburgh, "Near-infrared reflectance spectroscopy–principal components regression analyses of soil properties," *Soil Sci. Soc. Am. J.*, vol. 65, no. 2, pp. 480–490, 2001.
- [25] K. W. Daniel, N. K. Tripathi, and K. Honda, "Artificial neural network analysis of laboratory and in situ spectra for the estimation of macronutrients in soils of Lop Buri (Thailand)," *Soil Res.*, vol. 41, no. 1, pp. 47–59, 2003.
- [26] D. J. Brown, K. D. Shepherd, M. G. Walsh, M. Dewayne Mays, and T. G. Reinsch, "Global soil characterization with VNIR diffuse reflectance spectroscopy," *Geoderma*, vol. 132, no. 3–4, pp. 273–290, 2006.
- [27] G. R. Hunt, "Spectral signatures of particulate minerals in the visible and near infrared," *Geophysics*, vol. 42, no. 3, pp. 501–513, 1977.
- [28] R. N. Clark, "Spectroscopy of rocks and minerals, and principles of spectroscopy," *Man. Remote Sens.*, vol. 3, pp. 3–58, 1999.
- [29] J. B. Reeves III, G. W. McCarty, and J. J. Meisinger, "Near infrared reflectance spectroscopy for the determination of biological activity in agricultural soils.," *J. Near Infrared Spectrosc.*, vol. 8, no. 3, pp. 161–170, 2000.
- [30] T. H. Waiser, C. L. S. Morgan, D. J. Brown, and C. T. Hallmark, "In situ characterization of soil clay content with visible near-infrared diffuse reflectance spectroscopy," *Soil Sci. Soc. Am. J.*, vol. 71, no. 2, pp. 389–396, 2007.
- [31] K. D. Shepherd and M. G. Walsh, "Development of reflectance spectral libraries for characterization of soil properties," *Soil Sci. Soc. Am. J.*, vol. 66, no. 3, pp. 988–998, 2002.

- [32] D. Cozzolino and A. Moron, "The potential of near-infrared reflectance spectroscopy to analyse soil chemical and physical characteristics," *J. Agric. Sci.*, vol. 140, no. 1, pp. 65–71, 2003.
- [33] A. Moron and D. Cozzolino, "Exploring the use of near infrared reflectance spectroscopy to study physical properties and microelements in soils," *J. near infrared Spectrosc.*, vol. 11, no. 2, pp. 145–154, 2003.
- [34] "ASD. website, high intensity contact probe." [Online]. Available: www.asdi.com/accessories/high-intensity-contact-probe. Accessed: September 27, 2010.
- [35] C-C. Chang, A. Garcia-Uribe, J. Zou, L. V. Wang, B. Banerjee, "Fast and minimally-invasive tumor margin detection using a novel micromachined 'side-viewing' OIIRS sensor probe," in *13th Solid-State, Sensors, Actuators, and Microsystems Workshop*, Hilton Head, South Carolina, June 1-5, 2010.
- [36] A. Garcia-Uribe, E. B. Smith, J. Zou, M. Duvic, V. Prieto, and L. V Wang, "In-vivo characterization of optical properties of pigmented skin lesions including melanoma using oblique incidence diffuse reflectance spectrometry," *J. Biomed. Opt.*, vol. 16, no. 2, 020501, 2011.
- [37] "Microchem Corp. website, Nano TM SU-8." [Online]. Available: www.microchem.com/products/pdf/SU8_50-100.pdf. Accessed: January, 18, 2009.
- [38] K. A. Sudduth, J. W. Hummel, S. J. Birrell, F. J. Pierce, and E. J. Sadler, "Sensors for site-specific management.," *State Site Specif. Manag. Agric.*, pp. 110–183, 1997.
- [39] A. Zhu, L. Band, R. Vertessy, and B. Dutton, "Derivation of soil properties using a soil land inference model (SoLIM)," *Soil Sci. Soc. Am. J.*, vol. 61, no. 2, pp. 523–533, 1997.
- [40] J. Zhu, C. L. S. Morgan, J. M. Norman, W. Yue, and B. Lowery, "Combined mapping of soil properties using a multi-scale tree-structured spatial model," *Geoderma*, vol. 118, no. 3, pp. 321–334, 2004.
- [41] A. B. McBratney, M. de L. Mendonça Santos, and B. Minasny, "On digital soil mapping," *Geoderma*, vol. 117, no. 1, pp. 3–52, 2003.
- [42] R. A. V. Rossel and A. B. McBratney, "Soil chemical analytical accuracy and costs: implications from precision agriculture," *Anim. Prod. Sci.*, vol. 38, no. 7, pp. 765–775, 1998.

- [43] J. A. Thomasson, R. Sui, M. S. Cox, and A. Al-Rajehy, "Soil reflectance sensing for determining soil properties in precision agriculture.," *Trans. ASAE*, vol. 44, no. 6, pp. 1445–1453, 2001.
- [44] I. D. Moore, P. E. Gessler, G. A. el Nielsen, and G. A. Peterson, "Soil attribute prediction using terrain analysis," *Soil Sci. Soc. Am. J.*, vol. 57, no. 2, pp. 443–452, 1993.
- [45] A. C. Scheinost, A. Chavernas, V. Barron, and J. Torrent, "Use and limitations of second-derivative diffuse reflectance spectroscopy in the visible to near-infrared range to identify and quantify Fe oxide minerals in soils," *Clays Clay Miner.*, vol. 46, no. 5, pp. 528–536, 1998.
- [46] A. C. Scheinost, D. G. Schulze, and U. Schwertmann, "Diffuse reflectance spectra of Al substituted goethite: a ligand field approach," *Clays Clay Miner.*, vol. 47, no. 2, pp. 156–164, 1999.
- [47] D. J. Brown, R. S. Brickleyer, and P. R. Miller, "Validation requirements for diffuse reflectance soil characterization models with a case study of VNIR soil C prediction in Montana," *Geoderma*, vol. 129, no. 3, pp. 251–267, 2005.
- [48] M. R. Nanni and J. A. M. Demattê, "Spectral reflectance methodology in comparison to traditional soil analysis," *Soil Sci. Soc. Am. J.*, vol. 70, no. 2, pp. 393–407, 2006.
- [49] E. Ben-Dor, Y. Inbar, and Y. Chen, "The reflectance spectra of organic matter in the visible near-infrared and short wave infrared region (400–2500 nm) during a controlled decomposition process," *Remote Sens. Environ.*, vol. 61, no. 1, pp. 1–15, 1997.
- [50] L. V Wang, "Tutorial on photoacoustic microscopy and computed tomography," *Sel. Top. Quantum Electron. IEEE J.*, vol. 14, no. 1, pp. 171–179, 2008.
- [51] J. Gamelin, A. Maurudis, A. Aguirre, F. Huang, P. Guo, L. V Wang, and Q. Zhu, "A real-time photoacoustic tomography system for small animals," *Opt. Express*, vol. 17, no. 13, 10489, 2009.
- [52] L. Song, C. Kim, K. Maslov, K. K. Shung, and L. V Wang, "High-speed dynamic 3D photoacoustic imaging of sentinel lymph node in a murine model using an ultrasound array," *Med. Phys.*, vol. 36, 3724, 2009.
- [53] M. K. Yapici, C. Kim, C.-C. Chang, M. Jeon, Z. Guo, X. Cai, J. Zou, and L. V Wang, "Parallel acoustic delay lines for photoacoustic tomography," *J. Biomed. Opt.*, vol. 17, no. 11, 116019, 2012.

- [54] J. E. May, "Wire-type dispersive ultrasonic delay lines," *Ultrason. Eng. IRE Trans.*, vol. 7, no. 2, pp. 44–52, 1960.
- [55] A. H. Meitzler, "Ultrasonic delay lines for digital data storage," *Ultrason. Eng. IRE Trans.*, vol. 9, no. 2, pp. 30–37, 1962.
- [56] R. W. Gibson, "Solid ultrasonic delay lines," *Ultrasonics*, vol. 3, no. 2, pp. 49–61, 1965.
- [57] B. A. Auld, *Acoustic fields and waves in solids, vol. 1.*, New York, New York: Wiley, 1973.
- [58] T. R. Meeker, "Dispersive ultrasonic delay lines using the first longitudinal mode in a strip," *Ultrasonic Engineering, IRE Transactions on*, vol. 7, no. 2. pp. 53–58, 1960.
- [59] J. David and N. Cheeke, *Fundamentals and applications of ultrasonic waves*. Boca Raton, Florida: CRC press, 2012.
- [60] M. J. de Boer, J. G. E. Gardeniers, H. V Jansen, E. Smulders, M.-J. Gilde, G. Roelofs, J. N. Sasserath, and M. Elwenspoek, "Guidelines for etching silicon MEMS structures using fluorine high-density plasmas at cryogenic temperatures," *Microelectromechanical Syst. J.*, vol. 11, no. 4, pp. 385–401, 2002.
- [61] A. Rosencwaig and A. Gersho, "Theory of the photoacoustic effect with solids," *J. Appl. Phys.*, vol. 47, 64, 1976.
- [62] D. Debashis, *Basic Electronics*. Nodia, India: Pearson Education India, 2010.
- [63] L. Dobrzynski, P. Zieliński, A. Akjouj, and B. Sylla, "Simple acoustic multiplexer," *Phys. Rev. E*, vol. 71, no. 4, 47601, 2005.
- [64] L. Solie, "A surface acoustic wave multiplexer using offset multistrip couplers," in *1974 Ultrasonics Symposium*, Milwaukee, Wisconsin, November 11-14, 1974.
- [65] C.-C. Chang, Y. Cho, L. V Wang, and J. Zou, "Novel micromachined silicon acoustic delay line systems for real-time photoacoustic tomography applications," in *2013 SPIE BiOS*, San Francisco, California, February 5-7, 2013.
- [66] "Onda Corporation." [Online]. Available: ondacorp.com/tecref_acoustictable.html. Accessed: August 18, 2012.

- [67] C.-C. Chang, Y. Cho, L. Wang, and J. Zou, "Micromachined silicon acoustic delay lines for ultrasound applications," *J. Micromechanics Microengineering*, vol. 23, no. 2, 25006, 2013.
- [68] M. Xu and L. V Wang, "Photoacoustic imaging in biomedicine," *Rev. Sci. Instrum.*, vol. 77, no. 4, 41101, 2006.
- [69] M. Xu and L. V Wang, "Universal back-projection algorithm for photoacoustic computed tomography," *Phys. Rev. E*, vol. 71, no. 1, 16706, 2005.
- [70] J. D. Aussel, A. Le Brun, and J. C. Baboux, "Generating acoustic waves by laser: theoretical and experimental study of the emission source," *Ultrasonics*, vol. 26, no. 5, pp. 245–255, 1988.
- [71] B. Yin, D. Xing, Y. Wang, Y. Zeng, Y. Tan, and Q. Chen, "Fast photoacoustic imaging system based on 320-element linear transducer array," *Phys. Med. Biol.*, vol. 49, no. 7, 1339, 2004.
- [72] J. T. Ylitalo and H. Ermert, "Ultrasound synthetic aperture imaging: monostatic approach," *Ultrason. Ferroelectr. Freq. Control. IEEE Trans.*, vol. 41, no. 3, pp. 333–339, 1994.
- [73] C.-H. Weng, K.-Y. Lien, S.-Y. Yang, and G.-B. Lee, "A suction-type, pneumatic microfluidic device for liquid transport and mixing," *Microfluid. Nanofluidics*, vol. 10, no. 2, pp. 301–310, 2011.
- [74] T. S. Sammarco and M. A. Burns, "Thermocapillary pumping of discrete drops in microfabricated analysis devices," *AIChE J.*, vol. 45, no. 2, pp. 350–366, 1999.
- [75] T. K. Jun, "Valveless pumping using traversing vapor bubbles in microchannels," *J. Appl. Phys.*, vol. 83, no. 11, pp. 5658–5664, 1998.
- [76] M. K. Tan, J. R. Friend, and L. Y. Yeo, "Microparticle collection and concentration via a miniature surface acoustic wave device," *Lab Chip*, vol. 7, no. 5, pp. 618–625, 2007.
- [77] D. Baigl, "Photo-actuation of liquids for light-driven microfluidics: state of the art and perspectives," *Lab Chip*, vol. 12, no. 19, pp. 3637–3653, 2012.
- [78] S. Arscott, "Moving liquids with light: Photoelectrowetting on semiconductors," *Sci. Rep.*, vol. 1, 184, 2011.

- [79] S.-K. Fan, T.-H. Hsieh, and D.-Y. Lin, "General digital microfluidic platform manipulating dielectric and conductive droplets by dielectrophoresis and electrowetting," *Lab Chip*, vol. 9, no. 9, pp. 1236–1242, 2009.
- [80] M. W. J. Prins, W. J. J. Welters, and J. W. Weekamp, "Fluid control in multichannel structures by electrocapillary pressure," *Science* *12*, vol. 291, no. 5502, pp. 277–280, 2001.
- [81] F. Mugele and J.-C. Baret, "Electrowetting: from basics to applications," *J. Phys. Condens. Matter*, vol. 17, no. 28, R705, 2005.
- [82] W. C. Nelson and C.-J. "CJ" Kim, "Droplet actuation by electrowetting-on-dielectric (EWOD): a review," *J. Adhes. Sci. Technol.*, vol. 26, no. 12–17, pp. 1747–1771, 2012.
- [83] A. Nakajima, "Design of hydrophobic surfaces for liquid droplet control," *NPG Asia Mater.*, vol. 3, no. 5, pp. 49–56, 2011.
- [84] N. L. Jeon, S. K. W. Dertinger, D. T. Chiu, I. S. Choi, A. D. Stroock, and G. M. Whitesides, "Generation of solution and surface gradients using microfluidic systems," *Langmuir*, vol. 16, no. 22, pp. 8311–8316, 2000.
- [85] J. Zhong, M. Yi, and H. H. Bau, "Magneto hydrodynamic (MHD) pump fabricated with ceramic tapes," *Sensors Actuators A Phys.*, vol. 96, no. 1, pp. 59–66, 2002.

APPENDIX

CRYOGENIC REACTIVE ION ETCHING

The cryogenic reactive ion etching process is used to achieve anisotropic etching for silicon substrate. The basic idea for anisotropic etching is to find the balance between trench side-wall passivation and trench bottom etching. In cryogenic etching, two process gases are used, which is SF₆ and O₂. SF₆ provides F radical to etch the silicon, while the addition of oxygen gas in low temperature forms SiO_xF_y layer as a protective layer at the sidewall. Also, the low temperature reduces the chemical reactivity. The side wall, covered with protective layer, is less like to be attacked by the ion bombardment. On the other hand, the bottom is exposed to ion bombardment which removes the protective layer; therefore, the bottom is un-passivated and is attacked by the F radical, resulting anisotropic etching. Guidelines for the process control can be found in reference [60]. The process parameters are listed in table 4 and etching profiles are shown in table 5 and table 6. The reactive ion etching system is Oxford Plasmalab 100 ICP System.

Table 4 Process recipe for through-wafer etching.

Step	Time (minute)	Temperature (° C)	Chamber pressure (mTorr)	RF power (W)	ICP power (W)	SF ₆ (sccm)	O ₂ (sccm)	He backing (Torr)
Stable process gas	5	-120	20	0	0	100	17	0
Stable temperature	5	-120	20	0	0	100	17	0.1
Etch	60 (for 250 μm wafer) 90 (for 300 μm wafer)	-120	20	10	600	100	17	0.1
Purge	5	-120	20	0	0	0	0	0

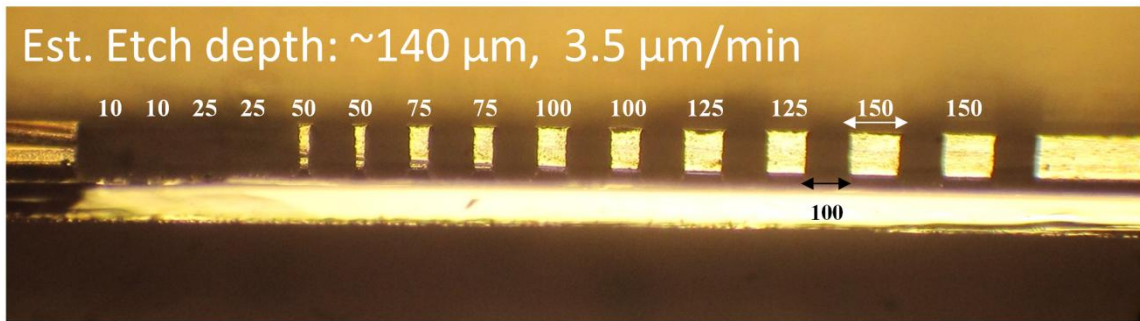


Figure A.1 Etching for 40 minutes with different line width (unit: μm).

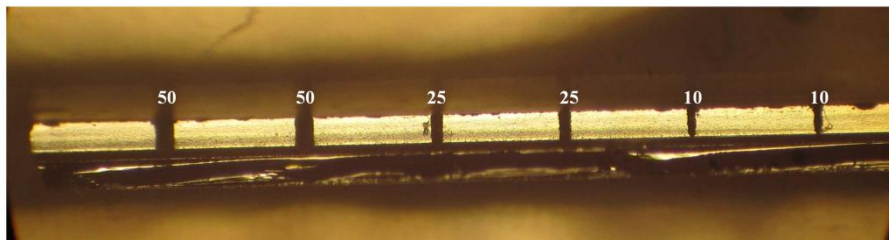
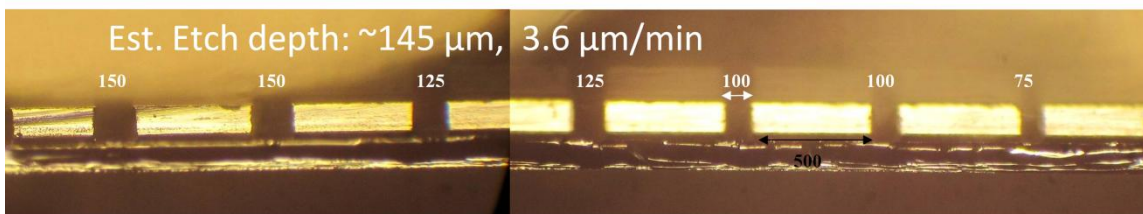


Figure A.2 Etching for 40 minutes with different trench width (unit: μm).

Table 5 Etching profile with different O₂ flow rate for 10 minutes.

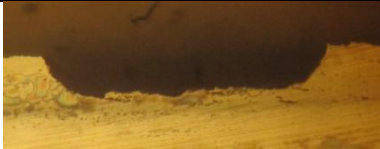



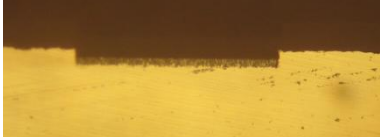

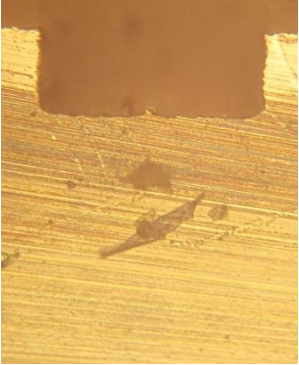
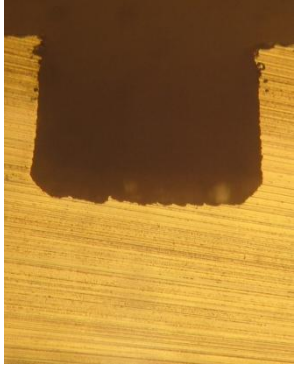
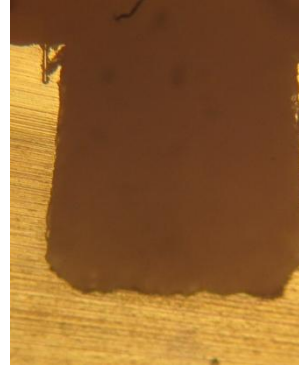
O ₂ flow rate (sccm)	Profile	Note
10		Isotropic etch, undercut
15		Vertical side wall
16		Vertical side wall
17		Vertical side wall
18		Black silicon formation
20		Black silicon formation

Table 6 Etching profile with different etch time.

Etch time (minutes)	20	40	60
Profile			
Depth (μm)/ Etch rate (μm/min)	79/3.95	147/3.67	221/3.68
Side wall angle with respect to vertical (°)	0	4	4